



BALLISTIC ELECTRON EMISSION MICROSCOPY IN A 4-PROBE STM SYSTEM

Standardizing Techniques and Analysis to Explore its Potential for Buried Interface Characterization

MSC. THESIS

Written by *Alec P. Romagosa*

March 5, 2022

Supervised by

Rajib Batabyal & Peter Krogstrup Jeppesen

UNIVERSITY OF COPENHAGEN



UNIVERSITY OF
COPENHAGEN

NAME OF INSTITUTE: Niels Bohr Institute

NAME OF DEPARTMENT: Center for Quantum Devices

AUTHOR: Alec P. Romagosa

EMAIL: qvn822@alumni.ku.dk

TITLE AND SUBTITLE: Ballistic Electron Emission Microscopy in a 4-Probe STM System
- Standardizing Techniques and Analysis to Explore its Potential for Buried Interface Characterization

SUPERVISOR: Peter Krogstrup Jeppesen

CO-SUPERVISOR: Rajib Batabyal

HANDED IN: March 5, 2022

DEFENDED: 25.10.2021

NAME _____

SIGNATURE _____

DATE _____

Contents

1	Introduction	3
1.1	Background	3
1.2	Standardization of BEEM in a 4-Probe STM System	5
2	Experimental	7
2.1	Scanning Tunneling Microscopy Concepts	7
2.1.1	Tunneling Current	9
2.1.2	Measurements of Topography & Density of States	10
2.2	4 Probe STM System	11
2.3	Theory of Ballistic Electron Emission Microscopy	13
2.4	Implementation of BEEM in 4-Probe STM	21
3	Epitaxial Au Thin Film on GaAs	23
3.1	Introduction	23
3.2	Experimental	26
3.3	Results & Discussion	27
3.4	Conclusion	32
4	Au/GaAs Schottky Contacts and Au/Ti/GaAs Ohmic Contacts from Circular-Patterned Thin Film Deposition	33
4.1	Introduction	33
4.2	Experimental	35
4.3	Results & Discussion	37
4.4	Conclusion	45
5	Analysis of BEES Data	47
5.1	Introduction	47
5.2	Interval Optimization	48
5.2.1	Models	50
5.3	Results	56
6	BEEM Investigations of Metal-2D Electron Gas System	60
6.1	Introduction	60
6.2	Experimental Setup	61
6.3	Experimental Results	62
6.4	Simulation	65
6.5	Conclusion	69
7	Future Research and Conclusion	70
7.1	Significance	70
7.2	Further Research	70
7.3	Theoretical Conditions for the Experimental Realization of Majorana Zero Modes using BEEM-enabled Fabrication of Superconductor-Semiconductor Hybrid Nanowires	72
7.4	Conclusion	77
8	Acknowledgments	79
	Appendices	85

A	Analysis Code	85
A.1	Height Profiles	85
A.2	Sub-threshold Fitting	86
A.3	2D Map Fitting	90
A.4	Logarithm Fitting	93
A.5	Line-spectra	96

Abstract

This project standardizes the process of ballistic electron emission microscopy (BEEM) using a 4-probe STM system for multiple probe transport measurement on advanced nanostructures manufactured *in-situ* in the attached ultra-high vacuum molecular beam epitaxy (UHV-MBE) system. Specifically, this provides a path to developing a system for producing the semiconductor-superconductor hybrid nanowires expected to host the computationally valuable phenomena known as Majorana zero modes (MZMs), and to this end, a wide variety of systems and statistical methods were tested. The first sample attempted consisted of an Au thin film grown on a GaAs(100) substrate, with ballistically transported current measured through the backside plate used for staging the sample. Though this sample did not yield the response expected of the Schottky barrier which typically forms at Au/GaAs interfaces, it provided the basis for a further multiple-probe technique using an additional probe connected to a circular Au/Ti/GaAs deposition region, with this extra Ti layer creating an ohmic contact with a resistor-like I-V curve. To optimize Schottky barrier height extraction and precisely measure spatial shifts, various models and optimization techniques were investigated and compared to literature values. One such model, which gave a highly precise fit in tests, was used to extract Schottky barrier heights and associated goodness-of-fit statistics over a 61×61 point scan, to be compared with an analogous 3600 nm^2 area on a topographic STM scan. As a final test, BEEM measurement was performed on a confined 2-dimensional electron gas (2DEG) system, composed of an $\text{In}_{0.8}\text{Al}_{0.2}\text{As}/\text{InAs}$ thin-film heterostructure with a patterned Al deposition acting as the BEEM contact layer. The 2DEG confinement layer, was composed on InAs in an attempt to analyze the barrier height of the wide-gap semiconducting alloy surface layer. The result was next compared to simulations of similar systems using self-consistent Schrödinger-Poisson simulation and $\mathbf{k} \cdot \mathbf{p}$ perturbation theory, though no barrier height was found.

1 Introduction

1.1 Background

In condensed matter physics, the study of possible material implementations of modern quantum computing theory has become a significant field of research, in large part as a result of the broad variety of possible industrial applications. As a primary example, in theoretical computer science, the space of computationally solvable problems currently includes problems which require polynomial time to complete, as a function of the complexity of the initial problem (for instance, determining whether a subset of a given set of integers sums to a given final target

integer, which would require an exponential number of steps to solve as the size of the set of integers grows, while more deep and complex problems would require a prohibitively lengthy time to solve for all but the simplest cases in a conventional computing scheme. In contrast, when considering quantum-mechanical operators on a particular state, the fundamental representation of data, ordinarily being a single two-level 'bit,' becomes instead a Bloch sphere representing the superposition of the 'on' and 'off' states of the bit, with some arbitrary relative phase between 'on' and 'off' components of the superposition, as is common in quantum mechanics. As such a system could incorporate many different possible operators and coupled states which would otherwise not be available, the operation space and operational complexity of such a quantum machine would extend beyond the binary gates and logical operators of traditional computer science. Ultimately, the key requirement for this kind system to be created relies on the material conditions which would allow said states to exist for a significant length of time in a consistent superposition, allowing operations to be performed while assuming a minimal loss of information.

A particular form of quantum state, known as MZMs, have been theorized to be possible to construct and verify experimentally in a lab environment, with the possible end result of producing an industrial platform for topologically protected quantum computing devices. [1, 2, 3] The requirements for such a state to exist, however, are by necessity rather complex, with the first precondition being a one-dimensional (1D) superconductor-semiconductor hybrid nanowire, with the superconductor side of the interface being a conventional s-wave superconductor, and the semiconductor side having a strong spin-orbit coupling, in order to create a split band dispersion with a proximitized superconductivity effect near the interface. Separately, the presence of an applied magnetic field can in theory be used to open a Zeeman gap in the band dispersion. The particle-hole symmetry of the superconductor, combined with the topologically distinct phase of this system caused by the applied magnetic field, can create a p-wave superconductivity effect. Through the conglomeration of these various effects on the electronic structure of a 1D system, the emergence of Majorana quasiparticles has been predicted at each end of the nanowire. These hypothesized states would exist at zero energy within the superconducting gap in the k-space dispersion relation. The key feature of these prospective states is the expected property of non-Abelian exchange statistics, wherein the path by which the particles at either terminus of the wire replace each other in a larger system can result in a non-degenerate difference in final state. In terms of final application, this topological 'braiding' of multiple particle paths could then be used as part of the operations of a complete quantum computer. To give a better picture of the theoretical workings of such a system, the section on future research gives a mathematical overview of the necessary spin-orbit coupling

and the Kitaev toy model explaining how such states could arise in a 1D nanowire.

One of the most crucial aspects to creating such a system is being able to fabricate the actual material platform itself. Any possible scattering center along the length of the nanowire can easily lead to a loss of information, and modeling and performing the high-complexity nanostructural growth processes necessary to construct such an elaborate system presents a truly towering hurdle to implementing the conceptual model which suggests such a system is possible. More specifically, it requires the fabrication of localized metal-semiconductor interfaces with atomic accuracy, with all possible parameters, defects, and interface properties being sharply controlled and measured. Measuring these interfaces, by itself, presents yet another significant challenge. Because the interfaces are fabricated on an underlying substrate in a high-precision molecular beam epitaxy environment, it is necessary to have a tool to investigate the electronic and material properties of these deeply buried heterostructural discontinuities, in particular one using the attached scanning probe system, capable of performing in scanning tunneling microscopy (STM), spectroscopy (STS), and atomic force microscopy (AFM) modes.

While the general technique of STM has been studied and modified to an extensive degree since its original conception in a landmark 1982 paper by Binnig and Rohrer, [4], the method investigated here is to use the particular implementation of the basic STM system known as ballistic electron emission microscopy (BEEM) to study such interfaces. This technique has been studied from a variety of perspectives, such as to determine the spatially-resolved characteristics of an Ru/Al₂O₃. [5]

1.2 Standardization of BEEM in a 4-Probe STM System

The central purpose of this thesis is to standardize the process of multiple probe BEEM using a 4-probe STM system for nanostructures fabricated *in-situ* in the UHV environment of an attached high-precision molecular beam epitaxy (MBE) deposition system. Accomplishing this task allows the experimental environment to be further applied to a variety of systems which can be fabricated in this environment, and is expected to be used in further research on the electronic properties of material interfaces such as semiconductor-superconductor hybrid structures, which is a highly studied potential material platform for the industrial application of quantum computing principles as a result of the MZMs predicted to appear as part of the electronic structure of such a system.

The BEEM process can be used to provide precise, spatially-resolved information on the transmission of current through buried metal-semiconductor interfaces, which can in turn be used as a key input in the process of material growth optimization necessary to create the atomically pristine epitaxial thin films necessary

for the predicted electronic behavior of such interfaces to be realized. Standardizing this process consisted of first fabricating and evaluating the current response of the BEEM system when applied to an Au thin film epitaxially grown on GaAs, a material interface which has been highly studied for its role as a high-speed Schottky barrier diode. [6] When measuring this system through the technique involving two scanning probes and the backside plate attached to the sample acting as electronic contacts, as has been employed in prior implementations of the BEEM process, the expected Schottky barrier response did not occur, necessitating the use of a more elaborate, three-probe, technique, to precisely control the conditions of the contact measuring the ballistically transmitted collector current measured through the backside staging plate of the sample in the prior measurement. This newly standardized technique replaces the backside plate contact with a surface level contact consisting of a third Au tip submerged in a circular layer of Au grown on a thin circular layer of Ti, separating it from the underlying GaAs substrate, and thereby creating a classical resistor-like ohmic contact, through which current transported ballistically across a separately grown Au/GaAs interface can be measured in a highly controlled manner.

To determine a broadly applicable, precise, and consistent method of extracting and comparing the height of the Schottky barrier present at such an interface, a variety of models and statistical optimizations for extracting the Schottky barrier voltage threshold of this system were then implemented and compared with literature values for similar samples, as well as with each other, once the expected barrier-like current response was detected. For example, the highly precise and well-fitting, yet computationally fast model developed by Qin *et al.* [7] results in a value of 1.18 V for the threshold voltage, significantly higher than what might be expected based on other models applied to similar samples in previous studies. Such a model can be applied over many individual scanning points to give a spatially-resolved image of the barrier height, to be mapped in 2 dimensions (2D) alongside the surface morphology of the sample.

Furthermore, this system was applied to a sample containing a confined 2D electron gas layer (InAs), separated from its surface and a patterned deposition of Al using a wide-gap semiconducting alloy ($\text{In}_{0.8}\text{Al}_{0.2}\text{As}$). To understand the band structure of this sample and assess the possibility of using the BEEM setup as a means of recording the barrier height separating the confinement layer from the surface, self-consistent Schrödinger-Poisson simulation and $\mathbf{k} \cdot \mathbf{p}$ perturbation theory have been employed to give a qualitative picture of states and charge density of such a system.

2 Experimental

In this thesis, our goal is to standardize BEEM spectroscopy (BEES) measurement with the four probe STM system of the Microsoft Quantum Materials Laboratory (MQML) in Kongens Lyngby, Denmark. By accomplishing the development of this system, BEEM can be used to provide electronic band information of the buried interfaces of thin film heterostructures. We firstly describe the working principle of the scanning tunneling microscopy and spectroscopy techniques. Then, the BEEM setup can utilize the high spatial resolution of an STM system, while using its spectroscopic mode to measure BEES, which is capable of probing the interface band structure and its spatially-resolved characteristics. The STM system consists of four tips which can simultaneously perform STM and STS measurements, connected to a high resolution UHV scanning electron microscope (SEM). STM is a tool which is typically used to measure a conducting sample which has a vacuum barrier through which electrons tunnel, creating a current that flows through the conducting sample, completing the electronic circuit and providing a means of measuring this tunneling current. However, with a four probe STM system, we can measure the conducting quantum structures grown on an insulating substrate using two tips: one tip can be operated in the standard STM mode while the other tip is used to ground the circuit by merging it with a conducting structure while precisely controlling its depth. The attached UHV SEM is used for the positioning of these tips on the sample in order to correctly locate the structures under study. BEEM performed in this way is a three-terminal measurement technique, and these tips can be used as contacts for measuring the base and collector currents of the BEEM system. This chapter gives a comprehensive discussion of this system, combined with the experimental tools and their working mechanisms.

2.1 Scanning Tunneling Microscopy Concepts

Scanning tunneling microscopy, in its basic application, is a type of high-resolution, highly sensitive microscopy technique which is used to measure the morphological properties of the surface features of a material sample by measuring the tunneling amplitude across a vacuum barrier. Many other specialized versions of the general scanning probe microscopy (SPM) concept exist, such as STM itself. Beyond just ballistic electron microscopy, AFM based techniques such as non-contact AFM and Kelvin probe force microscopy, and many more have been developed.

In STM, an atomically sharp STM tip is brought into proximity with an atomically clean sample surface via a finely-controlled piezoelectric scanner combined with coarsely-controlled piezoelectric components to measure the quantum mechanical tunneling current through a vacuum barrier (as shown in Figure 1). This measured tunneling current is part of a circuit which provides cyclical feedback to

the scanning piezoelectrics which can be used to precisely scan across a 2D array of points in the constant current mode of operation. This feedback can be interpreted as deviations from a predefined distance between tip and sample, which can be electronically adjusted to maintain equilibrium about this preset value. All these steps of operation are conducted via a standard dedicated electronics system for STM operation.

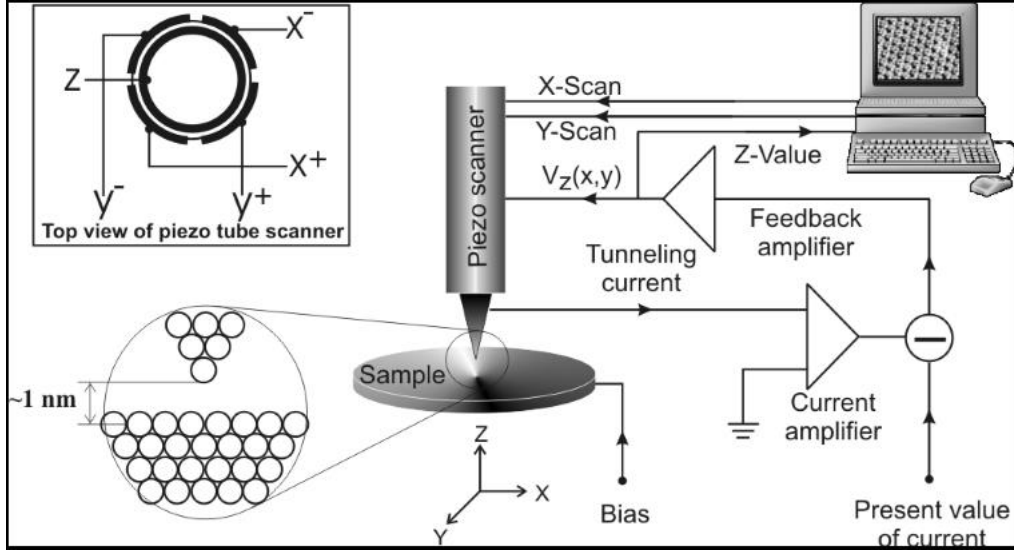


Figure 1: Circuit Diagram of the STM setup. The scanning action of the tip is controlled by a piezoelectric crystal which can be expanded and contracted through applied voltage in accordance with a characteristic piezoelectric tensor of the material. The tunneling current between the tip and sample for a given bias voltage between them is then passed through a feedback loop which is used to hold the net current through the sample constant. The necessary distance between the sample and tip which is required to maintain this current is then recorded as a 2D image on the attached PC. This schematic diagram was taken from the internet. [8]

A detailed schematic of the core STM system is shown in Figure 1, with the key characteristics of the atomically fine tip and the piezoelectric tube scanner electrical contacts highlighted in the zoomed in and inset sub-figures, respectively. The connected PC controls the x-direction and y-direction scanning of the tip, while the tunneling current is fed into a feedback loop which in turn controls the z-direction motion of the tip, with the z-position being recorded by the PC. An external bias is also applied in order to drive the tunneling current.

2.1.1 Tunneling Current

Applying a bias between the sample and scanning probe tip can lower or raise the Fermi level of the sample relative to the level of the tip. With a negative bias voltage applied to the sample, the tunneling current runs from the sample to the tip in accordance with the lower relative Fermi level of the tip, just as the reverse occurs for positive bias, as schematically illustrated in Figure 2.

The tunnelling current between sample and tip follows time-dependent perturbation theory as shown by Equation 1.

$$I = -\frac{4\pi e}{\hbar} \int |M|^2 \rho_s(\varepsilon) \rho_t(\varepsilon + eV) (f(\varepsilon)[1 - f(\varepsilon + eV)] - [1 - f(\varepsilon)]f(\varepsilon + eV)) d\varepsilon \quad (1)$$

Here $|M|^2$ is the matrix element representing the tunneling probability amplitude, $\rho_s(\varepsilon)$ is the DOS of the sample, $\rho_t(\varepsilon + eV)$ is the DOS of the tip, $f(\varepsilon)$ is the Fermi-Dirac distribution of the sample and $f(\varepsilon + eV)$ is the Fermi-Dirac distribution of the tip.

$$f(\varepsilon) = \frac{1}{1 + e^{(\varepsilon - \mu)/k_B T}} \quad (2)$$

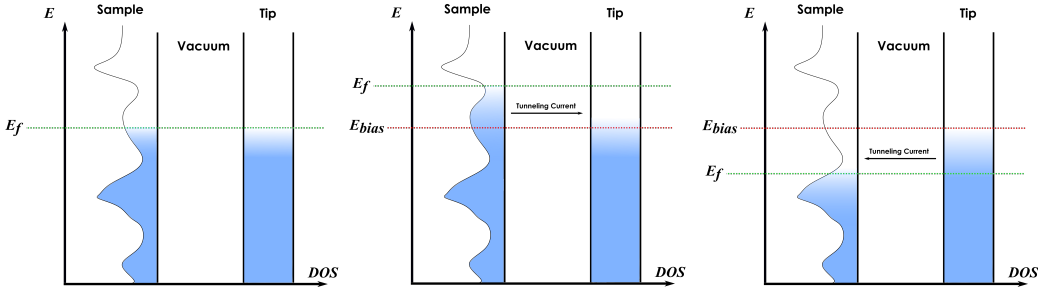


Figure 2: When there is zero bias voltage applied between the sample and tip, the Fermi energies, E_f , of the sample and tip will align. When a negative bias voltage is applied to the sample a disparity between sample and tip will appear increasing the effective Fermi energy, E_f , between sample and tip. This disparity will cause a tunneling current to flow from the sample to the tip. When a positive voltage bias is applied to the sample the disparity will be inverted and the effective Fermi energy, E_f , of the sample will be lowered compared to the tip. This disparity will cause a tunneling current to flow from the tip to the sample.

Measurements were taken at a temperature of $T = 77$ K, giving a cutoff width of about $3k_B T = 19.91$ meV at the Fermi surface. The small temperature broadening width means that, effectively, nearly all states below the Fermi energy will be filled and those above the Fermi energy will be empty. The result of this is that the

only current between the sample and tip will be in the energy range between the applied bias, $E_{bias} = -eV$, and the Fermi energy, $E_f = 0$.

$$I = \frac{4\pi e}{\hbar} \int_{-eV}^0 |M|^2 \rho_s(\varepsilon) \rho_t(\varepsilon + eV) d\varepsilon \quad (3)$$

Using a tip with a comparatively flat DOS, it can be assumed that the DOS is constant and that $\int_{-eV}^0 \rho_t(\varepsilon + eV) d\varepsilon = \rho_t(0)$. This assumption simplifies Eq. 3 and means that only the DOS of the sample will affect the tunneling current.

$$I = \frac{4\pi e}{\hbar} \rho_t(0) \int_{-eV}^0 |M|^2 \rho_s(\varepsilon) d\varepsilon \quad (4)$$

Assuming that the vacuum barrier is a square barrier, the Wentzel-Kramers-Brillouin (WKB) approximation can be used to solve the tunneling probability amplitude, $|M|^2$. The assumption of a square barrier is generally appropriate, as the tilt of the barrier (the applied bias voltage) will be on the scale of 100 meV, while the height, ϕ , of the barrier will typically be on the scale of several eV, $E_{bias} \ll \phi$. This approximation makes the tunneling probability, $|M|^2$, independent of the bias voltage, E_{bias} , and it can be written as

$$|M|^2 = e^{-2s\sqrt{2m_e\phi}/\hbar} \quad (5)$$

where s is the width of the barrier (the distance between tip and sample), and m_e is the mass of an electron. From Equation 5 the equation for tunneling current can then be written as

$$I = \frac{4\pi e}{\hbar} \rho_t(0) e^{-2s\sqrt{2m_e\phi}/\hbar} \int_{-eV}^0 \rho_s(\varepsilon) d\varepsilon \quad (6)$$

It is the exponential proportionality between current, I , and tip-to-sample distance, s , combined with an atomically sharp tip and a high tunneling barrier, ϕ , that gives STM its high resolution and precision.

2.1.2 Measurements of Topography & Density of States

The STM can be used to measure not only the topography of a sample, but its local density of states (LDOS) as well. This allows one to scan over a 2D region, mapping DOS as a function of both energy and position. Topography measurements are taken by first fixing the bias voltage, V , between sample and tip. The tip then scans across the surface while the tunneling current, I , is kept constant by a feedback loop controlling the z-direction piezoelectric. The height is mapped by recording the voltage applied to this piezoelectric component, giving

an image of the sample's topography. The units in which the height is measured in this way will, however, be arbitrary and dependent on the voltage and current resulting in a need for further calibration. Another issue is variations in electron density, though this typically is limited by the exponential dependency of tunneling current on distance having a greater effect than the dependency of DOS. The local density of states (LDOS) can be derived from the relation between current and DOS taken from Equation 6.

$$\frac{dI}{dV} \propto \rho_s(\varepsilon) \quad (7)$$

To accomplish this, a lock-in amplifier is used to reduce the noise by modulating the bias voltage, V_0 , with an AC voltage, dV . The voltage modulation, dV , is set to a certain frequency (preferably a prime number, to avoid overlap with other frequencies in the tunneling current spectrum) such that the current modulation, dI , can then be measured at that same frequency. The DOS can then be related to spatial features of the sample by methodically scanning the tip across the surface while taking spectra measurements, making line-cuts. In all the DOS measurements, the zero bias level is taken to represent the Fermi level of the sample.

2.2 4 Probe STM System

The lab used in this experiment consists of a main UHV tunnel which is connected to three MBE systems with the facilities to grow a significant variety of samples and a four probe Scienta Omicron STM with an attached SEM. This STM system operates at three different temperature ranges namely, 4.2K (LHe), 77K (LN2) and room temperature (RT). The STM is controlled and data are recorded with a dedicated electronic control system known as Matrix. Figure 3 shows this STM in the laboratory. The inset shows the four STM scanners as seen from above, positioned at the four corners of a rectangular sample mounted at the bottom of these tips. The SEM is mounted on top of the sample and scanners in order to get the full field of view of the sample and four tips at a same time.

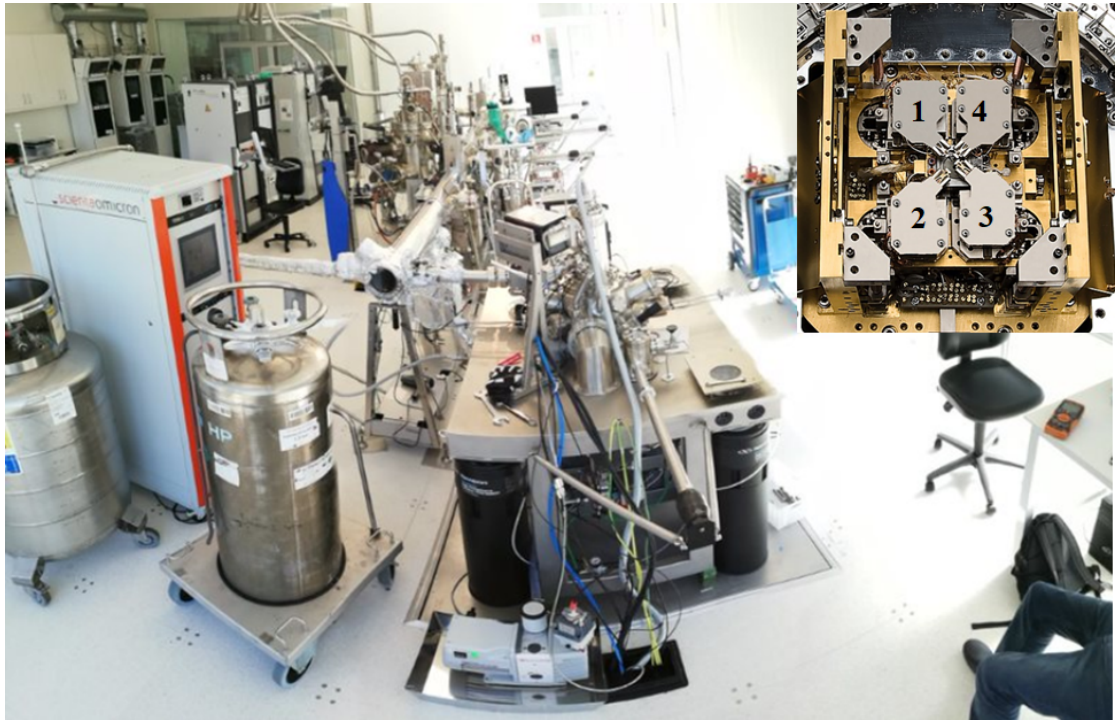


Figure 3: View of 4 probe STM enclosure, with the staging platform and labeled tip holders inset.

Using the 4 probe set up, more advanced modes of scanning and transport measurements can be developed. Specifically, by using one tip as a contact, current can be injected or received very precisely at various points on the sample. This opens up wide possibilities beyond those allowed by the more straightforward mode of single probe scanning, which has applications in characterization of various lithographically generated nanostructures and surfaces with interesting and unusual transport properties, whether nanowires, quantum dots, quantum spin Hall bars, or others.

For example, when applied to measurements on metal-semiconductor hybrid nanowires, the multiple-probe measurements enabled by this system allows the user to bypass a major roadblock to recording clean and clear STM data in this situation, which is that the surface on which the nanowires are grown is not conductive, and therefore the characteristic STM circuit is incomplete. To circumvent this issue, nanowires can be attached to a conducting pad, with a secondary probe in contact with this new surface in order to complete the circuit. In the Figure 4 we show as an example the microscopy experiments performed on SAG nanowires grown on an insulating substrate. With the help of SEM, we approach both the tips toward the desired structure on which one tip makes contact with the Au thin

film, serving to complete the ground connection, and STM is performed through the second. Figure 4a shows an SEM image with a larger field of view showing InAs SAG nanowires grown on an insulating substrate. In Figure 4b and c an STM image taken on such wires can be seen, along with a 3D image of the same. The width and height of the nanowires were measured to be 200 nm and 52 nm respectively, which are closely agrees with previous *ex – situ* SEM and AFM characterizations on such similar samples. On the right hand side of both nanowires measured in STM (as shown in Figure 4b), multiple tip effects appear as a result of the non-uniformity of the apex of the tip. Such an effect can appear when performing STM measurements on tips of a very large vertical extent in height.

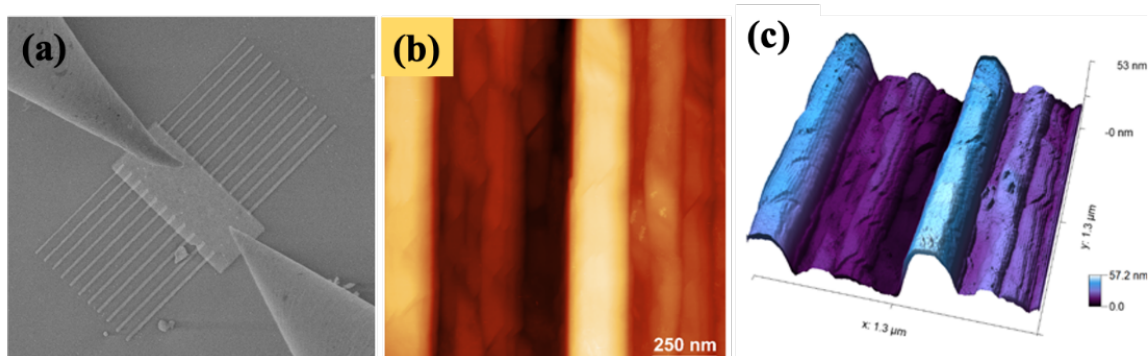


Figure 4: Topographic images showing the utility of multiple probe measurements in STM characterization of the InAs SAG nanowires grown on insulating substrate. (a - c) show a SEM, STM and its 3D view of such nanowires. Width and height of the nanowires were measured to be 200 nm and 52 nm respectively.

2.3 Theory of Ballistic Electron Emission Microscopy

Metal-semiconductor interfaces have been extensively studied for use in electrical applications, in particular, due to the rectifying Schottky barriers found at such interfaces. These electronic barriers are formed in cases where the interface creates a localized upward bend of the conduction band minimum and valence band maximum in the semiconductor near the interface, has been widely exploited in the fabrication of Schottky diodes. Au/GaAs interfaces have been especially studied for use in precision applications which require a low forward voltage drop and fast switching. [9] The ballistic electron emission microscopy is one of the limited instrumental tools that offers direct measure of this interface band alignment between metal and semiconductors in terms of measuring the barrier height.

Whereas STM is typically only used to study the surface characteristics of a bulk material, ballistic electron microscopy can be used to go further in studying

the advanced transport characteristics of a more elaborate sample, in particular through the measurement of current across buried interfaces. There is even evidence to suggest that BEEM can in principle be used to assess the characteristics of the surface reconstruction states which define the band structures of vacuum-semiconductor interfaces. [10, 11] It can also be used to estimate the barrier height of the Schottky barrier present in the metal-semiconductor interfaces used to produce the commonly used electrical components known as Schottky diodes. Furthermore, it can be used to assess the shift and deterioration of this interface effect over a the width and breadth of a 2-dimensional surface.

In Figure 5a we show a schematic BEEM set up which utilizes the STM mode of operation to inject constant current through the bias range of interest. The area of influence of this injected current follows a cone of a set solid angle between the tip apex and the interface. This projected area in the interface determines the spatial resolution of the BEES response. The order of magnitude of this resolution is around ~ 1 nm. The injected current is transported though the base metal layer and through the semiconductor across the interface, to be recorded by a separate collector contact. The resulting collector current I_C is measured as BEEM current. Figure 5b shows a typical band alignment of such metal-semiconductor interface.

Ballistic electron transport, or ballistic conduction, occurs when the mean free path of an electron significantly exceeds the dimension of the medium through which it is induced to travel. In such systems as 1-dimensional nanowires, the mean free path of the electron can be controlled to be relatively long, [12] to satisfy this condition, as well as in thin-film electrical contacts, in which case the resistivity of transport across the contact is dictated by the Sharvin mechanism which prescribes the relevant linear combination of each material resistivities on either side of the interface, $R_s = \frac{\lambda(\rho_1 + \rho_2)}{2a}$. [13] The contact resistance in this relation is given by the contact area a , the electron mean free path λ and the resistivities ρ_1 and ρ_2 . In general, the mean free path of a given material is dependent on the ambient temperature and crystal purity of the sample, while in electrical applications it is dependent on the energy of electrons at a given section of a particular circuit or component. In the case of, for example, bulk Au at ambient room temperature, the resulting mean free path, also known as λ_{rt} has been calculated from first principles to be 37.7 nm. [14]

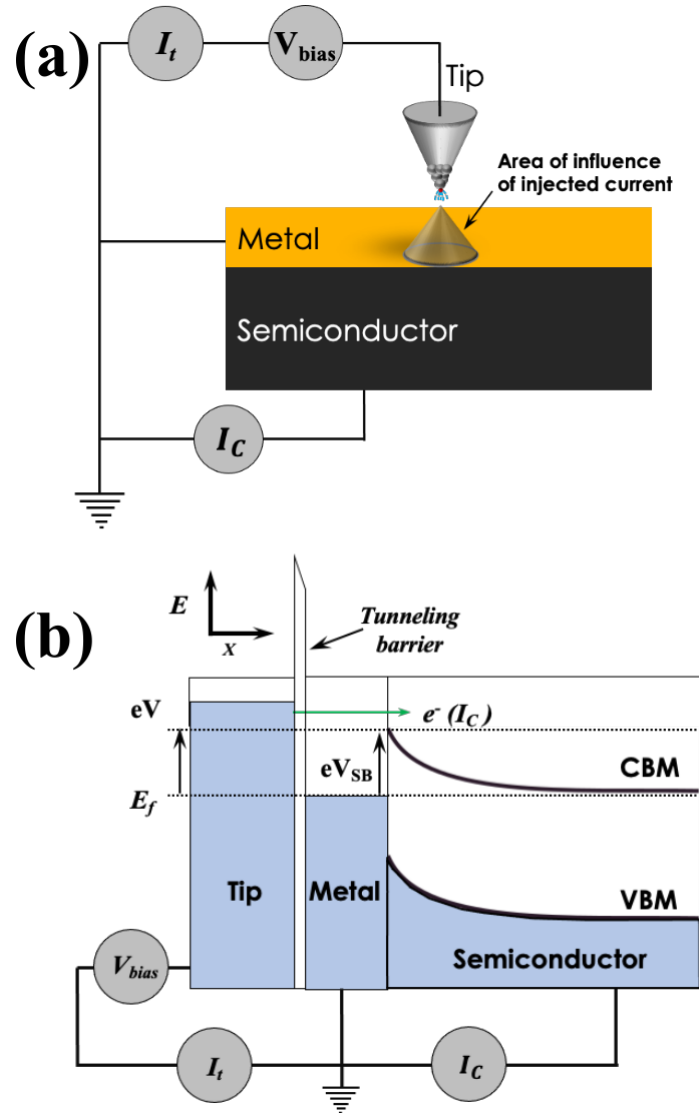


Figure 5: Schematic of a typical BEEM setup: (a) A BEEM setup utilizing the STM system. Area of influence of the injected current determines the spatial resolution of BEEM. (b) The band alignment of the tunneling tip, vacuum barrier with applied bias, metallic Au layer, and GaAs Schottky diode. By tracking the ballistic transport of electrons across the metallic layer and through the Schottky barrier, the precise height of the band offset at the interface can be determined.

The material system and energetic band alignment involved in BEEM measurement is shown in Figure 5. The presence of an externally biased tip creates a tunneling current across a thin vacuum barrier into the metallic layer, which is then recorded through a grounded contact as I_b . Once this bias voltage exceeds

the threshold value set by the Schottky barrier determined by the degree of upward band bending at the interface, all electrons transmitted within a critical emission cone positioned about the tunneling tip are able to ballistically transmit across the metallic thin film, where they are measured as the BEEM collector current I_c .

Disregarding quantum mechanical reflection at the interface between the two materials, and assuming a smooth interface which conserves the electron wave vector transverse to the interface normal, the theory of BEEM covers the tunneling through the vacuum, then base transport and interface transport. [15] This can be modeled as an electron incident upon a potential step, with energy $E_x > E_0$ where $E_0 = E_F + eV_b$ and V_b is the barrier potential. However, conservation of transverse wave vector means that above a certain critical angle, the particle is reflected back at the interface. This is described by the following equation:

$$\sin^2\theta_c = \frac{E - E_0}{E} \quad (8)$$

This situation is further complicated by the possibility of differing effective masses and off-center conduction band minima when used to evaluate a real system. Assuming zone-centered CBMs, but taking into account all possible effective masses, the following equation arises:

$$\sin^2\theta_c = \frac{m_{tf}}{m_{xi}} \frac{E - E_f - eV_b}{E + \left(\frac{m_{tf}}{m_{xi}} - \frac{m_{tf}}{m_{ti}}\right)(E - E_f - eV_b)} \quad (9)$$

In which m_{xi} and m_{ti} are transverse and x-direction components of effective mass in the metal, with m_{xf} and m_{tf} being the equivalent components in the semiconductor. For a polycrystalline metallic base, mass is assumed to be that of the isotropic free electron, this simplifies to the following:

$$\sin^2\theta_c = \frac{m_t}{m} \frac{E - E_f - eV_b}{E} = \frac{m_t}{m} \frac{e(V - V_b)}{E_f + eV} \quad (10)$$

The implication of this is that for relatively small values of m_t , for example in GaAs, the critical angle is also small for values of V which just barely clear the barrier. This critical angle serves to limit resolution, as only electrons at small incident angles can be collected.

The tunneling step can be evaluated with traditional planar tunneling formalism according to the WKB approximation.

$$D(E_x) = \exp(-2 \int k_x dx) \quad (11)$$

$$D(E_x) = \exp(-\alpha s \frac{2}{3eV} [(E_f + \phi - eV - E_x)^{3/2} - (E_F + \phi - E_x)^{3/2}]) \quad (12)$$

$$D(E_x) \approx \exp(-\alpha s(E_F + \Phi - E_x)^{1/2}) \quad (13)$$

$$\alpha = (8m/\hbar^2)^{1/2} \quad (14)$$

with $\Phi = \phi - eV/2$ and ϕ being the work function of the tip. E_x is the x-direction component of incident electron energy, perpendicular to the surface. $D(E_x)$ is then the tunneling probability as a function of energy.

This is comparable to the traditional result of the WKB approximation applied to 1D tunneling where phase varies slowly relative to amplitude:

$$T(E) = \exp(-2\sqrt{\frac{2m}{\hbar^2}V_0 - E}(x_2 - x_1)) \quad (15)$$

From this, the tunneling current can be found by integrating over k-space, taking into account arbitrary temperature and x direction velocity:

$$I_t = 2ea \int \int \int \frac{d^3\mathbf{k}}{(2\pi)^3} D(E_x) v_x (f(E) - f(E + eV)) \quad (16)$$

Which can then further be separated into transverse and x-direction components:

$$I_t = C \int_0^\infty dE_x D(E_x) \int_0^\infty dE_t (f(E) - f(E + eV)) \quad (17)$$

Where $C = 4\pi m a e / \hbar^3$.

When looking at the conditions for tunneling in the tip, if the tip is considered for simplicity to be an isotropic free-electron mass metal identical to the base material, the conditions for tunneling requires that $k_x > 0$ and $E_F - eV < E < E_F$, which creates a semi-spherical shell in k-space limited by the Fermi energy of the tip. In addition, there are further constraints on E_x and E_t . These arise from the critical angle conditions which requires that $E_x > E_0$, as well as the transverse effective mass at the interface (assumed here to be below free electron mass):

$$E_t \leq \frac{m_t}{m - m_t} (E_x - E_F + e(V - V_b)) \quad (18)$$

$$E_x \geq E_F - e(V - V_b) \quad (19)$$

These conditions create a hyperboloid region which can be integrated over to find the proportion of collector current actually measured.

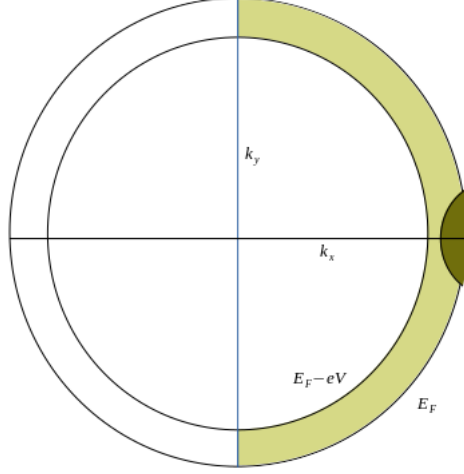


Figure 6: Diagram showing the hyperboloid conditions for tip tunnelling relative to Fermi level as described above.

$$I_c = RC \int_{E_x^{min}}^{\infty} dE_x D(E_x) \int_0^{E_t^{max}} dE_t (f(E) - f(E - eV)) \quad (20)$$

For the very low temperature case this can then be further simplified to the following:

$$I_c = \int_{E_x^{min}}^{\infty} e^{-\alpha s (E_F - \phi - E_x)^{1/2}} dE_x \quad (21)$$

Which is an analytically solvable integral which can be evaluated to get a final equation.

$$I_c = \frac{-2e^{-\alpha s (E_f + \phi - E_x^{min})^{1/2}} (\alpha s (E_F + \phi - E_x^{min})^{1/2}}{\alpha^2 s^2} \quad (22)$$

For higher temperatures, but still low enough that $eV \gg kT$, $f(E)$ must still be considered. In this environment, $f(E + eV)$ can be neglected, and

$$\int_0^{E_t^{max}} dE_t (f(E) - f(E - eV)) \quad (23)$$

in the equation for I_c becomes

$$\int_0^{E_t^{max}} dE_t (1 + e^{\frac{eV - eV_b}{kT}})^{-1} \quad (24)$$

which can be evaluated to

$$kT \ln \frac{e^{-\frac{E_x - E_F}{kT}} + 1}{e^{-\frac{E_t^{\max} + E_x - E_F}{kT}} + 1} \quad (25)$$

While considering voltages below the barrier threshold, by definition, $eV < eV_b$ and, as described above, $E_x > E_F$. However, when integrating over all $E_x > E_x^{\max}$ to thereby find the collector current, the primary contribution comes from high energy states in which $E_t^{\max} \gg kT$ and therefore $e^{-\frac{E_x - E_F}{kT}} \gg e^{-\frac{E_t^{\max} + E_x - E_F}{kT}}$. [7] This leads to the approximation

$$\int_0^{E_t^{\max}} dE_t (f(E) - f(E - eV)) \approx kT \ln [e^{-\frac{E_x - E_F}{kT}} + 1]. \quad (26)$$

Considering that, due to the large values of E_x which are being integrated, $e^{-\frac{E_x - E_F}{kT}} \ll 1$, this can be further reduced to

$$\int_0^{E_t^{\max}} dE_t (f(E) - f(E - eV)) \approx kT e^{-\frac{E_x - E_F}{kT}}. \quad (27)$$

resulting in a final current integral of

$$I_c = RCkT \int_{E_x^{\min}}^{\infty} T(E_x) e^{-\frac{E_x - E_F}{kT}} dE_x \quad (28)$$

with $T(E_x)$ being taken as roughly constant relative to the exponential, resulting in the final solution

$$I_c \approx C_1 (kT)^2 e^{\frac{eV - eV_b}{kT}} \quad (29)$$

for a value of E_x^{\min} of $E_F - e(V - V_b)$. To get the full-spectrum current response in BEES, this can be combined with a second order polynomial expansion, in accordance with the assumption of a parabolic conduction band minimum in the above-barrier energy region, and the goodness-of-fit for each possible location of the threshold energy in this bifurcated model can be evaluated. [16]

$$I_c = \begin{cases} R(kT)^2 e^{\frac{eV - V_b}{kT}}, & \text{for } eV \leq eV_b \\ R(kT)^2 [1 + (\frac{eV - V_b}{kT}) + \frac{(\frac{eV - V_b}{kT})^2}{2!}], & \text{for } eV > eV_b \end{cases} \quad (30)$$

This however, may be complicated further when taking into account quantum mechanical reflection, cases in which transverse effective mass exceeds free electron mass, tip sample distance varies, or those in which the conduction band minimum is not zone-centered (resulting in an off-angle center for the critical transmission cone).

For the case where transverse electron mass exceeds free electron mass, a different region of the tip states are available for tunneling according to the following relation:

$$E_x + \frac{m - m_t}{m_t} E_t = E_F - e(V - V_b) \quad (31)$$

which takes the form of a section of an ellipsoid, rather than a hyperboloid.

When taking into account changes in tip-sample spacing, additional normalization may be necessary, taking $I_c(s_0, V)$ normalized by I_t for all voltages, where s_0 is taken to be a constant distance, thereby resulting in the current response expression

$$I_c = RI_{t0} \frac{\int_{E_x^{min}}^{\infty} dE_x D(E_x) \int_0^{E_t^{max}} dE_t (f(E) - f(E - eV))}{\int_0^{\infty} dE_x D(E_x) \int_0^{\infty} dE_t (f(E) - f(E - eV))} \quad (32)$$

taken at constant current I_{t0} .

In general, conduction band minima are not necessarily perfectly zone-centered, including in the case of GaAs, and for this reason the critical angle requirement becomes shifted, resulting in the new critical angle equation,

$$\sin^2 \theta_0 = \frac{E_{0t}}{E_F + eV_b}, E_{0t} = \frac{\hbar^2 k_{0t}^2}{2m} \quad (33)$$

with k_{0t} being the component transverse to the conduction band minimum. In terms of components of k relative to ellipsoid section created by the conditions for tunneling mentioned above, the phase space condition then becomes

$$k_x^2 - \frac{m - m_t}{m_l} k_y^2 - \frac{m}{m_z} (k_z - k_{0z})^2 + k_z^2 > \frac{2m}{\hbar^2} (E_F + eV_b) \quad (34)$$

with m_t and m_l are the transverse and longitudinal effective masses in the plane of the constant energy ellipsoid section, and $k_{0z} = k_0 \sin \theta_m$, and $m_z = m_t * \sin^2 \theta_m + m_l \cos^2 \theta_m$, where θ_m is the arbitrary off-center position of the conduction band minimum relative to the interface.

Quantum mechanical reflection at the interface further complicates the situation relative to the model above.

Taking into account reflection, an additional transmission factor $T(E, k)$ must be included when integrating the current, which can be approximated as the transmission factor of an electron normally incident on a step potential,

$$T = \frac{4 \frac{k_{xi}}{m_{xi}} \frac{k_{xf}}{m_{xf}}}{\left(\frac{k_{xi}}{m_{xi}} + \frac{k_{xf}}{m_{xf}} \right)^2} \quad (35)$$

where the i and f subscripts refer to quantities (wave vector and effective mass here) in the region of the collector and the base, respectively, with the x and t subscripts indicating the normal and transverse directions, respectively.

This can be expanded in terms of the tip conduction band minimum for zone-centered collector minima:

$$T = \frac{4\sqrt{\frac{(E_x+eV)(E_x+eV-E_F-eV_b-\beta E_t)}{m_{xi}m_{xf}}}}{\left(\sqrt{\frac{E_x+eV}{m_{xi}}} + \sqrt{\frac{E_x+eV-E_F-eV_b-\beta E_t}{m_{xf}}}\right)^2} \quad (36)$$

where

$$\beta = \frac{m_{ti} - m_{tf}}{m_{tf}}. \quad (37)$$

When V and V_b are close in value, the transmission factor scales as $(V - V_b)^{(1/2)}$, though when the transition from base to collector is sudden, the range of this behavior becomes smaller.

2.4 Implementation of BEEM in 4-Probe STM

The 4-probe setup allows for the extension of the basic configuration of BEEM measurement. To accomplish this, a separate tip was used as a contact, allowing for a precise way to measure transport for BEEM, and a further tip was used in place of the traditional backside plate. While similar multiple-probe techniques have been tried before, for example on Si/Ge quantum dots, [17] BEEM performed using a 4-probe STM system is now being standardized as a means of studying buried interfaces of a variety of basic properties of interest to the *in-situ* MBE fabrication of quantum nanowires, such as the kinds of hybrid nanowires which may play host to the elusive Majorana fermions.

The individual scanning probes are carefully positioned over the thin film somewhat near to each other using the overhead SEM. In Figure 7 the SEM image taken of the tip alignment and sample is shown in the inset as well as overlaid on the sample schematic surface. Tip 1 is used as a tunneling junction similarly to traditional STM, while the second tip is connected to the sample to measure non-ballistic current travelling through the metal thin film near the surface. The BEEM current I_c in this setup is then recorded from the sample holder on which the sample is staged, with a conducting glue allowing ballistically transported electrons in the conducting band of the semiconductor to travel through the metal sample holder towards ground.

In Figure 7, we show how the multiple probes of the STM system are used to create the contacts required for BEEM measurement. We use the SEM to locate these triangular metal quantum structures on the semiconductor surface

and the two tips are approached towards such a structure. Tip 2 is then brought into contact with the structure, and tip 1 is used in the standard STM mode of operation.

After performing this setup, regular STM measurements were taken to find a good topographic region on this metal structure, and the scan was continued for some further time at the same temperature to stabilize the tip. Once the tips are nearly entirely free from any apparent drift, BEES measurements were carried out. Moreover, in order to control against environmental noise sources, a lock-in technique can be employed. In our system, this technique is used during the measurement of voltage-driven spectral current response using AC modulation applied to the tip during measurement for each voltage recorded.

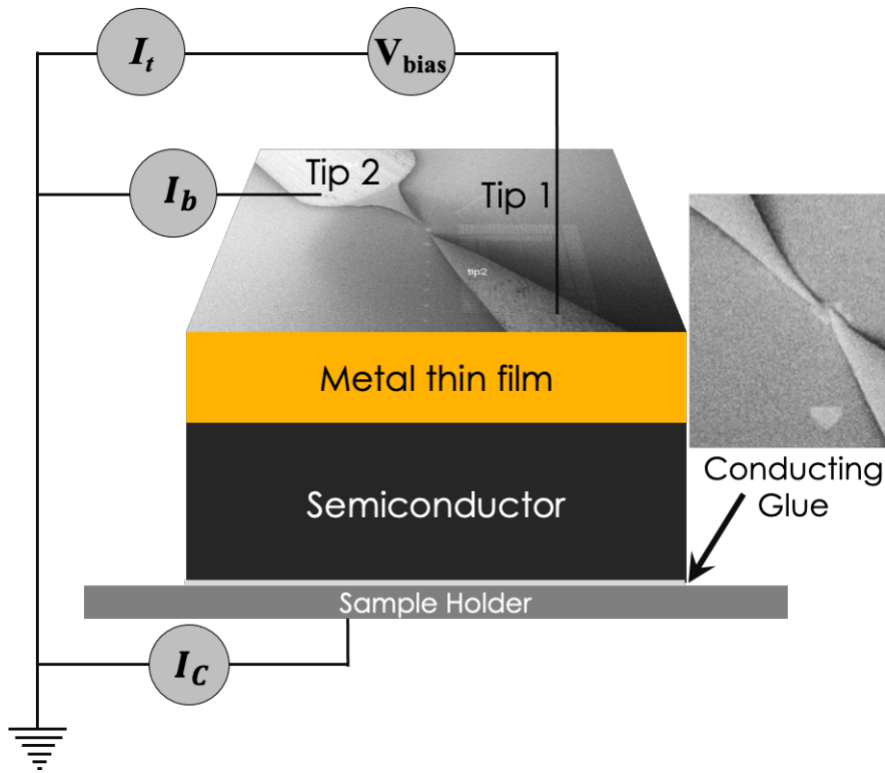


Figure 7: Schematic diagram of the BEEM circuit. One scanning probe is used to inject the electrons in a cone fanning outwards from the tip, with an additional probe measuring the current traveling through the base conductive layer. The final probe, which completes the circuit, measures the ballistic transport through the barrier. This has in the past been measured through a backside plate attached to the bottom of the sample, but can also take the form of an additional probe connected to an ohmic contact elsewhere on the sample surface, which also controls for leakage current and confounding effects.

3 Epitaxial Au Thin Film on GaAs

3.1 Introduction

In order to standardize the four probe STM system, allowing BEEM measurements to be recorded in both the microscopy and spectroscopy modes of operation, as a multiple probe measurement using the back of the sample holder plate as an electric contact, we first attempted to use an Au-GaAs interface fabricated via molecular beam epitaxy as a standard prototype system. This interface was created by growing an ultra thin epitaxial Au film on a GaAs substrate, with the BEEM collector current being measured through the backside of the sample via a sample holder plate glued to the sample with indium, acting as an adhesive.

Au/GaAs heterostructures have been studied extensively from the perspective of crystal growth optimization and morphological characterization. For instance, past studies as early as 1986 have been performed on the precise development of *in situ* ultra high vacuum preparation of gold contacts on GaAs. [18] A GaAs crystal is a semiconductor with a bulk band gap of 1.42 eV, and a zinc-blende crystal structure composed of gallium and arsenic. A metal-semiconductor interface is formed by depositing a thin film of Au on an atomically clean GaAs surface. The material characteristics of this metal-semiconductor interface lead to an exchange of charge carriers (electrons and holes) across either side of the interface, which results in an upward bending of the conduction band minimum and valence band maximum of the semiconductor in the region near the interface, creating an electron depletion layer in the semiconductor as a result of the interface states causing Fermi level equilibrium at the interface. [19] This upward band bending right at the interface produces an energy barrier (known as a Schottky barrier) which impedes the propagation of electrons across the interface. Our aim is to measure this energy barrier using the high energy resolution provided by a scanning tunnelling technique which incorporates BEEM measurement, as BEEM has been shown to be effective as a potential tool to measure this energy barrier directly at the material interface. In previous studies, this Schottky barrier has been measured very accurately by employing the BEEM technique, which has resulted in a rough estimate of about 0.88 eV. [20] Our goal is to measure this energy barrier height and to thereby reproduce the previously reported value with BEEM in order to standardize our four-probe STM set up. The sample currently under consideration was prepared in a very precisely controlled ultra-high vacuum environment provided by the Microsoft Quantum Materials lab, with material growth parameters optimized to create a very clean interface without the protrusions into the semiconductor which would arise from using a GaAs surface which was not atomically clean, as has been the case in some prior studies. [18]

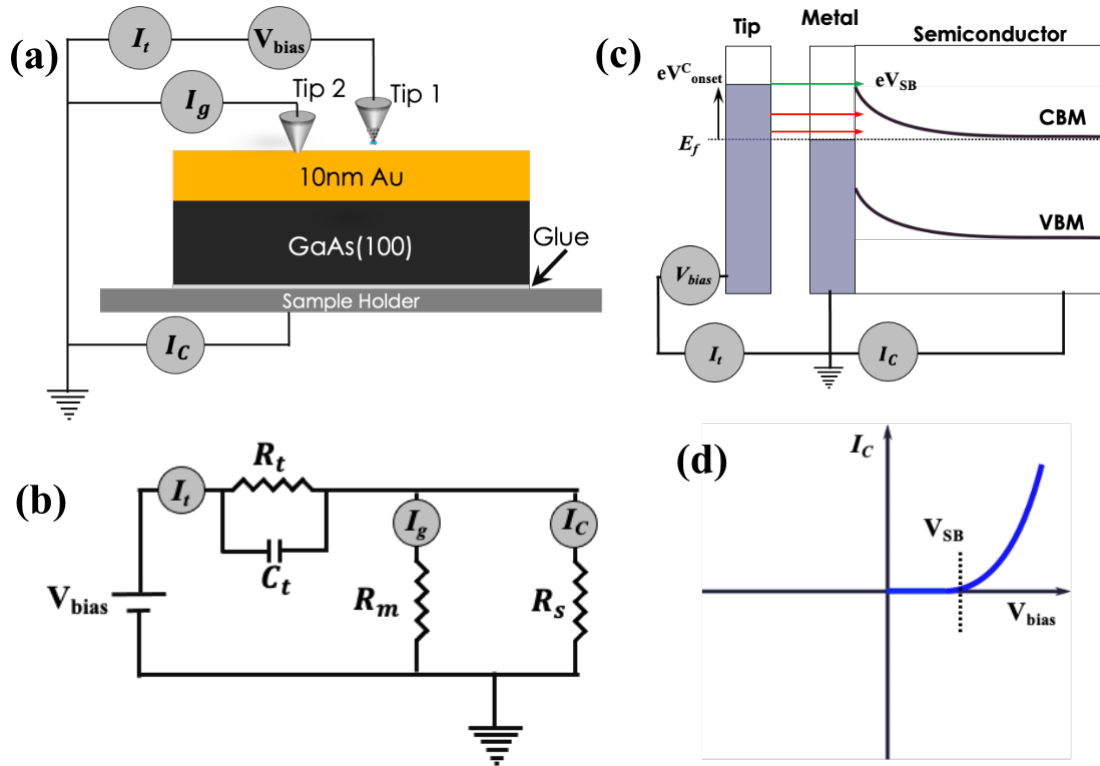


Figure 8: **Experimental setup of BEES.** a) Sample composition and overall circuit construction. I_t is the tunneling current measured by the scanning tip, at a constant voltage set to the point V_{bias} . I_b is the voltage through the 10 nm Au metal layer, and I_c is the BEEM current measured through the backside plate attached to the bottom of the GaAs(100) substrate. b) The same as a), except reduced to the equivalent circuit, with R_t and C_t being the resistance and capacitance across the tunnel junction, R_m being the resistance through the gold layer, and R_s being the resistance going from the tunnel junction to the backside plate. c) The same circuit diagram, but displayed in terms of band alignment relative to the bulk Fermi level of the substrate. The applied bias on the tip raises its effective Fermi level, allowing ballistic transport through the metal layer and over the Schottky diode barrier. d) Illustration of the approximate shape of the expected BEEM current response. By sweeping through various applied biases, the Schottky barrier height can be approximated as the precise point at which current starts to flow freely over the barrier. Because only a small fraction of transmitted electrons are able to flow ballistically across the metal layer, this current is initially very small (on the order of 10 pA).

A schematic diagram of such a sample is seen in Figure 8a, where a 10 nm Au thin film is grown on a GaAs(100) substrate, glued to a metallic sample plate

with indium. A multiple-probe STM system was used to create a closed circuit for measuring ballistic electron transmission in which Tip 1 ($T1$) is operated in the normal STM mode, in which we inject a constant tunneling current into the sample. Tip 2 ($T2$) is then used to approach the sample surface in the same way as during regular STM, and is then pushed into the metal film with a degree of precision in the range of about 2 to 10 nm. $T2$ acts as an electrical contact on the Au film, which can subsequently be used to make the applied bias voltage zero in this region with respect to $T1$. The current measured through this contact is referred to as I_b . Another electrical contact will be needed to measure three-terminal BEEM current, this being the collector current (I_C). For this one, we use as the contact a direct connection to the backside of the sample plate, which can be used to bias the sample. During normal STM operation, the sample is always grounded with respect to the tip with using this backside electrical contact. The typical STM pre-amplifiers were connected to $T2$ and the backside of the sample plate to measure the currents I_b and I_C , respectively.

The main mechanism of BEEM, as previously described in Chapter 2, is as follows: an STM tip is used to inject a constant tunneling current, most of which travels through the contact attached to the Au film ($T2$ in this case) toward electrical ground. However, a small part of the current is then ballistically transported through Au, which results from the mean free path of the electrons in Au being larger than 10 nm, allowing these ballistic electrons to travel through the semiconductor and reach ground through the sample plate. This ballistically emitted electron's current, I_C , is measured via a pre-amplifier connected to this contact. The equivalent electric circuit diagram is depicted in Figure 8b. The tunneling junction can be represented as an equivalent RC circuit with resistance R_t and capacitance C_t . The average tunneling resistance during the normal STM operation is on the order of $28 G\Omega$. The total injected tunneling current I_t is then transported through two different paths, one (I_b) through the metal Au layer, via a classically resistive path with resistance R_m , and the other, I_C , through the semiconductor with the resistance R_s (assuming the capacitive coupling is negligibly small for a DC mode of operation). These two resistances, R_m and R_s , determine the amount of current passing through these two channels. In the normal forward bias scheme of BEEM measurement, in cases where the band bending is upward and forms a Schottky barrier at the interface, R_s provides the larger resistance relative to R_m ($R_s \gg R_m$). This larger R_s allows one to measure the very small amount of BEEM current (I_C) being transported.

A schematic of the band alignment at the metal-semiconductor interface, measured through a tunneling junction, is shown in Figure 8c. Under normal BEEM operation, the metal layer deposited atop the semiconductor and the backside of the sample are both connected to the same system ground and an external bias

voltage is applied to the tip. In the forward bias mode of operation, the tip voltage is methodically varied (as shown in Figure 8c) with respect to the common ground. The BEEM current, I_C , is accessible only when the tip voltage is set to a value larger than that of the Schottky barrier, (V_{SB}) and can be measured as I_C as a function of bias voltage, which is shown in Figure 8d. I_C begins transmission across the barrier when the applied bias voltage has crossed the V_{SB} threshold, and thus can provide a very precise estimation of these interface band characteristics arising from the conduction band offset.

We present here the investigation through BEEM studies of a uniform ultra thin epitaxial Au film on a GaAs surface. The single point BEES measurement has been measured in order to precisely verify the interface Schottky barrier. Based on the measured data, we further discuss the possible challenges of performing BEEM in this 4-probe STM system and will further show some proposed methods of solving these challenges.

3.2 Experimental

The underlying semiconductor substrate was prepared from an n-type Si-doped GaAs(100) wafer, which was polished on both sides, with a carrier density of $(1 \sim 2) \times 10^{18} \text{ cm}^{-3}$. This wafer was initially cleaned via degassing upon loading in the load lock for 10 hours at 200°C. Subsequently, the wafer was transferred to the a-H-cleaning chamber connected to the UHV cluster and after 1 hour degassing at 350°C, atomic hydrogen cleaning was performed for around 20 minutes at 350°C at a background hydrogen pressure of 2×10^{-5} mbar. This technique removes the native oxide layer of the substrate surface and reveals the flat pristine GaAs surfaces. After finishing this a-H-cleaning, the sample was annealed at 350°C for 10 more minutes while the hydrogen was being pumped out, before cooling it to 200°C for transfer.

The Au deposition was performed on this clean GaAs(100) surface using molecular beam epitaxy from an e-Gun electron beam evaporation cell which deposited the Au through a fully opened beam shutter for 8 minutes at a rate of 0.46 Å/s and an emission current which was measured to be around 174 mA. This growth condition is intended to grow a 10 nm Au layer. However, due to an error in applying the growth rate, the actual Au thickness may be significantly larger, even as high as 22 nm thick. In any case, this apparent discrepancy does not deter our investigations, as the mean free path of Au is generally about 37.7 nm [14] and the thickness of the Au layer of this current sample is at most 22 nm, meaning that the electrons can most likely undergo ballistic transmission and produce the expected BEEM current. Upon completion of the deposition, the sample was quickly but carefully transferred *in-situ* to the STM chamber over the course of slightly less than 30 minutes. The STM and BEES measurements were performed at 77 K.

3.3 Results & Discussion

Using scanning probe techniques, we were able to record various morphological properties of epitaxially grown Au films on GaAs(100) surfaces and to show the BEEM point spectra recorded at different locations on the sample surface. In Figure 9a, we show an STM image depicting the typical surface structure of the Au film. In fabricating the gold layer, the major lattice mismatch between the GaAs substrate and the Au thin film creates many small grains during growth. These small grains, having no prevailing single orientation, form together to create

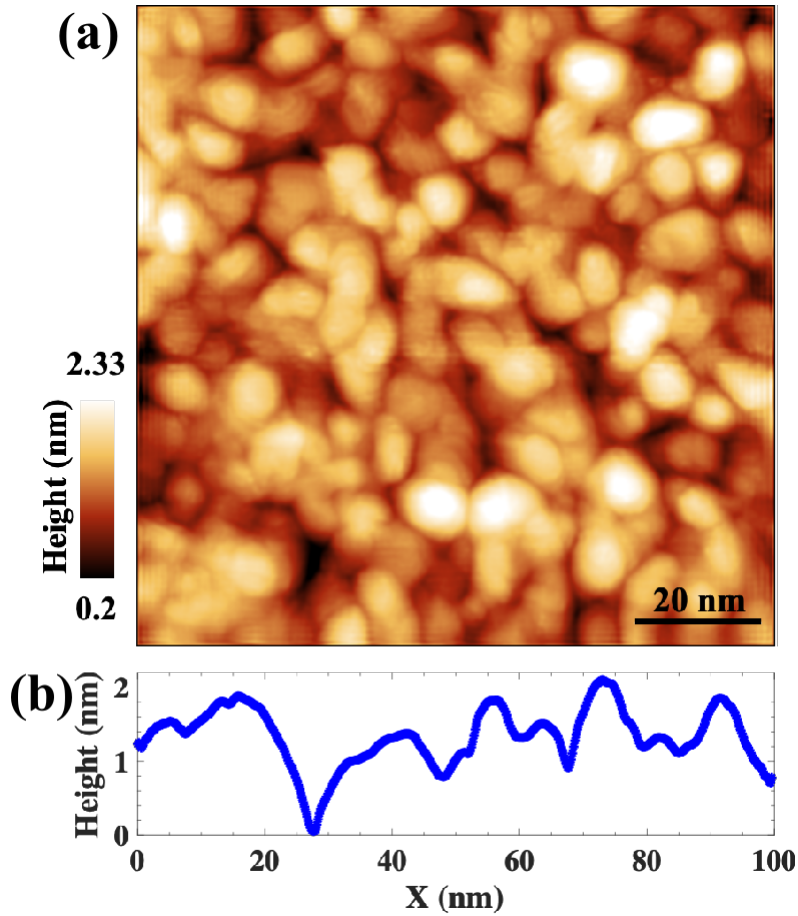


Figure 9: a) Topographic STM image of the epitaxially grown Au film on GaAs, showing small Au grains of various heights and orientations. b) The profile of a single scan line across 100 nm, showing the various grain heights ranging from around 1-2 nm.

a solid layer with many small amorphous hills, rather than an entirely single-phase continuous film. In some cases, through post-deposition annealing, the volume

fraction of these various orientations can be shifted, such that there is a higher volume of Au(100)/GaAs(100) grains relative to Au(111)/GaAs(100), implying that the former is the more stable phase, while the latter is only a metastable configuration found in samples which have not undergone high temperature annealing of up to 450°C. [13] Figure 9b shows a height profile taken along a line marked in (a). The height profile shows an average roughness is about 2 nm.

Spectral measurements were carried out on this sample in order to determine the viability of the sample for measuring the Schottky barrier at the interface. The BEES measurements were performed after completing the standard STM measurements wherein both the tips were thermally stabilized, to eliminate any apparent drift in the piezoelectric components used during scanning, with the specific intent of limiting in particular any drift of the z-direction piezoelectric components. This stable condition was achieved by scanning STM topography normally with both tips for an extended period, most of the time scanning for an open ended duration overnight. These stability checks were performed every time the tips were moved a significant distance across the sample during the process of finding a good region of the sample surface for spectroscopy measurements. Once the tips were stabilized, we kept $T1$ (as shown in Figure 8a) set to STM scanning mode and $T2$ (as shown in Figure 8a) was brought down with extreme precision in regards to the tip-sample distance, keeping this distance stable within roughly the order of magnitude of 1 Å. The tip-sample distance was reduced to zero and the tip was thereby essentially merged into the Au thin film to a depth of about 5 to 10 nm. This tip was used as the grounding contact for the Au layer.

Here, two important aspects of BEEM measurement become relevant. Firstly, if the piezoelectric component controlling the z-position of $T2$ has any degree of upward drift, then at any time, dependent on the magnitude of this drift velocity, the quality of this tip-metal contact can deteriorate, resulting in an increase in the associated contact resistance. It can also in some cases result in the tip becoming completely disconnected from the sample, eliminating any grounding for the Au layer. Secondly, $T2$, along with the third electric contact from the backside plate on which the sample is glued, are both connected to a common system ground through individual STM pre-amplifiers which are used to measure each of the relevant current channels, those being namely I_g and I_C (as shown in Figure 8a). These two different pre-amplifiers, being connected through the same circuit, produce a tiny voltage offset with respect to each other. This voltage offset prevents the two pre-amplifiers from simultaneously recording a single common electrical ground. We measure this offset voltage by minimizing the current passing through both the pre-amplifiers when $T1$ is fully retracted. This offset voltage is then externally fed back into one of the two amplifiers in order to counteract this floating voltage difference which would otherwise distort measurements. Once all these conditions

are achieved, the BEES response is recorded at various sample positions by methodically sweeping the applied bias voltage in increments of 0.0099 V from a low voltage limit of 0.02 V, to the higher limit of 2 V. One of the main differences in recording this data compared to normal scanning tunnelling spectroscopy (STS) is that, during BEES measurement, the response current is measured while keeping the standard STM feedback circuit activated such that a constant current is being injected to the sample over the entire bias range of interest. This constant current injection is achieved by altering the tip-sample distance during bias sweeping. In order to remove this tip-sample distance dependence from the resulting BEES collector current, the BEES current is normalised by tunneling current, which is measured simultaneously with I_C as described in Equation 32.

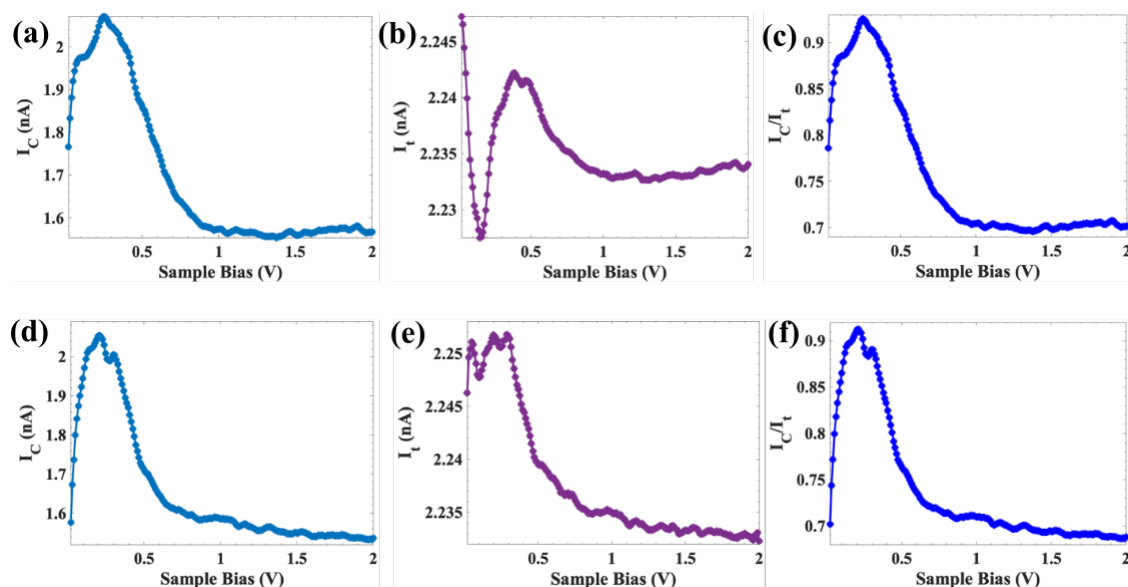


Figure 10: Comparison of the first two spectral measurements, divided into BEEM current, tunneling current, and BEEM current normalized by tunneling current. a) and d) show the collector current, b) and e) show the tunneling current, and c) and f) show the final result from normalizing the collector current by tunneling current to eliminate the effect of variations in tip-sample distance. However, the expected Schottky barrier response does not appear to have occurred.

In Figure 10, two sets of BEES measurements from two different sample locations are shown. (a) through (c) are two different current channels I_C , and I_t measured simultaneously, with the BEEM current normalised by tunneling current being shown for in the third position, (c). In the second row, (d) through (f) follow the same pattern. These results show two important problems to overcome in order to successfully record and interpret a successful BEEM measurement across

energy. For one thing, the BEES data (both measured as I_C in Figure 10a as well as the normalised response shown in Figure 10c) are not consistent from one location to another, which is not what would be expected when comparing with previous measurements. [21] One would expect to record a similar profile with respect to bias voltage, however, these spectral profiles appear noticeably different. For example, while there are two apparent peaks which are located near $0.1V$ and $0.3V$ respectively in Figure 10a, the equivalent peaks in Figure 10d appear at different bias voltages. The rate at which the I_C response decreases in Figure 10a is clearly different relative to in Figure 10d. Moreover, in the region near zero bias voltage, the resulting BEEM current would be expected to be nearly zero due the presence of the Schottky barrier at the Au/GaAs interface as shown in previous measurements [22], which our measured data seems to contradict. In addition, in both cases the current response through both channels is either of a roughly similar magnitude or very large compared to an ideal BEEM signal as has previously been seen, which would be roughly on the order of tens of pA in magnitude. [23, 16] This would appear to imply that the current injected through the tunneling tip, I_t , is flowing through the collector as BEEM current, I_C , while having a negligibly small division of current flowing through the metal Au layer (I_b). A few possibilities were hypothesized as having caused this. The most immediate reason which came to mind was the quality of the contact between $T2$ and the Au thin film becoming degraded, causing the contact resistance R_m to become larger than R_s . To determine whether there was some local degradation of contact quality, $T2$ was carefully and deliberately shifted around to various contact points, while monitoring the I_C collector current response, as a means of trying to improve the contact resistance. However, several trials of this process did not appear to result in a significant shift in BEEM current, with I_C response remaining nearly the same as before. As a large proportion of current from the tunneling tip (I_t) was included regardless of contact point, this process indicated that the reason behind this effect is likely some other phenomena other than precisely the contact resistance between $T2$ and the Au thin film. These data ultimately indicated the issue that, apparently, the Au/GaAs Schottky barrier feature is not present in the collector current response. This result is not in accordance with the expected response of a correctly functioning system, in accordance with the totality of literature evaluating this system which results in precise estimation of the barrier height using BEEM. [16, 15, 24, 25] At this point, we began to suspect that the current path associated with the BEEM current might have leakage either through the interface states or as a result of a short circuit with the sample plate through some edge mode or impurity in the GaAs substrate, which might have resulted during the metal growth process. If there is a leakage path that has much lower resistance than that of the path through the Schottky barrier, this would give rise

to a similar spectra profile as shown in Figure 10. In the next chapter we shall discuss this aspect in greater detail.

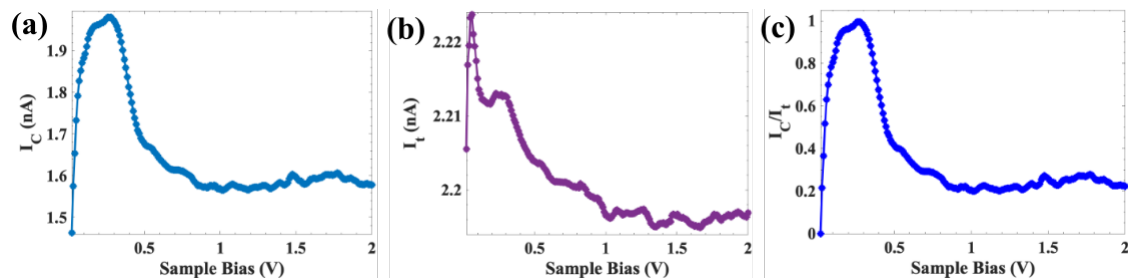


Figure 11: Comparison of the final spectral measurement, at a different location on the sample. As in Figure 10, a) and d) show the collector current, b) and e) show the tunneling current, and c) and f) show the combination of the two, I_C/I_T .

In the following measurements, which were taken to confirm this interpretation and are shown in Figure 11, the results are roughly similar, in that the overall magnitudes of each response are roughly comparable. If ballistic transport was truly occurring as expected, the current through the collector channel would be much lower relative to the transport through the metal layer, suggesting that this relatively high collector current must be travelling through the sample by some other means, such as leakage through a conductive interface or edge states at the edge of the substrate, or some other form of current leakage which may arise from a short-circuit during metal deposition. In the presence of such a leakage current, the small BEEM signal and the associated barrier would then become lost.

Another notable possibility is that, in some cases, the deterioration of the interface quality might also lead to the loss of the Schottky barrier effect which could result in the expected BEEM response failing to occur. Previous studies have shown that diffusion across the interface can lead to leakage current and a deterioration of the electronic properties of Schottky barrier diodes, but that a thin dividing layer of GaN may mitigate this issue. [26] Other studies have described in detail the mechanism of this interface doping reaction and discussed possible means of reducing the effect, such as by fabricating the diode using a much thinner ($\sim 1 \mu\text{m}$) GaAs substrate. [27, 28] However, this does not seem to be the case for our sample, as we have successfully measured the expected BEEM response in a similar sample with the same interface quality, though smaller interface area. A detailed investigation of these measurements will be discussed in the next chapter.

3.4 Conclusion

While this sample did not successfully display the characteristic response expected from a Schottky barrier diode, it provided the first step to standardizing the system and fabricating Au/GaAs interfaces for Schottky barrier measurement. However, likely as a result of leakage current being recorded in the collector, possibly combined with a degraded contact, the expected BEEM response did not occur, as the expected order of magnitude of the BEEM current response I_c is vastly smaller than the current through the metal base, on the order of picoamperes, or even a fraction thereof, and is therefore easily lost when unexpected current channels allow some circumvention of the expected BEEM process. Fabricating a sample with a very wide, effectively 2-dimensional interface between the semiconductor substrate and the Au thin film, as well as the possibility of leakage current flowing around the edge of the semiconductor towards the backside plate contact, created a significant difference from what was initially expected, with both channels of transport giving a response of basically similar magnitude of current. In the next chapter, we shall discuss how we overcome these challenges to successfully measure BEEM current in the manner reported by prior studies.

4 Au/GaAs Schottky Contacts and Au/Ti/GaAs Ohmic Contacts from Circular-Patterned Thin Film Deposition

4.1 Introduction

In order to overcome the issue of BEEM current becoming completely lost as in previous tests, a new technique was needed. Making use of the multiple probes present in the system, the next idea was to avoid the possibility of any short-circuiting or leakage through the substrate by bypassing the use of the backside plate glued to the sample with indium entirely, and instead using a patterned deposition method to create a different interface than the Au/GaAs interface of interest, deposited on a separate region of the substrate. This separate interface can then in principle be used to record current which is ballistically transported across the Au/GaAs interface and into the sample to reach a third probe in contact with this separate patterned deposition structure. Specifically, this patterned deposition method consisted of the preparation of a silicon mask containing many large-area circular holes (a bit more than $600\ \mu\text{m}$ in diameter), which was used as a stencil for the purpose of patterned shadow-mask deposition, creating isolated deposition regions at different locations across the substrate. The interface was required to have the characteristic of acting as an ohmic contact, that is, having I-V curve corresponding to the linear form of a classical resistor, rather than that of a Schottky barrier interface which would display the rectifying behavior of a diode. For this purpose, the material chosen was a thin film of Ti deposited over half of the sample through the patterned shadow deposition mask, with an additional layer of Au being deposited through said mask over both halves, leading to one half with a set of Au/GaAs circular deposition regions, and another half with Au/Ti/GaAs circular deposition regions. The Ti layer acts to eliminate the Schottky barrier characteristic of the Au/GaAs interface as a result of the interface chemistry and Fermi level alignment at the Ti/GaAs interface, which does not cause an upward band bending of the valence band maximum and conduction band minimum in the GaAs substrate. Rather, this Ti layer has been shown to generally improve electrical characteristics when applied to a GaAs substrate. [29] In order to improve the electrical contact between the Au layers and the tips (for measuring base and collector currents), we have replaced the standard W or PtIr tips with custom Au tips made from 0.5 mm thin manually cut, 99.995 % pure gold wire. These Au tips are dipped into the Au layer to achieve the desired contact needed for measurement.

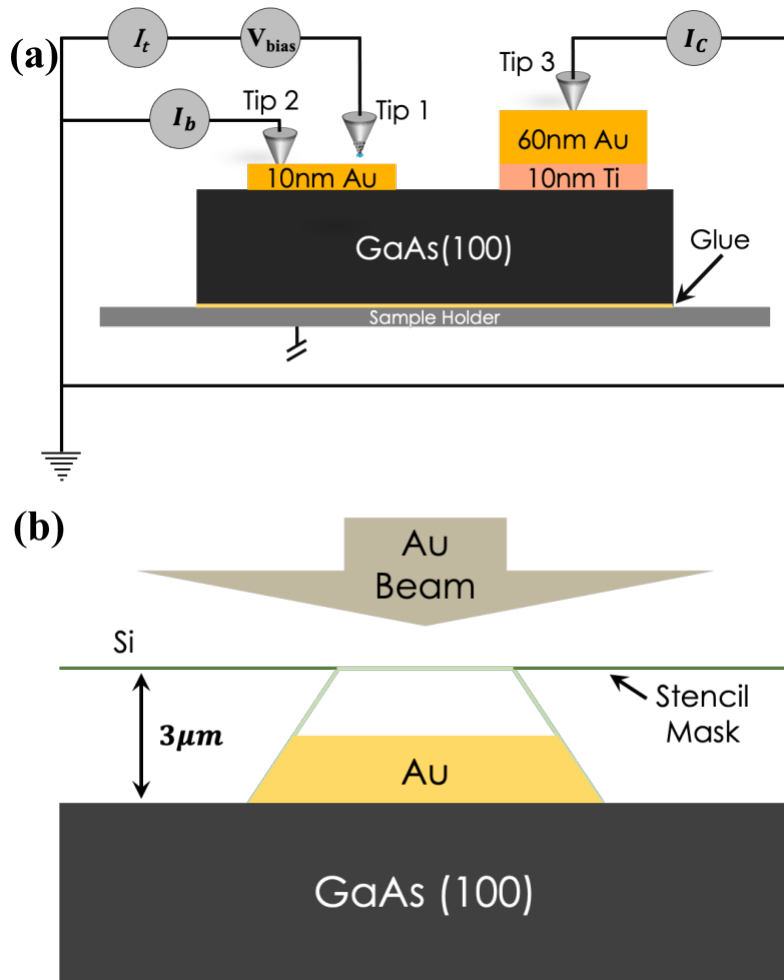


Figure 12: a) Schematic of the final sample after deposition. On the left side is the structure being measured through ballistic transmission, with a nominal thickness of 60 nm, similar to the sample attempted previously. On the right is the ohmic contact created by a layer of Ti, nominally 10 nm in thickness, in order to eliminate the Schottky barrier with the substrate, which is then used to record the BEEM current. b) Simplified schematic of stencil mask deposition. With a greater height relative to the surface, the edges become thinner and less well defined. In this sample, the mask was positioned about $3 \mu\text{m}$ from the underlying GaAs substrate.

In Figure 12 we show a schematic diagram of the improvements that were implemented to eliminate all possibilities that could inhibit the successful measurement of BEEM current, in order to rectify the issues encountered with the previous sample, described in the previous chapter. This sample's improved design employed two tips positioned over a single ~ 10 nm thick circular area on one side, with T_2 being embedded to a depth of about 2 to 5 nm into the Au film. T_2 is used to mea-

sure the base current being transported through this isolated layer of gold, while the other tip, $T1$, which is composed of PtIr for optimal tunneling performance, is used as the tunneling junction which injects the current I_t with a set bias voltage V_{bias} . A third tip, $T3$ is similarly embedded in a separate region of the deposition pattern, which consists of a ~ 10 nm thick Ti layer separating a thicker, ~ 60 nm depth layer of gold from the underlying GaAs(100) substrate. Both $T1$ and $T3$ are composed of Au to create the best possible contact with the Au film when embedded therein. This setup is used to eliminate the current-rectifying behavior of the Schottky barrier formed by the typical Au/GaAs contact. Instead, this interface creates an ohmic contact similar to that in an ideal resistor, and the attached tip can then therefore be used to measure the ballistic current transmitted across the thinner 10 nm Au film and into the conduction band of the semiconducting GaAs substrate. This process, as well as the details of its construction, will be discussed further in the following section.

In this chapter, we describe the details of the sample fabrication and carry out BEEM measurements on the patterned MBE-grown epitaxial Au microstructures fabricated via a stencil mask. For the improved version of the sample design, we show successful BEES measurement with precise estimation of the Schottky barrier height at the Au/GaAs interface.

4.2 Experimental

To describe the sample fabrication process in a detailed way, we first start with the construction of the stencil mask. By creating a solid slab of Si and selectively thinning the circular regions which were used as deposition apertures, removing these sections by heating the sample, either sticking them to the surface far from the relevant region of the substrate, or simply shaking them loose, a patterned shadow mask can be fabricated for use in creating patterned layers on a substrate in concert with an MBE system. As can be seen in Figure 13a, some parts can remain stuck to the edge or fall on the sample, with some circles may not being dislodged at all. This resulted in a final surface construction schematically described in Figures 13b - 13d, with Figure 13b showing an optical image of the sample glued to a flag-style sample plate with the various compositions of the various deposition regions being highlighted, while 13d shows the schematic picture with the tip configuration, as well as the In droplet used for ohmic contact calibration, included. In Figure 13b and d the circular pattern marked in dark brown, light brown and yellow are the Au/Ti/GaAs interfaces, mixed regions and the Au/GaAs interfaces, respectively. The regions represented by white circles are missing areas of the deposition, in which no materials were deposited as a result of blockage by the stencil mask.

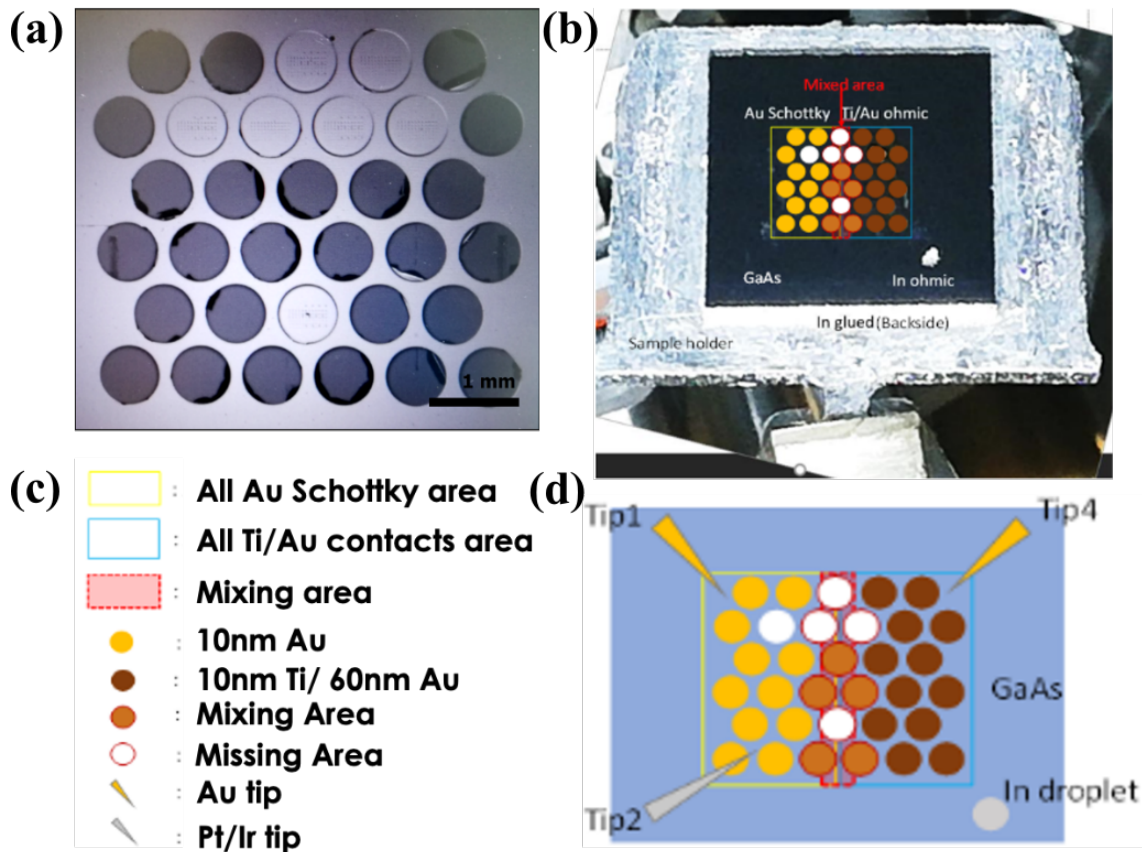


Figure 13: a) Optical image of the Si shadow mask used for stencil growth of Au and Au/Ti in circular patterned deposition regions. Note that some areas which were intended to be used for shadow deposition did not come loose from the mask during the final preparation stage, resulting the final pattern being missing in some areas. b - d) The final look and composition of the sample, with some deposition regions missing as a result of blockage by the deposition mask. However, these missing circular deposition regions are primarily located in the intermixing region between the two regimes of the Au Schottky area and the Ti/Au contact area, which is not used during measurement as a result of the less well defined composition of the circular deposition regions in this boundary area.

This patterned shadow mask is then aligned less than $3 \mu\text{m}$ from the sample, with the close distance to the sample being chosen in order to create a tighter deposition cone, and therefore a sharper boundary between the deposited region and the rest of the sample. By minimizing the contact area between the Au deposition region and the underlying substrate, any chemical reactions or protrusions occurring at the interface or leakage current through, for example, edge modes of the substrate can be limited or eliminated, and therefore any confounding resistance

or leakage current which might stymie the BEEM measurement process can be either mitigated or wholly prevented.

This sample was constructed as a GaAs wafer polished on both sides, which was n-type and Si doped to a density of $(1 \sim 2) \times 10^{18} \text{ cm}^{-3}$ with 10 nm Au pads on one side, and pads composed of a 60 nm Au thin film deposited on top of 10 nm Ti pads on the other side, with a "mixed region" of partially covered or missing pads lying at their interface. Separately, there is an In droplet prepared in ambient atmospheric conditions lying atop the clean GaAs surface.

The cleaning process for the GaAs substrate was the same as previously reported, using a-H-cleaning (see Section 3.2). To create the metal pads, thin films were deposited via a stencil mask at low temperatures of 130°K, using a half-closed main shutter in the initial Ti deposition, thereby growing only on half the mask. The sources for deposition were e-gun cells which deposited Ti at a rate of 0.185 Å/s (with an emission current of 63 mA) for 9 minutes. Afterwards, the Au was deposited for 20 minutes with the half-closed shutter at a rate of 0.46 Å/s and an emission current of 174 mA, and then for an additional 8 minutes with a fully opened main shutter. The sample was removed from the mask holder and immediately transferred to the STM environment, a process which took a bit less than half an hour. An issue with the deposition rate resulted in a significantly thicker final result than the intended 60 nm in the right half and 10 nm in the left half, resulting in real thicknesses of nearly 77 nm and 22 nm, respectively. In any case, these thicknesses will most likely not alter the findings and the conclusions of our experiments based on the evidence that the mean free path of the electrons in Au at room temperature is $\sim 37.7 \text{ nm}$ [14] which is much greater than the thickness of the Au thin film (at most 22 nm) at the Au/GaAs junction through which ballistically emitted electrons can propagate freely.

The purpose of this sample was to standardize the 4-probe STM system for BEEM measurement. Base current was measured across a singular Au circular contact, from the tunneling tip to an Au tip in contact with the same Au region as the electron emission tip. Said current was measured concurrently with the collector current, which was recorded through a third Au tip in contact with a separate deposition region which consisted of an Au layer over a Ti layer used to create an ohmic contact with the underlying GaAs substrate.

4.3 Results & Discussion

Prior to BEEM measurement, traditional scanning probe microscopy was used to investigate the roughly 10 nm thick Au film deposited on the GaAs(100) substrate, as well as on the bilayer deposition consisting of roughly 60 nm of Au and 10 nm of Ti deposited for the purpose of creating the ohmic contact for BEEM measurement. STM investigations have been used to better understand the morphological

properties of the Au surface in the region of the Au/GaAs junction, with these regions being marked by the yellow circular pattern shown in Figure 13. The results are shown in Figure 14, in a high resolution example (Figure 14c) a wider scan showing the general region of measurement (Figure 14b), and a large-area scan showing the overall surface of the sample (Figure 14a). Figure 14a shows very smooth, large-area STM topography with an average roughness of around ~ 2.71 nm. In the closer view of the surface shown in Figure 14b and c, these morphological scans show small grains of various heights and orientations similar to the surface structures shown in the last chapter (Figure 9).

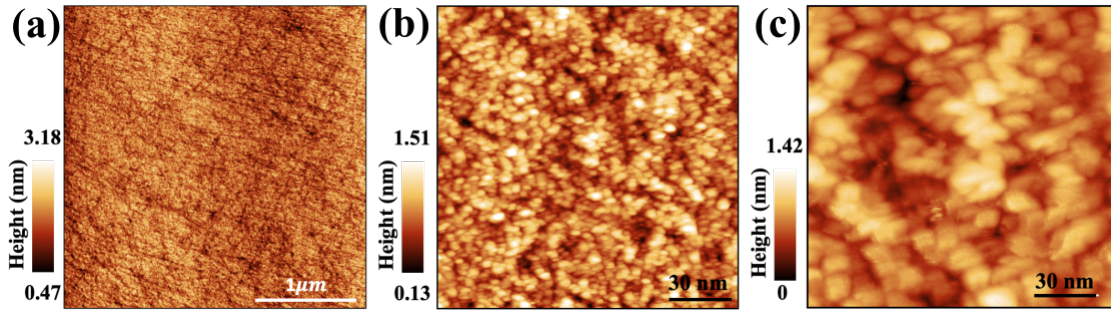


Figure 14: a) Topographic STM image of the Au thin film surface grown through patterned shadow mask deposition, showing many small Au grains and a high degree of variation in height, with close to a 3 nm difference between the highest and lowest elevations. b) Medium-level zoom of the prior scan. The chaos and variety of the grain size can be more clearly seen. c) Zoomed in high resolution scan of the above. Here, the individual shapes of the grains which were formed in various orientations, as well as their boundaries can be seen.

This sample was used to record a detailed analysis of the Schottky barrier feature formed at the Au/GaAs interface. To produce these measurements a high degree of precision was required, which necessitated an extensive process of stabilizing and conditioning the scanning probe system under the traditional STM mode of operation. By scanning for an extended period prior to BEES measurement, any instability in the structure of the tip or drift velocity present in the piezoelectric control system, which typically occurs anytime the tip is moved relatively quickly from one region of the sample to another, can be drastically reduced. Similarly to the previous sample, once the tips were fully stabilized through this process, $T1$ was preserved as a scanning tip for use in ballistic current injection, while the other two tips were carefully embedded into the sample deep enough to avoid any accidental disconnection or shift in resistance arising from this piezoelectric drift or any other cause, to a depth of greater than 5 nm. For this sample, $T2$ was embedded in the same 10 nm Au thin film subject to current injection

by $T1$, in order to record the non-ballistic base current I_b . $T3$, in contrast, was embedded on a separate section identified as being one of the 60 nm Au on 10 nm Ti deposition regions, which can be used to measure the actual ballistic current transmitted through the substrate.

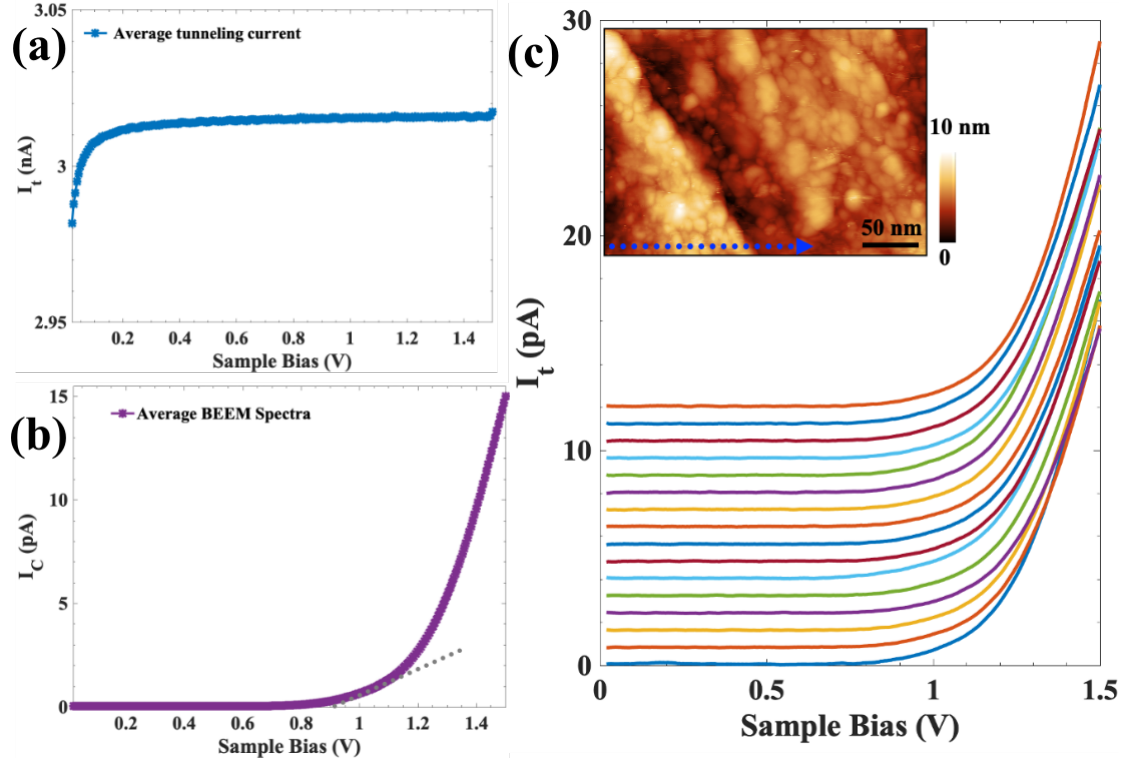


Figure 15: Data from the first line scan, with topography. a) The average tunneling current at each voltage scanned. Though constant throughout most of the range of voltages, for very low voltage the tunneling current becomes unstable and quickly decreases. b) The collector current from ballistic emission itself, with an added line showing the approximate slope near the threshold voltage. c) Waterfall plot showing each individual point of the scan in sequence. Inset: topographic STM image showing the location of the line scan itself placed against the surface morphology on which it was taken.

The use of this second separate deposition region has the benefit of bypassing any imprecisely controlled external aspect of the system which could result in the loss of the characteristic expected BEEM response. As both current response measurement lines $T2$ and $T3$, as well as the current injection tip $T1$ all share the same ground, the associated pre-amplifiers for each tip must be used introduce a small voltage offset in order to equalize the voltage being measured within each

section of the resulting circuit. To find this offset, the current measured as flowing between each probe when all probes are retracted is measured, and this externally applied small voltage offset is methodically varied to find the value which minimizes this steady-state voltage. By minimizing this current, the ground level measured by each probe can be calibrated to a single common value accurate to the ground of the overall system.

Many test measurements of ballistic energy transmission were tested in this configuration, with two high-resolution line scans being recorded over an extended period. The first of these, shown in detail in Figure 15 was taken by recording the current response over voltages from 0.02 V to 1.5 V in intervals of 0.0059 V, across 16 different positions, for a total of 251 data points per scanning location after averaging all repetitions at each point. During this measurement, the tunneling current I_t , as well as the resulting ballistic collector current I_c were simultaneously recorded.

In Figure 15, the data collected in this manner for the initial line scan, is presented, showing clear Schottky barrier-like behavior, in contrast to prior attempts. In Figure 15a we show constant injected tunneling current I_t over the full voltage range of the spectrum. Also of note is the significant deviation of the current response from the otherwise approximately constant tunneling current of about ~ 3 nA for low bias voltage. This is likely a result of tip instability occurring at very low bias due to the extremely small tip-sample distance, as this spectrum has been taken with the STM feedback loop turned on, which maintains constant current by varying the tip-sample distance during the voltage sweep. Based on a very rough approximation, the dotted line in Figure 15b was added to highlight the region of the voltage threshold, giving an initial qualitative estimate of around 0.9 V for the barrier height of the Schottky barrier, in accordance with prior literature. [20] Also of note is the relative lack of large-scale change between points in the scan, shown in Figure 15c, which shows each individual point in the entire 16-point scan. This scan was taken across a large step-edge between two different heights of the Au thin film deposition layer to examine any possible effect this could have on the electronic response at the interface. Our result, however, seems to show no apparent change in the response when moving from one height region to another. This means that these top-level surface irregularities do not apparently have any major role in determining the Schottky barrier height beneath the interface.

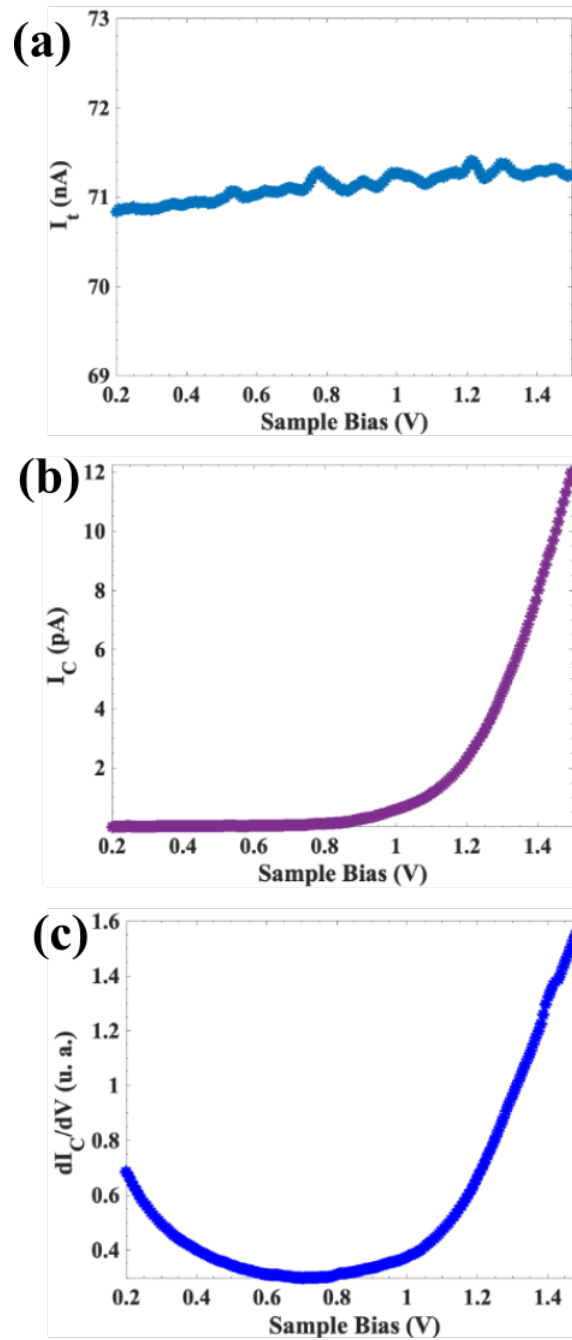


Figure 16: Aggregate of data taken during the second line scan, with all four coordinates scanned subsequently averaged to produce a trace of current for each measured channel. a) The average tunneling current in nA, which remains relatively constant over the sample bias range. b) The trace of the BEEM collector current itself, showing the sharp increase in current above the barrier. c) The derivative of the collector current, as measured through AC modulation applied by an external lock-in amplifier.

The second line scan, as shown in Figure 16, was measured in a similar way, with voltage instead varied from 0.2 V to 1.6 V in increments of 0.0071 V, for a total of 199 data points for each scanning location, a process repeated for all 4 evenly-spaced points of the linear scanning process. This was done with the STM feedback loop activated, which is ordinarily used to automatically adjust the height of the probe relative to the sample, keeping the tunneling current constant (as shown in Figure 16a). In a BEEM context, strictly maintaining constant current in this way has the effect of preserving the current which is injected through the tunneling tip across all applied voltages of interest. As a result of this, the tip sample distance can vary during scanning, the effect of which can be eliminated in a straightforward manner by normalizing the collector current response by collector current, as described by the Bell-Kaiser model. [30]

Figure 16b next shows similar data for the second line scan performed, this time with an adjusted, significantly larger set tunneling current. For this scan, an external lock-in amplifier provided by Zurich Instruments was used to inject a small-amplitude AC tunneling current to the measurement. The application of the lock-in amplifier has the effect of eliminating some environmental noise by creating a clear signal frequency which can be safely separated from other noise modes present in the system. At the same time, the resolution can become limited by the amplitude of the AC signal, added on top of the resolution limits arising from the distance between scan points in voltage and the temperature from liquid nitrogen LN2 cooling (77 K). To eliminate this issue of decreased resolution from the lock-in AC signal, the current modulation can be applied to the z-direction piezoelectric component instead, meaning that, rather than voltage being varied at an approximately constant tunneling current and tip-sample distance, the tip-sample distance is varied in a sinusoidal wave and current response can be measured at various points in the oscillation range of the tip. This AC voltage modulation, of amplitude dV (approximately 10 meV), applied to the z-scanning piezoelectric component is set to a prime number frequency in order to prevent the lock-in signal from overlapping with background noise. The current response signal dI_c is isolated in the resulting measurement, and by measuring this response across all energies in the voltage range scanned, a plot of dI_c/dV can be constructed, to better understand the onset of ballistic transmission through the Schottky barrier. The dI_c/dV response maps the derivative of Figure 16c, with a sharp increase in the onset region of ballistic transport. In accordance with a roughly quadratic response, the dI_c/dV spectrum appears roughly linear in this region. However, there is another high current-slope region in the low-voltage section of the scan, which does not seem to correspond to any clearly visible increase in this region of the dI_c spectrum. The implication of this may be some other confounding effect or alternative model for understanding the system when using this lock-in amplifier

in measuring dI_c/dV .

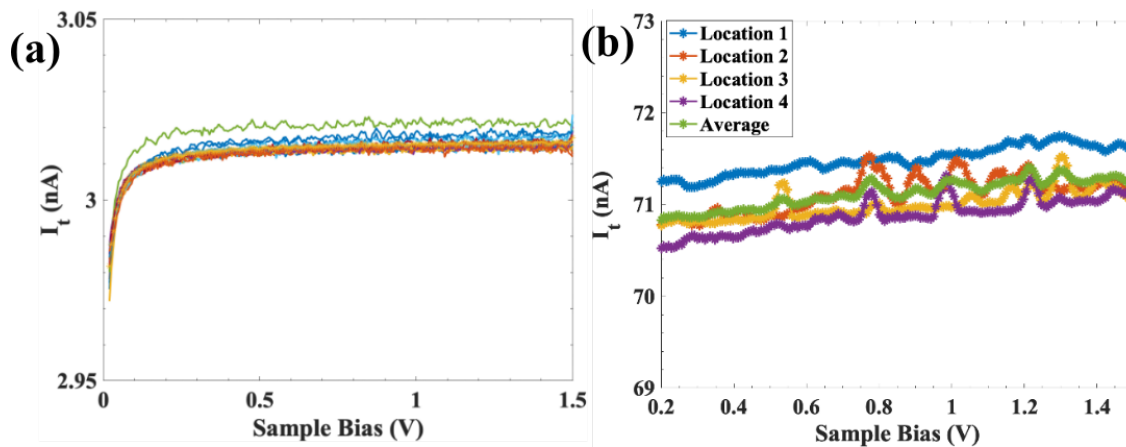


Figure 17: Tunneling current for each scanning location contrasted against overall average tunneling current. a) For the first line scan, some of the later points in the scan have a noticeable drift in overall tunneling current relative to the average. b) For the second scan, with higher relative current, there is still some difference in current between scans, though without the low-voltage instability.

Additionally, in Figure 17a and b, there appears to be a certain shift in the base level of tunneling current between measurements, implying that toward the end of the line scan, there was some increase in current. Given the intended function of the circuit feedback loop of controlling the tip to keep tunneling current constant across all applied voltages, this contradicts what would be expected. Tests were performed which made it clear that this was caused by photocurrent induced by light incident on the sample. Considering that GaAs has been studied in the past for its high-speed photoconductivity response, it seems reasonable that ambient light could have a significant effect. [6] Said shift apparently did not occur during later scans in which all apertures (specifically the viewports of the STM chamber) which might allow external light into the system were blocked with aluminum foil. The relative magnitude of this shift as measured is relatively small, at $\sim 0.2\%$ for the first scan and $\sim 0.6\%$ for the second. This photon induced shift in the tunneling current also alters the offset bias voltage between two current measuring tips (namely $T2$ and $T3$). Additionally, the second I_t measurement was taken with a slightly lower resolution, as a result of the higher set current level.

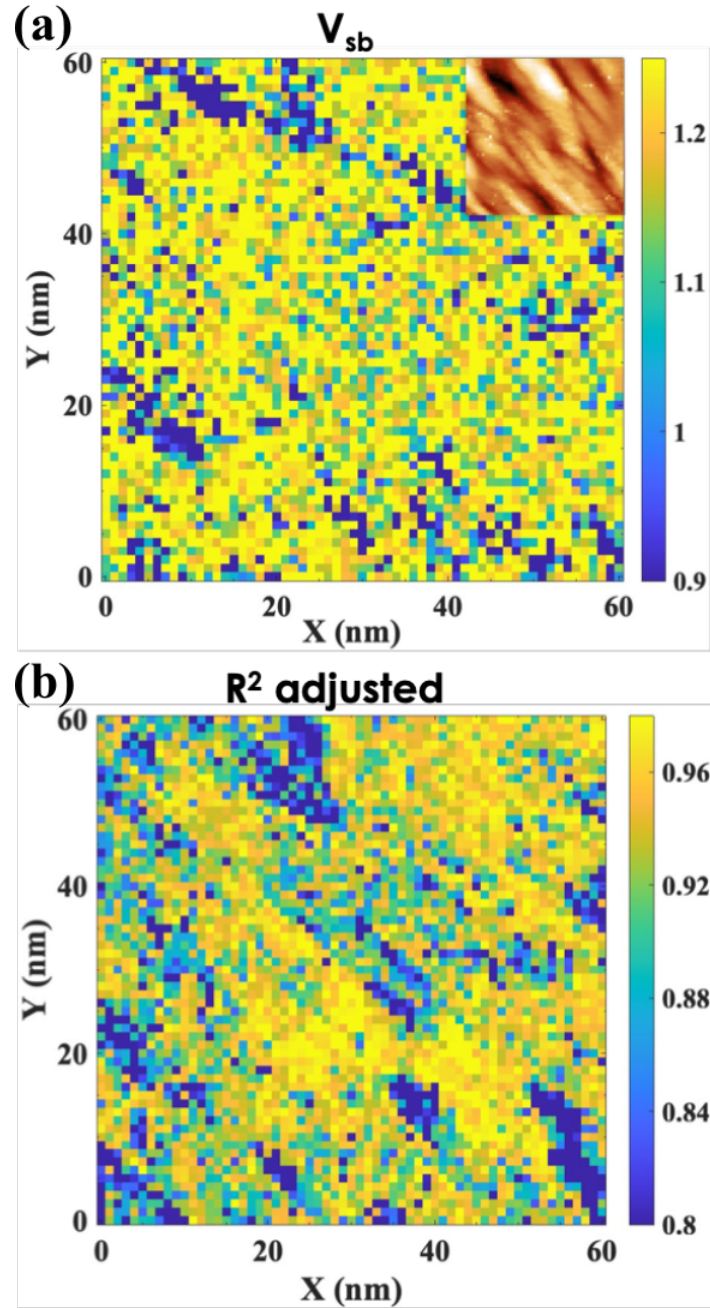


Figure 18: a) 2D map of the extracted barrier height relative to position, with the corresponding topography shown in the inset figure, found by fitting the BEEM current response using a model which takes into account small amounts of sub-threshold current. b) The adjusted R^2 value of the fit created using the above method. Some regions, colored dark blue, seem to have a noticeably worse fit based on this statistic.

An even more detailed and time consuming measurement known as a 2D map was performed over a 61-by-61 point matrix, with each point corresponding to 1 nm² pixel (for a total of 60 nm × 60 nm in area). The results of this process can be seen in Figure 18. A topographic scan was first taken over the same area, with the same resolution (as shown in Figure 18a). Then, a full matrix of 3,721 spatially-mapped spectral voltage scans were recorded in accordance with the previously described process, with each spatial coordinate corresponding to a 251-point scan from 0.02 V to 1.5 V over 0.0059 V intervals, similarly to the previously discussed line scan. At each of these points, the resulting ballistic emission spectrum is fit with a function described in a following chapter on data analysis methods, through which the approximate Schottky barrier height can be extracted. In Figure 18b, the adjusted R^2 of each of these nonlinear least squares estimates is displayed. This process shows the high degree of variability in the Schottky barrier height of this sample, with the many Au grains of various orientations and the gaps between them apparently corresponding to significantly different barrier heights. The adjusted R^2 of these fits, a statistic representing the goodness of fit of the model, sometimes called the coefficient of determination, is also significantly spatially variable in a manner corresponding to the orientations and heights of the Au surface grains, with some regions having a significantly worse fit than others. The details of this process and various alternate models are discussed in the next chapter.

Experimental Resolution The experimental resolution of the BEEM current response of this system mainly depends on two principal kinds of uncertainty: one being the distance between steps in voltage when scanning across a range of voltages, with this value being 0.0059 V for the first 16-point scan, and 0.0071 V for the second, 4-point scan. The temperature of the system during measurement also presents a significant source of noise limiting the resolution of the acquired data. Temperature during scanning was 77 K (from LN2 cooling), giving a thermal energy broadening of about $3k_bT = 19.91\text{meV}$. These two contributions sum as squares to the following equation $\sigma = \sqrt{(3k_bT)^2 + dV^2} \approx 21.2\text{meV}$, with σ being the effective standard deviation.

4.4 Conclusion

This sample was instrumental in firstly providing the basis for standardizing the system as necessary for recording high resolution ballistic electron emission through semiconductor substrates using a 4-probe setup as has been described in detail, as well as in investigating the spatially-resolved characteristics of the electronic structure of Au deposited on GaAs. In principle, this process may be relatively easily replicated with other kinds of metal-semiconductor interfaces, allowing one to analyze, for example, the quality of the buried interface and the effect that various

crystal growth characteristics may have on the electronic qualities of this interface. In contrast to similar, well-established BEEM-related techniques previously studied, the construction of this sample bypasses the many possible confounding effects which can occur when relying on the complete transmission of electrons through the conduction band of a semiconductor substrate to the underlying conductive sample holder in the expected way. Lacking any alternate channels resulting from uncontrolled aspects of the experimental design, such as the possibility of edge reconstructions or other modes of transport not taken into consideration by the BEEM model, this setup can now be used to carry out BEEM measurements on lower dimensional quantum structures as well.

5 Analysis of BEES Data

5.1 Introduction

As has been showed in the previous two chapters, the standardization of BEEM required an extensive process in itself in order to develop a consistent system for reliable BEEM measurement. While it is possible to get a rough estimate of the Schottky barrier height just from a superficial examination of the data, rigorously determining the precise definition of the barrier height from ballistic emission spectroscopy is more complicated, and in fact despite the specific interface in question being extensively studied as a standard example of the kind of interface used in developing Schottky barrier diodes, there is not a single prevailing method for determining the barrier height lacking prior data on the system. Part of the reason for the statistical difficulty of modeling the system is that the basic theoretical equation for the current response, given in Equation 32 in Chapter 2, is, for one thing, itself a fairly computationally elaborate equation when numerically implemented. It also is not necessarily the most accurate when considering a real, non-theoretical sample, which may often have many individual defects scattered across the interface, or other reactions at the interface which lead to the current response not perfectly matching theoretical predictions. In order to simplify and extend the theoretical model, many straightforward means of computationally evaluating the statistics of the recorded data have been developed, though even then, current response in the range of voltage a significant magnitude above the onset threshold is generally not taken into account by these models, as the current can exhibit a falling-off or oscillation in the high voltage range, which does not match theoretical predictions. To examine these models, and to create a new means of optimizing models to the specific system under consideration, a large variety of models and ranges have been methodically examined to investigate their relative differences and to compare against prior literature on similar systems. Due to the importance of applying BEEM measurements of interface characteristics to many different spatially-resolved points and surface morphologies, having a consistent and precise means of evaluating the shift, degradation or systematic change relative to an established central tendency can allow a greater understanding of various material systems important in device fabrication.

The models typically used for Schottky barrier extraction and analysis of BEEM data do not perfectly match with the combined theoretical model taking into account all the effects of quantum mechanical reflection, cases in which transverse effective mass exceeds free electron mass, the tip-sample distance varies, nor those materials for which the conduction band minimum is not zone-centered, but instead, a simpler model better fitting experimental data is used, for example the original $e(V - V_b)^2$ model proposed by Bell and Kaiser [30] or the slightly

corrected $e(V - V_b)^{5/2}$ model proposed by Prietsch and Ludeke to better take into account the effects of quantum mechanical reflection and potential current loss from inelastic scattering owing to variations in the mean free paths of transmitted electrons. [31] However, the difference between these models is small near the barrier threshold under consideration, and both models only hold within a limited range above the threshold, owing to a slight tapering off in current for high voltage past the barrier threshold. This range is itself not a strictly well defined value, but is typically taken to be 0.2 eV. [21, 32] Because of this, it is necessary to tailor the basic model provided by Bell and Kaiser to a more practical model applicable to the energy region just above the barrier. To this end, a variety of models have been employed, including the commonly used fixed-exponent model [30], the also well studied linearized model [21], as well as a logarithmic model and a more elaborate model based on work by Qin *et al.* [7] which takes into account current below the threshold. In order for these models to be applicable, however, the width of the near-threshold range above the Schottky barrier must be determined.

The remainder of this chapter covers the process of optimizing the interval over which these models are applied, as well as the results of applying these models to the intervals determined by this optimization process. The specific models covered are the simple quadratic model, a linearized version of said model, fit with a logarithmic function determined based the quadratic model, and a piecewise expansion of the basic theoretical model about the threshold, which has been constructed to take into account the not otherwise modeled effect from current present below the threshold voltage.

5.2 Interval Optimization

In order to ideally match the recorded data, the models must be fit to a limited range above the threshold voltage, as a result of the simplified Bell-Kaiser model only having limited predictive ability for high levels of ballistic current transport. However, as the purpose of the fitting procedure is to determine the best possible value for V_{sb} , in principle a simplified model accurate only in the immediate vicinity of the threshold is still valuable for giving a precise and consistent estimate of the threshold location. The resulting issue is that there is no definite theoretical value for the range above the threshold beyond which the approximation begins to break down, meaning that some optimization is necessary, in this case by trying all possible threshold widths to see which provides the best explanation of the data, as measured by adjusted R^2 .

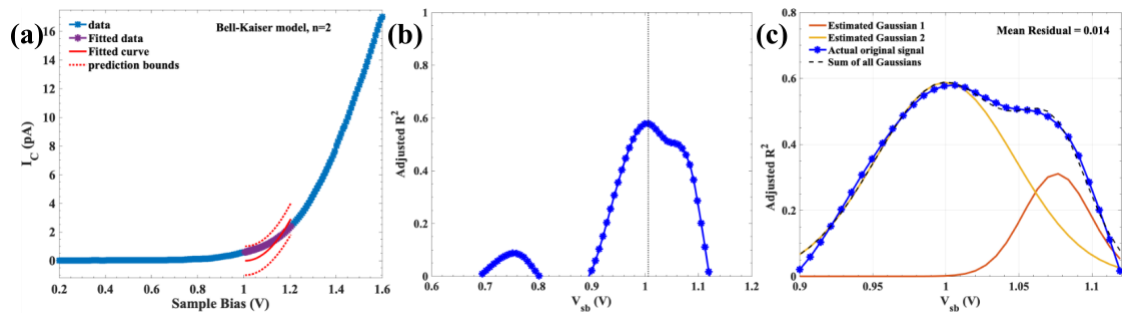


Figure 19: a) Illustration of the full spectrum of current response compared with the 0.2 eV interval fit described above. This gives a value of $0.9996 \sim 1.00$ eV for the threshold. b) Illustration of the process of finding the value of V_b which optimizes adjusted R^2 for a fixed 0.2 eV interval, applied to a simple implementation of the model originally proposed by Bell and Kaiser (the BK $n = 2$ model). Note that there are actually three local maxima, with only the highest being marked as the optimal approximation of V_b . For other intervals, one of the other local extrema may dominate. c) Double Gaussian fit of the above distribution of possible threshold locations, with a comparison between the sum of the two Gaussian curves and the actual signal.

To illustrate this optimization, the basic model with an exponent value of 2, that is, $C(V - V_b)^2$, is used to show, first of all, the process of determining the barrier height through multiple Gaussian fits and adjusted R^2 optimization, using the 4-point line scan (as shown in Figure 16), the experimental details of which are described in Chapter 4. This technique consists initially of sweeping across all possible values of V_b and fitting the region 0.2 eV above the threshold, which is considered a test parameter of the model. This window was first decided upon in accordance with previous studies by Balsano *et al.* and Andres *et al.* on various metal/Si(111) heterostructures, which suggest that 0.2 eV is the optimal window for this model to be accurate above the threshold, before the near-threshold behavior originally predicted by Bell and Kaiser breaks down. [21, 32] The approximate value of V_b is then approximated as the value for which the fit has the highest possible adjusted R^2 , with such a fit being shown in Figure 19a, and the corresponding adjusted R^2 value being noted as the highest maximum of all fits in Figure 19b. In Figure 19a we show the fitted curve along the predictive bounds of the estimation. In cases where there are multiple maxima, these values can be extracted through a multiple-Gaussian fit as shown in Figure 19c. This fitting method extracts the Schottky barrier height to be approximated as 1.00 eV.

The existence of multiple local maxima in R^2 seems to suggest that the 0.2 eV fitting interval may not be appropriate for this sample. For some fitting widths, other features of the data may be erroneously fixated upon via this method, as a

result of the interval width not matching the width of the near-threshold region wherein the chosen model holds. For certain intervals, the threshold value which gives the best possible value of R^2 may be different from the one highlighted in Figure 19b, as for example, a small feature of the data arising from external noise, current leakage, parasitic capacitance, or any other systematic error not taken into account by this model may fit better than the real region being searched for when sweeping the data with a small interval. As a further example, one such interaction which this model does not consider is the effect of strong elastic scattering at the Au/GaAs interface, which may contribute an additional non-exponential attenuation of BEEM current in the region just above the Schottky barrier threshold.[23] This non-exponential factor could possibly contribute to the existence of a small feature below the threshold which creates a local maximum in the adjusted R^2 when scanning for the best possible threshold. To circumvent this issue and find the best possible interval, the interval itself was then optimized to find one which yielded the best approximation of V_b .

This higher energy region being fit by this model can be varied from the entire remaining above-threshold spectrum, to only a small window above the threshold, to determine the optimal width of the near-threshold region. From these fits, the maximum adjusted R^2 for each interval size can be plotted across all possible near-threshold region widths. The fit corresponding to this maximum can be taken as the best possible application of the chosen model across all possible thresholds and windows of fitting. In order to determine the best possible model, each of the models suggested by various literature sources was individually evaluated based on the value of V_b given by this method of optimizing R^2 for all possible fitting intervals above 0.2 eV and choosing the one which gives the best possible optimized maximum for this measure of best fit. The resulting fit, plotted in Figure 19a, shows the data within the given range falling well within the prediction bounds of the model, though the fit is not perfectly aligned with the data.

5.2.1 Models

Fixed Exponent

$$I_c \sim C_1(V - V_b)^2 \quad (38)$$

For the first model, the simplest possible quadratic model, which was inspired by the initial formulation of the problem provided by Bell and Kaiser in 1988, was initially used to determine the viability of fitting to find the Schottky barrier threshold. [30] The results are shown in Figure 20, with all possible fitting intervals and threshold values tested. Figure 20a shows the final result of this process, with the quadratic fit slightly diverging from the data near the threshold, but fitting it with a high degree of accuracy for the high-voltage region, in contrast with what would be expected. In Figure 20b, the interval optimization method is shown, with

the fitting interval which gives the best possible adjusted R^2 for the final value of V_{sb} being taken as the optimal width of the near-threshold region to be fit. For this model, the near threshold model determined in this way covers a significant extent above the found threshold voltage, as a result of the nearly-quadratic response of the overall above threshold current in this measurement. Figure 20c shows the difference in final threshold values found when using different near-threshold fitting windows. Corresponding to the two local maxima shown in Figure 20b, there are two clear "plateaus" in the final value of V_{sb} , as slight variations in the fitting window do not result in significant changes in the threshold value found by this method. The boundary between these two overlapping peaks in Figure 20b can be seen to correspond to a discontinuity in the final threshold value found in Figure 20c, which in turn would seem to correspond to nearly-quadratic feature of the data which does not take into account the full extent of the data above the threshold.

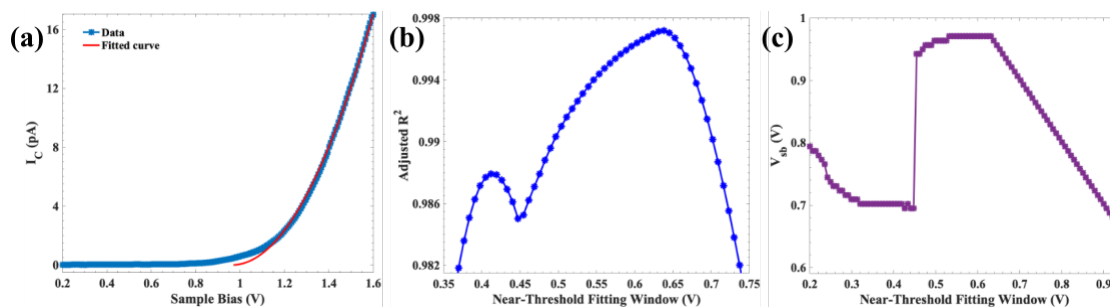


Figure 20: a) Illustration of the full range of BEES data compared with the 0.6384 eV interval fit described above. This gives a value of $0.9636 \sim 0.96$ eV for the resulting threshold value. b) Illustration of the issue of multiple local maxima in R^2 for various fitting window widths. When fitting over a smaller region, a weaker fit is produced corresponding to a threshold value significantly below literature values. c) Selection of optimized V_{sb} values for different fitting windows, showing the two values which correspond to local maxima in R^2 , with a discontinuous jump between them. The higher value represents a higher maximum R^2 , for a final value of $0.9636 \sim 0.96$ eV.

Linearized

$$\sqrt{I_c} \sim C_2(V - V_b) \quad (39)$$

The simpler, quadratic method described above was then subsequently iterated upon by effectively linearizing the data relative to the previous exponential model through a simple square-root, in order to create a linear dependence near the threshold. By fitting this threshold to the intersection of the new, linear fit, with a separate linear fit for the low-voltage sub-threshold region, the intent was to

thereby reduce the influence of sub-threshold noise and find a better estimate of the actual barrier height. This method incorporates the linearization fitting employed by Balsano *et al.* in 2013. [21] In Figure 21, similar results to those of the quadratic model are shown. However, the linear model used requires the intercept with the zero ballistic current floor to be taken as the threshold value, as the linear model does not take into account the exact near-threshold current uptake curve, but rather fits the higher voltage region which is extended backwards in voltage to find the zero-current level when ignoring this near-threshold curve. To find this intercept, the square-rooted below threshold voltage is fit with another linear fit as a means of finding the approximate current floor of the system, with the result being shown in Figure 21a. Figure 21b and Figure 21c show very similar results to the analogous results for the prior model, though in this case there is greater overlap between the two local maxima in adjusted R^2 , with a slightly less clear "plateau" region in the V_{sb} values found for threshold values near the threshold value which maximizes adjusted R^2 .

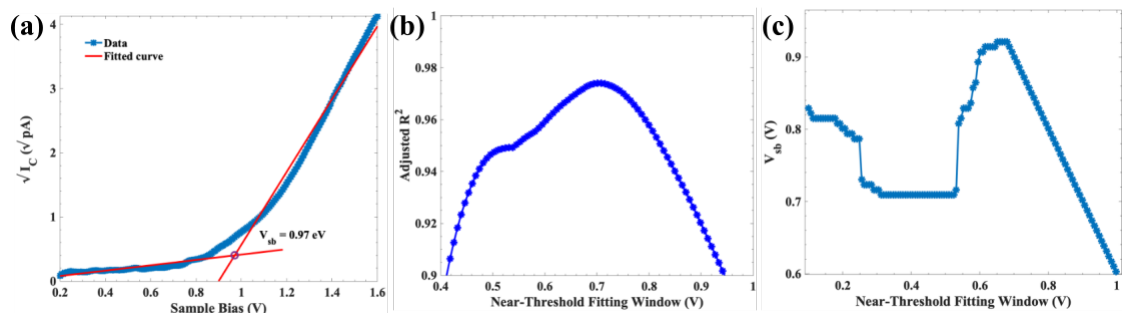


Figure 21: a) Illustration of the full linearized BEES data, which has been fit with a linear model. In this case, both the sub-threshold and the near-threshold regions are approximated as roughly linear, and the intersection of the sub-threshold region with the simple linear fit done of the near threshold region is taken to be the true threshold value. b) Illustration of the issue of multiple local maxima in R^2 for various fitting window widths. Here the two local maxima are nearly overlapping, which would inhibit the utility of trying to do a multiple Gaussian fit. c) Selection of optimized V_{sb} values for different fitting windows in the linearized model, similar to that of the simpler model shown in Figure 20c showing the two values corresponding to local maxima in R^2 . For this model, the higher value is somewhat less well defined than in the quadratic model, with the higher value representing a higher maximum R^2 , for a final value of $0.9707 \sim 0.97 \text{ eV}$.

Logarithmic

$$\ln(I_c) \sim C_3 \ln(V - V_b + 1) \quad (40)$$

A similar method was next attempted, with the modification that the exponent is not assumed to be 2, as this exponential value is typically used as a simplified approximation of the Bell-Kaiser model, which may not be perfectly accurate for all experimental systems. A logarithmic model is used above the threshold, with the intersection of the two regions being considered the threshold. In this model, the natural logarithm of the data is taken, and the resulting data is fit, with the polynomial exponent absorbed into the coefficient treated as a parameter of the model. The resulting best fit is then used to find the intercept with a linear fit of the sub-threshold current, with this intercept being taken as the barrier height, similarly to the process for the linear model. Using this intercept method takes into account any possible variation in the exponential curvature of the sub-threshold

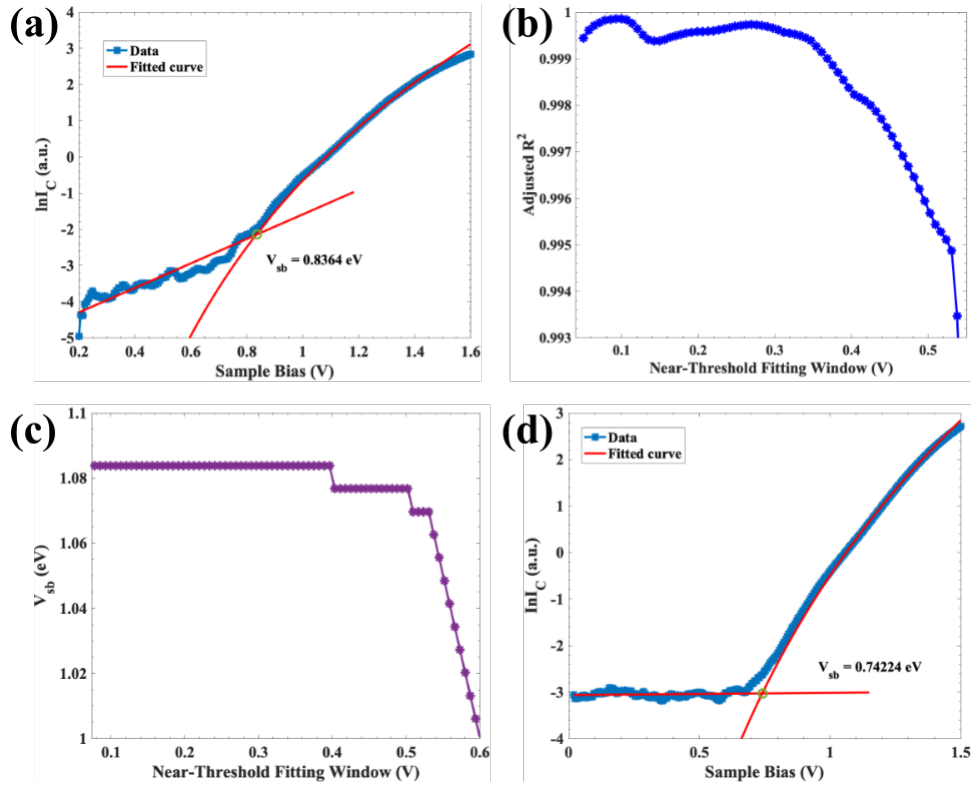


Figure 22: a) Logarithmic fitting of the full spectrum transformed BEEM response, which has been fit with a linear model below the threshold similarly to the linear model process shown in Figure 21. This data is taken from the second, 4-point line scan taken on March 23rd, 2021. b) Illustration of the issue of multiple local maxima in R^2 for various fitting window widths. c) Selection of optimized V_{sb} values for the logarithmically transformed model. d) The full logarithmically-transformed BEES data fit in the same way as a), using the data from the initial 16-point line scan taken on March 18th, 2021 to standardize the process.

current prior to logarithmic transformation. The apparently somewhat linear nature of the sub-threshold region under this transformation seems to imply a roughly exponential form in this sub-threshold current prior to logarithmic transformation.

Figure 22a through Figure 22c show the process of interval optimization for the best line scan data taken as in prior models. In Figure 22b, which shows the adjusted R^2 across all the near-threshold fitting windows attempted, the model clearly has a higher explanatory power for smaller thresholds below the 0.5 V level, with one particular maximum lying at around 0.1 eV. In this case, there are clear plateaus in the value of V_{sb} found for low threshold widths, as may be seen in Figure 22c, without the significant discontinuities displayed by previous models when sweeping across a range of possible threshold values. This may possibly imply that the logarithmic model is significantly less accurate outside of the most immediate possible region to the threshold when compared with other possible transformations and models. This process was replicated for the initially attempted line scan, presented in Figure 22d for which the response below the threshold is apparently more constant, which may imply a less clearly exponential character of the current response prior to transformation below the threshold.

Sub-threshold

$$I_c = \begin{cases} R(kT)^2 e^{\frac{eV - V_b}{kT}}, & \text{for } eV \leq eV_b \\ R(kT)^2 \left[1 + \left(\frac{eV - V_b}{kT} \right) + \frac{\left(\frac{eV - V_b}{kT} \right)^2}{2!} \right], & \text{for } eV > eV_b \end{cases} \quad (41)$$

In the most analytically elaborate model attempted, a piecewise function was used to more precisely evaluate the sub-threshold current response, rather than simply approximating all values near zero to a linear function. This model, explained in more detail in the section on the theoretical background of BEEM, consists of a second order polynomial expansion above the threshold, with shifting applied from the sub-threshold current included as an exponential function below the threshold, which is adapted from the form given by Qin *et al.* [7], which results in the above experimental form given in Equation 41.

The results of optimizing and applying this model are shown in detail in Figure 23, with Figure 23a showing that outside of the highest voltage range, the model seems to very closely match the real data, which can be seen in the inset focusing on the region immediately about the found threshold value. In terms of adjusted R^2 for the various intervals examined, as investigated in Figure 23b, it appears that for sub-threshold fitting, there are several local maxima in the small-window range, but none in the higher threshold range. In fact, the optimal resulting interval fits closely to the previously assumed literature value of 0.2 eV, at 0.2202 eV. However, the other local maxima have roughly similar magnitude, and therefore may not correspond to significantly different threshold values. In Figure 23d, the

optimal threshold found in this way is 0.3192 eV as a result of the local maximum corresponding to a higher threshold window being found to be higher than the one near the 0.2 eV mark. This may be the cause of the slightly higher final value

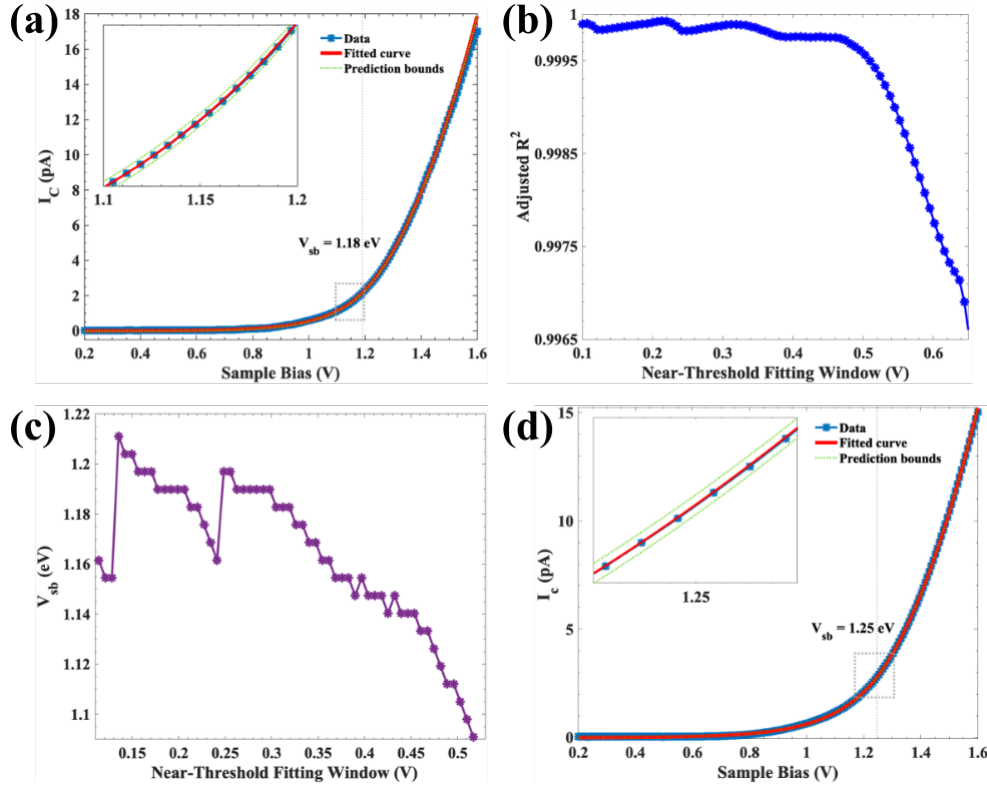


Figure 23: a) The full sub-threshold model applied to the un-transformed BEES data. b) Illustration of various local maxima in R^2 which occur during interval optimization using this method. c) The many different optimized V_{sb} values found when varying fitting windows during this process, showing significantly greater variation in the final threshold value in regards to the fitting window relative to the other models attempted. However, the region of interest is still on the smaller side, with higher thresholds not resulting in any apparently stable value. d) The full-spectrum fit equivalent to that in a) for the first 16-point line scan recorded on March 18th 2021, with a final value for the threshold voltage, as well as a slightly larger optimal fitting window resulting from one of the larger-threshold peaks overtaking the one at ~ 0.2 V.

of V_{sb} for this measurement. While it is interesting that different measurements have significantly different optimized near-threshold fitting windows, it is likely a result of a difference in the material location of the measurement, with a less clean interface possibly resulting in a quicker deterioration of the expected response.

Figure 23c supports the idea that there may be slight differences in the final threshold value for different measurements, as the value of V_{sb} for the different fitting windows tested have much less clear plateau regions than in previously attempted models, which correspond to the local maxima in adjusted R^2 which have similar magnitudes. Nonetheless, all these maxima corresponding to low-width fitting windows result in final adjusted R^2 values very close to 1, implying a good fit regardless of slight differences in fitting window width for this model.

5.3 Results

Method	$V_{sb} \pm 0.021eV$	Adjusted R^2	Fitting Window
Fixed Exponent ($n = 2$), Fixed interval	1.00 V	0.5799	0.2 V
Fixed Exponent ($n = 2$)	0.96 V	0.9972	0.6384 V
Linearized data ($I_{BEEM} \rightarrow \sqrt{I_{BEEM}}$)	0.97 V	0.9739	0.702 V
Logarithmic fit ($I_{BEEM} \rightarrow \ln(I_{BEEM})$)	0.84 V, 0.74 V	0.9999	0.0995 V, 0.346 V
Sub-threshold current included [7]	1.18 V, 1.25 V	0.9999	0.2202 V, 0.3192 V

Table 1: Schottky barrier thresholds found through applying various optimized models to an atomically clean Au/GaAs interface grown *in situ* in an ultra high vacuum MBE enclosure.

Table 1 gives the end results from all the models discussed above, from the initial attempt with a quadratic model and a fixed 0.2 eV fitting window, to the four different interval-optimized methods using the quadratic, linearized, logarithmic, and sub-threshold models. The first column gives the rounded final values of V_{sb} , with the logarithmic and sub-threshold models having values for first the 4-point scan and then the 16-point scan, with all values having an experimental deviation of ± 0.021 eV. The next column shows the adjusted R^2 values for each model, with all models having a final value close to one, with the exception of the initially attempt at implementing the quadratic model.

Adjusted R-squared is used as the characteristic statistics under the classic definition

$$R_{adj}^2 = 1 - \left[\frac{(1 - R^2)(n - 1)}{n - k - 1} \right] \quad (42)$$

with n being the number of total data points, and k the number of parameters in the model. This gives an estimate of the goodness of the fit from residual magnitude which takes into account the number of parameters applied in order to prevent over-fitting the model.

Finally, the third column gives the optimized fitting window for each model. Of particular note is that both the logarithmic and sub-threshold models give significantly lower optimized threshold values than the linearized and fixed interval methods, which would likely mean that these models fit better when focusing solely on the near-threshold region, while the other two models work better at giving a quick approximation of the general above-threshold current in the higher voltage range.

These results can be compared to the statistically compiled values provided by Forment *et al.* for samples fabricated by electrochemical and thermal evaporation deposition methods, rather than molecular beam epitaxy, evaluated using a linear model. [20] However, differences in annealing processes and doping may also contribute to differences in result. [26]

	Thermal Evaporation Deposition Sample 1	Thermal Evaporation Deposition Sample 2	Electrochemical Deposition Sample 1	Electrochemical Deposition Sample 2
Φ_B (eV)	0.880	0.883	0.985	0.984
σ (eV)	0.019	0.018	0.032	0.029
N	233	197	222	241

Table 2: Statistical comparison of Schottky barrier values found via linear fitting for a large sample size of different measurements on multiple samples fabricated through either thermal evaporation or electrochemical deposition. Φ_B is the height of the barrier potential, σ is the standard deviation of these values, and N is the number of measurements on each sample.

For the thermally evaporated samples, these results are significantly lower than those found for this sample, though the electrochemical deposition samples provide a closer match, despite the deposition method for the sample studied here being through an electron beam physical vapor deposition e-gun cell used as part of a high-precision ultra high vacuum MBE *in-situ* fabrication environment. Of particular note is that the model which gives the best quality of fit as determined by adjusted R^2 as well as by simple visual inspection also gives a significantly higher final threshold value compared to literature values. This likely results partially from a slight difference of definition, as the threshold value can be interpreted as the point at which a fit of the expected near-threshold response intersects with a

nearly zero noise floor, whereas in the model which fully considers sub-threshold current, the intersection of the above-threshold and below-threshold models are by necessity continuous, resulting in better overall fit where the quadratic segment

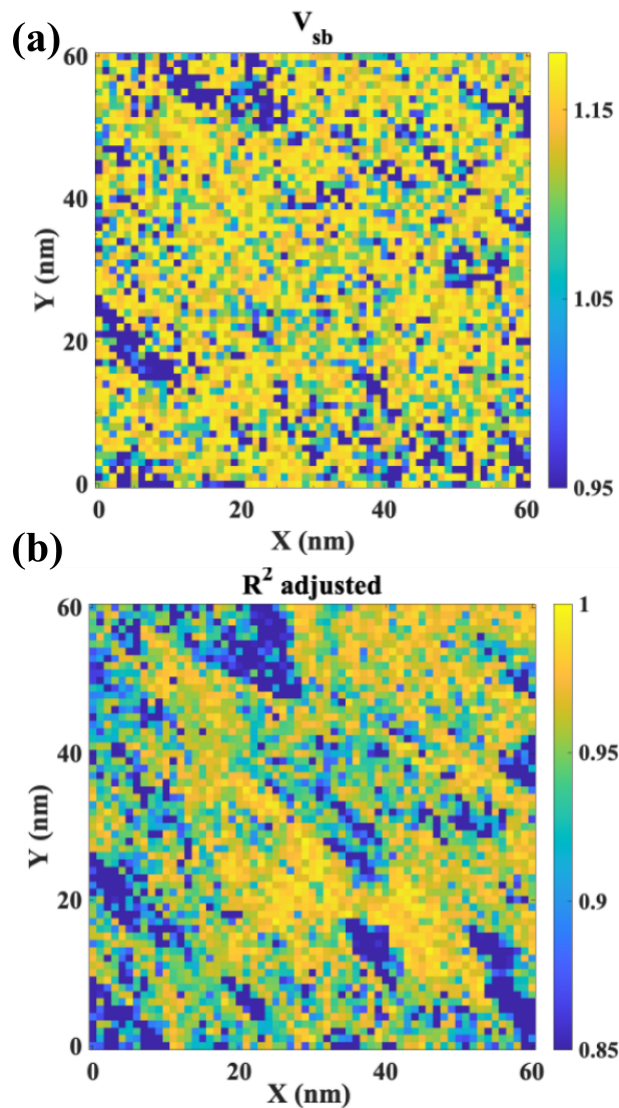


Figure 24: a) Spatially-resolved 2D map of Schottky barrier height found using the sub-threshold model. b) The adjusted R^2 value of the fit. In contrast to the method used in 18, which uses an 0.2 V fitting window, this extraction uses an optimized 0.3192 V fitting window, resulting in a set of adjusted R^2 values which fall almost entirely in the range of 0.85 to 1, slightly higher than the roughly 0.8 to 0.98 range found in the previous model.

of the fit is applied to a slightly higher region which is above what other models would consider the onset of ballistic transport. However, differences in fabrication procedure and measurement location could also result in different models having significantly different values as a result of variance in interface-level conditions. Regardless, the sub-threshold model is very precise in its estimation method, providing a consistent basis to analyze the spatially-resolved changes in interface characteristics of a sample, as has been done in the example of a large area 2D map as shown in Figure 18, which uses a near-threshold fitting width of 0.2 V, in accordance with prior literature. In contrast, when compared to Figure 24, which uses the fitting window of 0.3192 V found by optimizing the sub-threshold model for the initial 16-point line scan, the results show a slightly more condensed spread of threshold values, and a slight apparent increase in overall adjusted R^2 value.

6 BEEM Investigations of Metal-2D Electron Gas System

6.1 Introduction

The samples discussed in the last chapters, consisting of Au/GaAs Schottky contacts and Au/Ti/GaAs contacts, were a necessary step in standardizing and interpreting the process of recording detailed BEEM information and were used for measuring ballistic transport across the Schottky barrier. As a successful attempt at finding the expected Schottky barrier response, this system can be applied to various other samples. The results of the standardized technique can be used to interpret changes in the electronic properties of buried interfaces resulting from a particular band alignment and the Fermi level pinning effect caused by states at the interface. A particularly significant implementation of this method is the study of 2-dimensional electron gasses (2DEG), which form from the 2-dimensional confined states found in semiconductor quantum wells bounded by two interfaces with insulators or wide band gap semiconductors. One notable variety of device where this system is expected to be implemented is in optimizing the fabrication processes necessary to fabricate a 1-dimensional quantum nanowire capable of forming Majorana zero modes upon inducing superconductivity and magnetism, which could be used in the development of a topological quantum computer. Understanding the detailed electronic properties and the band alignment of such semiconductor heterostructures and superconductor-semiconductor interfaces is necessary for these kind of technological applications. The detailed analytical properties of such a device are discussed in further detail in a later chapter. If it is not first possible to fabricate a metal-semiconductor junction with an extreme degree of precision, it would likely eliminate the possibility of creating the Majorana modes necessary for such advanced devices, resulting from the presence of parasitic states at the interface which may degrade such a system. [33] In the interest of testing the experimental system further, and as an examination of the response of such a system to attempts at BEEM measurement, a structure composed of patterned depositions of Al on InAlAs/InAs substrate, with an insulating barrier on top and substrate underneath was fabricated to create a precisely controlled 2DEG, confined in the InAs layer. The ultra-thin layer of buried InAs below the insulating InAlAs layer hosts a 2DEG, as a direct consequence of the 2D quantum confinement of the electronic Bloch states of this material along the vertical (z-direction) axis of the sample.

The following sections investigate the fabrication, electronic band structure and ballistic transport characteristics of this sample in detail.

6.2 Experimental Setup

The 2DEG slab component of this sample was grown on an atomic hydrogen cleaned InAs(001) wafer, with the active 2DEG region consisting of 24 nm of InAs grown at a temperature of 480°C at a rate of roughly 0.5 ML/sec. Aluminum was then deposited at down to 140K substrate temperature to a thickness calculated to be nominally 12 nm at a growth rate of 0.74 Å/s, at a cell base temperature of 1200°C through an MBE effusion cell for 2 minutes and 42 seconds. A silicon stencil mask was used to create rectangular wire-like structures as shown in Figure 25a. These structures were measured by STM to have a height of about 9 nm and a width of about 1.3 μm. Similarly to the previously tested sample, ballistic transport

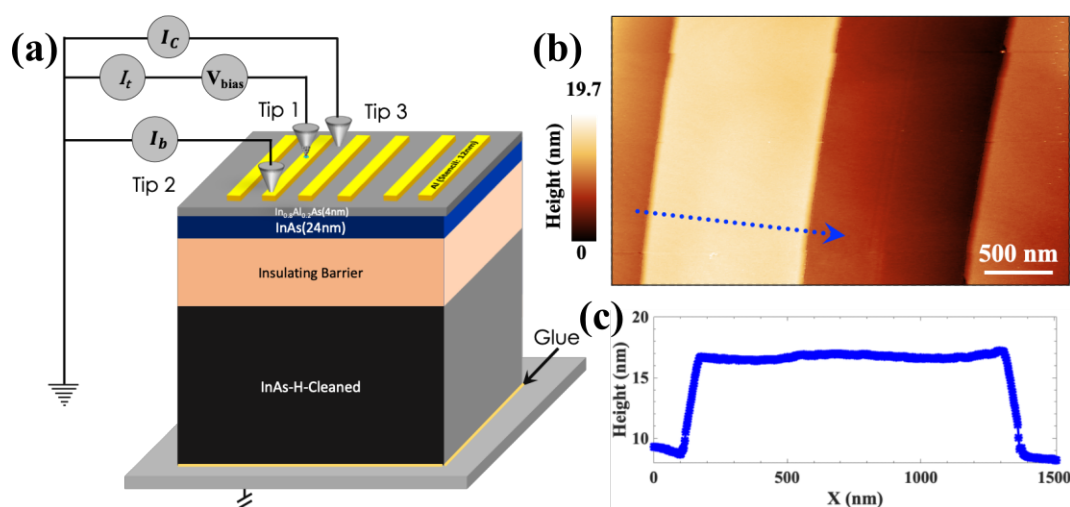


Figure 25: Detailed inspection of the setup configuration for the attempt at BEEM through a buried 2DEG layer. a) Schematic of the scanning circuit and sample, with 12 nm of aluminum deposited in rectangular strips through a patterned stencil mask similar to the circular depositions of the previously described sample. The underlying substrate is composed of hydrogen-cleaned InAs, with other wide band gap semiconducting materials layered on top of it to create a barrier insulating the near surface region from the substrate. This creates a near-surface quantum well composed of 24 nm of InAs covered with 4 nm of $\text{In}_{0.8}\text{Al}_{0.2}\text{As}$, with the comparatively very wide band gap of the aluminum indium arsenide layer causing the 2DEG confinement effect in the InAs layer, similar to that of a traditional particle-in-a-box model. b) STM topography of one of the Al strips. c) Height profile taken across the dotted line shown in b), which verifies the approximately 9 nm height of each rectangular deposition.

measurements were performed on the Al wire-like structures by submerging the

tip of one probe, $T2$, into an Al structure to be measured later (with the tunneling probe $T1$), while a third probe $T3$, was submerged into the underlying substrate separately. The top 4 nm of InAlAs was methodically scratched with this tip $T3$ to remove a significant portion of material from this surface layer of InAlAs, and was then submerged below it into the 24 nm InAs layer below.

The above process was verified using the attached SEM setup to make certain of the locations of the tips, and that the removal of the InAlAs surface layer was performed as expected.

As a result, current measured through this tip, I_c , may have included contributions from ballistic transport through the Al structure into the conduction band of the InAlAs, as well as from ballistic transport through both the Al structure and the InAlAs barrier to the InAs confined quantum well. The width of the InAlAs barrier is of particular importance to understanding this system, as this barrier controls the ability of confined states in the InAs layer to interact with the metallic states from Al layer on top which would be expected to play an important role in the proximity effect when superconductivity is induced.

The problem of poor lattice matching was avoided because the aluminum indium arsenide used was chosen as a insulating barrier to create a close match with the lattice constant of InAs, allowing epitaxial growth to be possible. Moreover, Al grown as a continuous layer on InAlAs without the creation of individual Al grains of widely varying crystal orientations of height in the metallic layer. This also affects the interface characteristics, as it reduces the scattering and reflection present at the interfaces with the Al deposition, and allows for a smooth band transition.

6.3 Experimental Results

The ballistic current measurements for this sample were performed through the metallic Al wire-like structures. Before starting these spectral BEEM measurements, a significant amount of STM scanning was first done on these Al wires, using both tips $T1$ and $T2$, which served the purpose of stabilizing these tips such that any piezoelectric drift present in the system could be eliminated. Meanwhile, $T3$ served as the grounding contact for the collector current I_c . measured through the InAlAs and InAs layers. Figure 25b shows a large area STM topographic scan, with two of the wire-like Al thin film structures present, with an InAlAs valley dividing them. A height profile taken across the Al wire is marked by the arrow and dotted line in Figure 25b, contrasting the height of the Al structure to the surrounding InAlAs is shown in Figure 25c. From this profile, height and the width of the wire can be estimated to be 9 nm and 1.22 μm respectively. At 77K, the range of the scanner is around $3\mu\text{m} \times 3\mu\text{m}$, which is what makes it possible to measure such large structures in STM.

BEEM measurement was performed using an external lock-in amplifier to modulate the z-direction piezoelectric component of the scanning probe ($T1$) with an applied reference frequency chosen to be a prime number, so as to avoid any

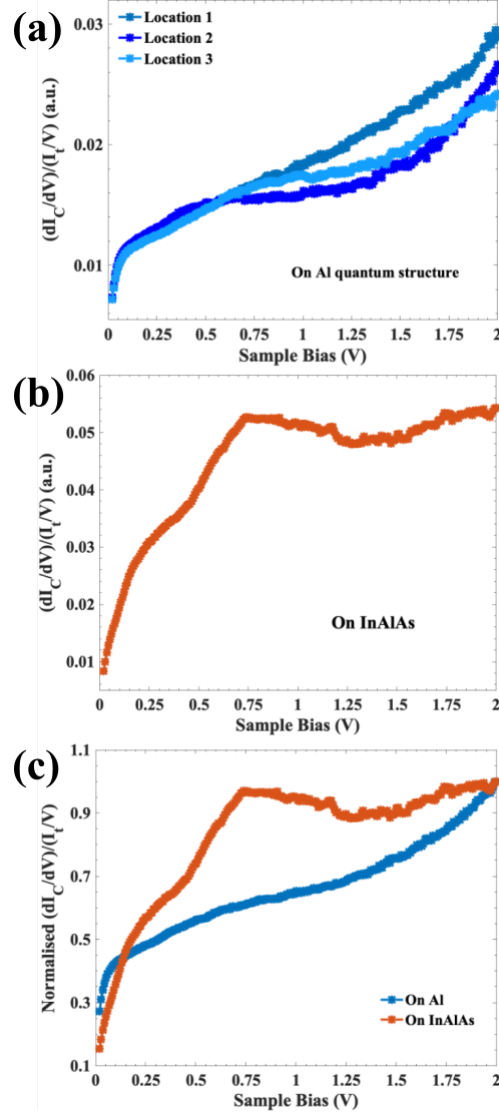


Figure 26: BEEM measurements recorded using an external lock-in amplifier to give dI_c/dV a) The derivative of the ballistic current response at three different locations on the Al structure. b) In comparison, the derivative of the ballistic current response not on the Al structure, but on the underlying InAlAs layer. c) The normalized results from a) and b), with all three measurements in a) averaged to a single curve, showing a clear smoothness in response on the Al structure not present when looking at the off-structure response.

overlap with environmental noise modes. This causes the tunneling current to be modulated by the same frequency, sinusoidally oscillating the tip-sample distance of the tunneling probe, with the typical STM feedback loop being activated to maintain constant current, similarly to that done for prior measurements on the previous sample. Rather than applying the AC-modulation directly to bias voltage, this method of z-direction piezoelectric modulation allows for a better energy resolution by eliminating the contribution to the variance of the measurement from the AC bias modulation amplitude applied to the bias voltage of the sample. This subsequently allows transmission spectra to be measured in the dI_c/dV form on both the Al structures and the underlying InAlAs layer. In Figure 26a we show the voltage derivative BEES response as a function of the sample bias voltage on an Al wire at three different locations. These data do not show the typical BEES response as we have considered for the case of Au/GaAs heterostructures in Chapter 4. We repeated these experiments at various locations, but this never resulted in the traditionally expected Schottky barrier BEEM current response. The spectra in Figure 26a appear to give a similar result regardless of the location tried on the Al structure. Ultimately, this data seems to clearly indicate that this system does not show any Schottky barrier-like feature at the interfaces through which current has been measured.

In Figure 26b we show a similar spectrum averaged over a large number of repetitions taken on the InAlAs surface. Unlike a typical BEES measurement for a sample with a Schottky barrier, this spectrum shows no zero-current level below a certain range of bias voltages, as would typically be considered the result of a barrier at the interface. As a result of the more elaborate three layer material system considered in this experiment, the resulting BEEM response is significantly more complex to evaluate than in the prior tests. Developing a full understanding of this system is beyond the scope of this thesis, though it may be a very significant and productive undertaking to further investigate the detailed transport characteristics of a similar sample for industrial application, using all possible analytical techniques.

This system contains two interfaces, namely, the Al/InAlAs interface and the InAlAs/InAs interface, which were fabricated in series. The response shown in 26a clearly does not match the response expected when performing an analogous measurement of an Au/GaAs system as in 16c in which an interface creates an associated energy barrier. A comparison between BEES measurements, normalised to their respective maxima, measured on Al and on InAlAs is shown in Figure 26c. This comparison indicates that in the forward-biased scan, that is, the bias voltage region above the Fermi level, there is no evidence of having any barrier in either the Al/InAlAs or InAlAs/InAs interface. Ordinary BEES has been performed without involving a lock-in amplifier during measurement, but nonetheless, no

BEES threshold resembling a Schottky barrier at the interface was found. In order to understand these BEES data, we performed theoretical simulations using the self-consistent Schrödinger-Poisson method [34, 35] and $\mathbf{k} \cdot \mathbf{p}$ perturbation theory, [36, 37] as described in the next subsection.

6.4 Simulation

To better understand the band alignment of the heterostructure, two kinds of electronic simulations were used to develop a better understanding of the system. First, the self-consistent Schrödinger-Poisson method was used to find the conduction band alignment of the two semiconductor surface layers and their interface, as well as the first four states located in and above the InAs well. A similar simulation was performed using $\mathbf{k} \cdot \mathbf{p}$ perturbation theory. Despite the fact that these simulations were not performed for the same layer thicknesses as the sample measured here, they give a clear picture of the band structure of a sample with a confined 2DEG InAs layer separated from the sample by an aluminum indium arsenide layer. In particular, the confined state energy corresponding to the 2DEG in InAs layer can be examined, and a rough estimate of the order of magnitude potential barrier presented by the InAlAs layer.

Schrödinger-Poisson (SP) Simulation SP simulation, in basic principle, consists of alternatively solving Poisson's equation for electric potential and Schrödinger's equation for particle density with the output of each being adjusted and then input into the next step of the loop, until a stable value is determined. In greater detail, the steps are as follows. First, the Poisson's equation

$$-\nabla \cdot (\epsilon \nabla V) = \rho \quad (43)$$

where V is electric potential, ϵ is the material permittivity and ρ is the charge density, is taken initially as a rough estimate using initial values of an intuitively reasonable order of magnitude. Secondly, this V is converted to a potential energy V_e through the equation

$$V_e = z_q e V \quad (44)$$

where z_q is the charge number and e is the elementary charge.

This updated potential is then input to the Schrödinger equation to produce a set of eigenenergies E_i and corresponding wave functions Ψ_i , which is then fourthly used to compute the particle density profile n_{sum} from a statistically weighted sum of the resulting probability densities as follows:

$$n_{sum} = \sum_i |\Psi_i|^2 \quad (45)$$

where N_i is the weight factor given by integrating the Fermi-Dirac distribution for the out-of-plane continuum states, which in 1D corresponds to the equation

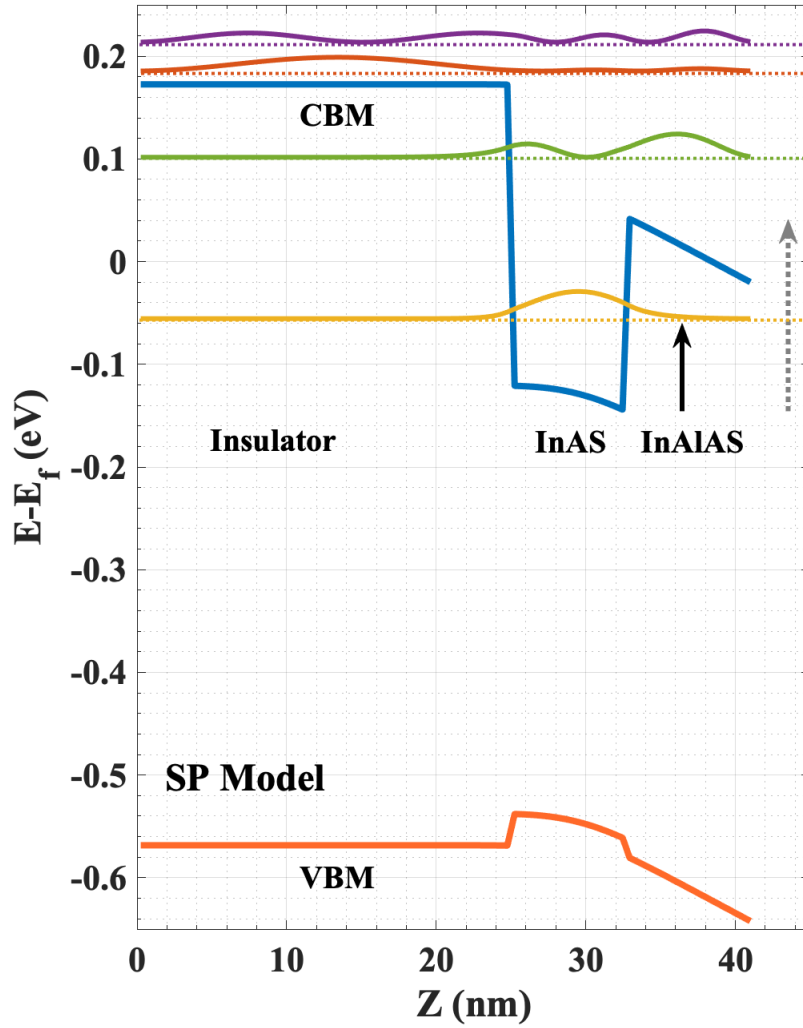


Figure 27: Schrödinger-Poisson self-consistent simulation of the 1D electrostatic potential in the sample, showing the conduction band alignment along the depth of the sample, with the InAlAs surface being located to the right, at the maximum z -value. Also shown are the wavefunctions and energy positions of the four lowest energy states.

$$N_i = g_i \frac{m_d}{\pi \hbar^2} k_B F_0 \left(\frac{E_f - E_i}{k_B T} \right) \quad (46)$$

in which g_i is the valley degeneracy factor owing to the symmetry of the band structure across the Brillouin zone, E_f is the Fermi level, k_B is the Boltzmann constant, T is temperature, m_d is the density of states effective mass (which corresponds to the geometric mean of effective masses combined with the degeneracy factor $m_d = \sqrt[3]{g^2 m_x m_y m_z}$).

To connect this back to Poisson's equation, the fifth step is to use n_{sum} to re-calculate the charge density $\rho = z_q e n_{sum}$ which can then be used to once again get the new potential profile V . However, in practical simulations, this value of ρ almost always diverges, meaning an adjusted estimate such as one including a commonly employed factor such as:

$$\rho = z_q e n_{sum} \exp \left(e^{-\alpha} \frac{-q(V - V_{old})}{k_B T} \right) \quad (47)$$

where V_{old} the previous iteration's potential output, and α is an external tuning parameter included to take into account any possible inaccuracies of Boltzmann statistical approximation for low temperatures. This process can then be repeated until the final output, ρ_{new} or $n_{sum,new}$ is equal to the old value ρ_{old} or $n_{sum,old}$ within a preset convergence value.

$\mathbf{k} \cdot \mathbf{p}$ perturbation modeling To verify and help interpret the results from the Schrödinger-Poisson, a similar simulation was performed using the formalism of $\mathbf{k} \cdot \mathbf{p}$ perturbation theory. This semi-empirical approach to modeling is characterized by the Bloch state Hamiltonian

$$\mathcal{H}_k = \frac{p^2}{2m} + \frac{\hbar \mathbf{k} \cdot \mathbf{p}}{m} + V \quad (48)$$

which can then be divided into the following components,

$$\begin{aligned} \mathcal{H} &= \mathcal{H}_0 + \mathcal{H}'_{\mathbf{k}}, \\ \mathcal{H}_0 &= \frac{p^2}{2m} + V, \\ \mathcal{H}'_{\mathbf{k}} &= \frac{\hbar^2 k^2}{2m} + \frac{\hbar \mathbf{k} \cdot \mathbf{p}}{m}. \end{aligned} \quad (49)$$

This Hamiltonian and dispersion relation can be applied to various band structures and extended to include spin-orbit effects, as a means of finding the effective mass and energy levels of states in a material.

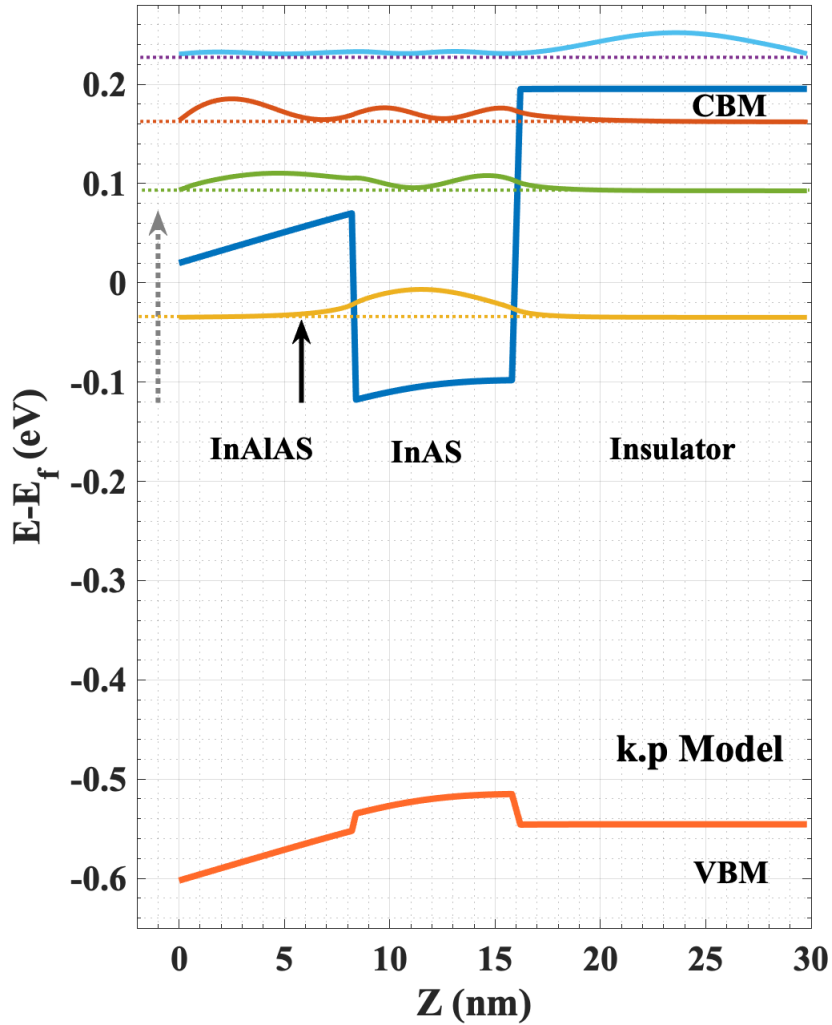


Figure 28: $\mathbf{k} \cdot \mathbf{p}$ simulation of the 2DEG material stack, with the valence band maximum in orange and the conduction band minimum in blue, with the energy levels and wavefunctions of the first four states also marked.

Comparison with the recorded data As can be seen in Figure 27, the above simulations gives a self-consistent confined state energy inside the square potential well created by the 2DEG stack. While not directly simulating the same system as those measured during BEEM standardization, these results show the associated states and electrostatic characteristics of a similar sample, presenting a qualitative framework for understanding the recorded data. Though the effectively insulating

materials deeper in the stack have little effect on the electronic properties of the sample, beyond allowing the sample to be materially fabricated without interface defects from lattice mismatching, the barrier and quantum well formed active region near the surface are evaluated for the same materials as the measured 2DEG sample, allowing some insight into the InAlAs barrier created by this sample.

The height of the InAlAs barrier found using this method seems to be around ~ 0.18 eV compared to the conduction band minimum of the InAs layer, with a distance in energy of a value close to 0.1 from the top of this barrier to the confined state simulated by the Schrödinger-Poisson method. Said value is roughly of the same order of magnitude as the dI_c/dV minimum, which appeared at the lowest end of the bias range of the measurement shown in Figure 26a. Representing the spectral BEEM response when measuring on Al, the sudden increase in current at around 0.1 V in applied bias could correspond to an emission energy which is able to pass through this barrier, with higher voltages passing current through the confined 2DEG state, estimated here to be located at around -0.05 eV. However, it is entirely possible that this phenomenon could arise from a different aspect of the sample not modeled in this project. Additionally, the effects of interface defects and associated interface states which may contribute to some shift in local band bending at the InAlAs/InAs interface are not modeled by this method. As it is unknown what states may exist at the interface between InAs and InAlAs, it is possible that this heterostructure contains in one of its interfaces or edges a metallic state, which could create a form of parasitic leakage current. If such a state were shown to exist, it would require more detailed characterization and analysis to interpret. These results also generally agree with the conclusions taken from the Schrödinger-Poisson model, with a layer of charge density confined in the InAs layer, though the simulated sample differs significantly from the one which was fabricated. In comparison to the Schrödinger-Poisson simulation, the $\mathbf{k} \cdot \mathbf{p}$ model gives a similar, though slightly smaller distance from the top of the conduction band minimum of the InAlAs layer to the confined 2DEG state formed in the InAs quantum well.

6.5 Conclusion

The results of the above simulation and analysis shows that there is not a Schottky barrier feature at the interface of the InAlAs layer with the patterned Al structures deposited on top of it. However, performing BEEM measurement through a tip buried below this InAlAs layer in the InAs layer underneath it seemingly allowed the current from the confined quantum well to be recorded instead, with very different results when attempting to measure ballistic current through the InAlAs bulk barrier than through an Al structure deposited on top of it. In order to further understand the details of this response, further simulation may be necessary.

7 Future Research and Conclusion

The wide variety of models for interpreting BEEM data, as well as the general difficulty of fabricating the relevant samples and developing the experimental system for recording such data presents a significant challenge when it comes to extracting relevant parameters in a consistent manner. When compared with literature values for similar samples, many granular differences in the details of both the fabrication method used and the particular applied model of data interpretation employed can result in a discrepancy of significant magnitude even when employing fairly consistent and well-supported statistical methods. However, the possibility of employing such models in a highly-controlled *in-situ* MBE fabrication facility provides the capability of further research into the electronic structure of buried interfaces, as is relevant when pursuing the creation of advanced devices such as those involved in predicted topological quantum computation systems.

7.1 Significance

Because the standardized methods presented here can be used on a variety of systems, there is no individual specific application which is the sole beneficiary of the employment of the BEEM experimentation process for *in-situ* MBE fabricated samples, as this process can be used in concert with other scanning probe techniques to give at least basic information or experimental confirmation of the existence and spatial consistency of the fabricated heterostructure. Specifically, however, this particular system is of particular relevance to the analysis of metal-semiconductor interfaces used in the fabrication of the 1-dimensional superconductor-semiconductor heterostructure nanowires necessary for the experimental verification of the predicted Majorana zero modes which may be present in such a system, which would present the possibility of creating a network of non-localized quantum information which could then in principle be used the implementation of quantum-based information processing in accordance with the basic theoretical principles of quantum computation as defined by the basic computational structure of a quantum Turing machine. [38]

7.2 Further Research

One possible experimental optimization which could have been employed is the use of an automatically determined tip conditioning process. There exist studies in which, for example, a machine learning algorithm is trained on a set of previously taken data, and this model is then in principle able to exit a measurement or operation cycle as soon as the response indicates that the tip is in an optimal state for measurement. [39] While there have been previous models developed to

tackle this problem, involving combinations of such methods as adaptive boosting, random decision trees and deep neural nets to create a decision based on multiple layers of weighted processing, there was not sufficient time available in this project to implement such a model, and all tip preparation was done manually.

In much the same way as the core technique of scanning probe microscopy has been widely expanded, in the intervening years since the invention of BEEM, many extensions have been developed, beyond those used in barrier height measurements for metal-semiconductor interfaces. The standard BEEM system can also be operated in reverse-bias mode, meaning the charge carriers emitted into the metal layer are holes, rather than electrons, causing electrons in the metal to be scattered over the Schottky barrier, though this results in a lower transmission level as a result of the inelastic scattering. [40] Hot-carrier measurements, which can provide the attenuation length of the metal by varying the thickness of the metal thin film and recording the percentage of transmitted current for a well-defined bias voltage, can take advantage of this reverse bias scattering to compare differences in attenuation length with the forward bias mode. [41]

While the high voltage necessary to pass current through an insulator may present challenges, there have also been studies where BEEM techniques have been applied to find barrier heights at insulating interfaces, such as through the native oxide layer of a Si(100) substrate. Organic materials can also be measured with BEEM, in which case, rather than current response being interpreted in terms of the valence band maximum and conduction band minimum of a semiconductor, the transport gap between the highest occupied molecular orbital and the lowest unoccupied molecular orbital of an organic layer may be observed if the organic layer is thick enough. BEEM on multiple layer magnetic heterostructures has also been previously implemented, in a process known as ballistic electron magnetic microscopy (BEMM), which typically takes the form of a specialized technique useful in measuring the magnetic alignment of the domain magnetic moments of two non-local ferromagnetic layers. On a sample composed of two ferromagnetic layers with a metal layer between them, the emitted current is attenuated and partially polarized by the magnetic moment of the surface layer, and then scattered according to its polarization by the magnetic moment of the bottom ferromagnetic layer as it is transported through the sample, thereby allowing high-resolution spatially-resolved imaging of the domain alignment of multiple ferromagnetic materials, as well as the effect of external fields on ferromagnetic domain alignment, which can be applied to measure, for example, spin attenuation length. [42]

Though the complete standardization of the above applications exceeds the reach of this thesis, the standard system developed here can potentially be used for such varieties of further experimentation. Naturally, BEEM also lends itself to measurement of the diverse field of quantum nanostructures, such as quantum

dots (QDs), nanowires, and 2DEG confined wells. Apart from the 2D confined well system, which has begun to be attempted here, the high-precision spatial resolution of BEEM lends itself to transport measurements of the electronic structure of QDs without including contributions from the surrounding environment. Spatially resolved Schottky barrier height measurements have also been performed on metal-semiconductor hybrid nanowires formed by depositing Au on vertically stabilized vapor-liquid-solid (VLS) grown Si nanowires. [43] These prior studies provide a promising outlook for the use of this experimental setup to examine and optimize the delicate fabrication processes necessary to create superconductor-semiconductor hybrid nanowires. The desired material characteristics, such as high spin-orbit coupling, and the novel properties of such nanowires are discussed in detail below.

7.3 Theoretical Conditions for the Experimental Realization of Majorana Zero Modes using BEEM-enabled Fabrication of Superconductor-Semiconductor Hybrid Nanowires

To better understand the material system this experimental setup has been developed for the purpose of fabricating, some background on the quantum transport principles which predict the existence of MZMs in superconductor-semiconductor hybrid nanowires is necessary. First of all, the principles of Rashba and Dresselhaus spin-orbit interactions provide a foundation for the development of spintronic devices, and give a relationship between the material parameter of spin orbit coupling and the dispersion relation of a material system.

For the example of an electron orbiting a nucleus, the following Hamiltonian can be constructed:

$$\mathcal{H}_{SO} = \frac{\hbar}{4m_0^2c^2}\boldsymbol{\sigma}(\mathbf{p} \times \mathbf{E}) \quad (50)$$

where \mathbf{E} is the field from the nucleus acting on the electron. In a semiconductor material, this model takes a similar form,

$$E_{SO} = q\mu_B\mathbf{B}_{SO}\boldsymbol{\sigma} = \alpha|\boldsymbol{\sigma} \times \mathbf{k}| \quad (51)$$

where μ_B is the Bohr magneton, α is a material constant, and B_{SO} is the magnetic interaction with the material. This means this magnetic field acting on the particle acts perpendicular to the spin in proportion to its k-vector, causing time-reversible spin precession as it moves, with the distance required for a full flip being a characteristic of the material. In practice, the form of the resulting

Hamiltonian results from both the heterostructure interface characteristics, as well as the bulk unit cell characteristics of the particular sample under consideration.

The structural asymmetry arising from interface states and associated band bending results in an electric potential interaction caused by the degree of curvature of the conduction band minimum, which creates the trapped 2DEG accumulation states confined in the bulk of the material near the interface. This electron trapping force is referred to as the Rashba effect, and has a Hamiltonian of the following form for GaAs slab grown in the (011) direction,

$$\mathcal{H} = \alpha(-p_y\sigma_x + p_x\sigma_y) \quad (52)$$

meaning that the resulting interaction points for instance along the +x direction for a k-vector in the +y direction for a +z spin.

There is a related effect which arises from the asymmetry of the bulk unit cell of the material as well, which in the case of GaAs and InAs is zinc-blende. In this case the asymmetry limits the perturbative effect of the lattice such that the resulting Hamiltonian can be expressed as

$$\mathcal{H}_D \propto p_x(p_y^2 - p_z^2)\sigma_x + p_y(p_z^2 - p_x^2)\sigma_y + p_z(p_x^2 - p_y^2)\sigma_x \quad (53)$$

Which can be simplified for 2D material of finite extent in the z-direction, taken to be (001), giving the following much simpler form,

$$\mathcal{H}_D^{2D(100)} = \beta[-p_x\sigma_x + p_y\sigma_y] \quad (54)$$

where β is roughly on the same order of magnitude as α . This then has an additive effect on momentum in the y-direction, and a counteractive effect on momentum in the x-direction.

When α is very close to β , these two effect essentially eliminates the interaction along one particular direction. For example, if an electron with +z spin travels in the +y direction, the Dresselhaus effect acts along +y, the Rashba effect acts along the +x direction and the sum of the two is along the (110) direction, and all other directions of motion similarly result in spin orbit interaction along this direction. This can then be used to develop wide varieties of spintronic devices. For example, a circuit with a voltage gated 2DEG channel connecting to ferromagnetic contacts, such that, by manipulating the applied voltage from the external gate, the spin precession of the flowing electrons can be tuned such that the required spin orientation needed to match the direction of spin at each end of the 2DEG channel needed to pass through the ferromagnetic domains can be achieved, and the circuit can be turned on and off in the same manner as a traditional field effect transistor. Understanding this interaction is imperative to fabricating advanced devices such as those which make use of Majorana fermions.

Majorana fermions are characterized by the fact that they are their own antiparticles. This means that in terms of creation and annihilation operators, the characteristic Majorana operators themselves are equal commuting superpositions of fermionic creation and annihilation operators, as in the following general construction,

$$\gamma_1 = \frac{1}{2}(c^\dagger + c) \quad (55)$$

$$\gamma_2 = \frac{i}{2}(c^\dagger - c) \quad (56)$$

These two particles can then be considered basically similar to two delocalized quasiparticles forming a single ordinary fermionic mode between them. Majorana fermions are theorized to provide a basis for the construction of a topological quantum computer, as they obey a form of exchange statistics characterized by different exchange paths between two particles resulting in measurably different final states. For example, if a set of two coupled fermionic modes $(c_1^\dagger, c_2^\dagger)$, constructed from the Majorana operators as indicated above, in an arbitrary superposition, performing an operation which exchanges two neighboring Majorana quasiparticles adds an additional complex phase, even if one is not present in the original state. Such fermionic modes are predicted to be present at zero energy for a 1-dimensional superconductor-semiconductor hybrid nanowire, with the associated fermionic mode corresponding to a delocalized electron composed of one Majorana quasiparticle at each end.

The model predicting this for a 1D p-wave superconducting tight-binding chain was originally modeled by Kitaev in 2001, [44] which can potentially correspond to the circumstances in a 1D nanowire with a high degree of spin-orbit coupling such that spin ceases to be well defined within the 1D conduction channel in the nanowire. In this model, the key effects to take into account are the intersite hopping between p-orbitals, the potential at each site, and the superconducting gap, which can be used to construct the following general Hamiltonian,

$$\mathcal{H} = \sum_n -\mu c_n^\dagger c_n - t(c_n^\dagger a_{n+1} + a_{n+1}^\dagger c_n) + \Delta c_n c_{n+1} + \Delta^* c_{n+1}^\dagger c_n^\dagger \quad (57)$$

where the first term comes from the chemical potential μ the second comes from the hopping integral t , and the final two terms comes from the superconducting gap Δ . Taking into account the phase dependence of the induced superconducting gap, the following alternate definition of the Majorana operators for this system can be constructed,

$$\gamma_{2n-1} = \exp\left(-i\frac{\theta}{2}\right)c_n^\dagger + \exp\left(i\frac{\theta}{2}\right)c_n \quad (58)$$

$$\gamma_{2n} = i(\exp(-i\frac{\theta}{2})c_n^\dagger - \exp(i\frac{\theta}{2})c_n) \quad (59)$$

where the operator γ_{2n} corresponds to the $2n$ th state in an alternating chain of bound Majorana fermions. In other words, Majorana fermion $2n - 1$ and $2n$ form a bound pair corresponding to a single electron for all n . [45]

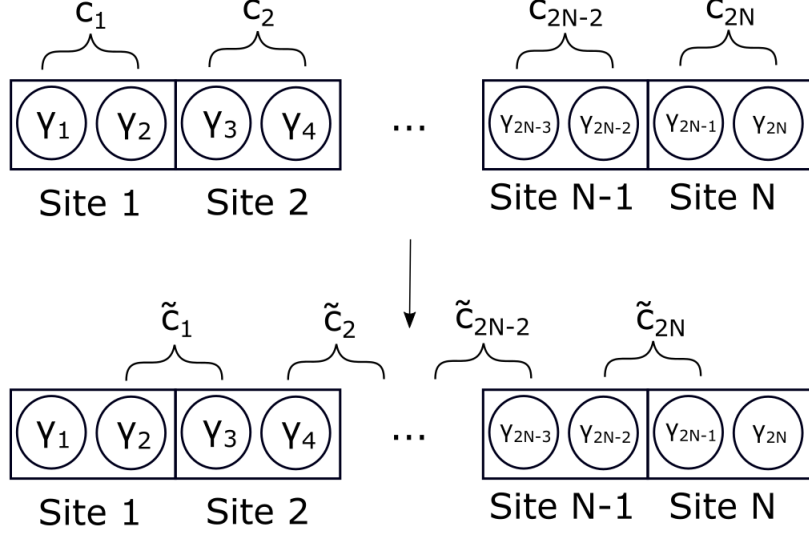


Figure 29: Schematic representation of the Kitaev model for a 1D superconducting p-wave tight-binding chain. At each electron site there are two Majorana fermions, which are related by an associated set of creation and annihilation operators, which represents an equal superposition of two non-Abelian Majorana fermions. In the lower diagram, an alternate set of construction and annihilation operators is constructed, which leaves the two Majorana fermions at the endpoints unpaired, which can be used to construct an additional delocalized fermionic operator, \tilde{a}_M , which can be shown to display non-Abelian exchange statistics. [46]

This is then used to express the above Hamiltonian in a simpler form in terms of Majorana operators on the basis of the assumptions that $|\Delta| = t$ and $\mu = 0$ to

$$\mathcal{H} = it \sum_n^{N-1} \gamma_n \gamma_{n+1} \quad (60)$$

However, by pairing Majorana operators between separate electron sites a new set of creation and annihilation operators can then be constructed,

$$\tilde{c}_n = \frac{1}{2}(\gamma_{2n} + i\gamma_{2n+1}) \quad (61)$$

$$\tilde{c}_n^\dagger = \frac{1}{2}(\gamma_{2n} - i\gamma_{2n+1}) \quad (62)$$

which can be used to write the Hamiltonian as

$$\mathcal{H} = 2t \sum_n^{N-1} (\tilde{c}_n^\dagger \tilde{c}_n - \frac{1}{2}) \quad (63)$$

This summation neglects the operators γ_1 and γ_{2N} , which are then used to construct the delocalized combined fermion operator

$$\tilde{c}_M = \frac{1}{2}(\gamma_1 + \gamma_{2N}) \quad (64)$$

As this state is not a part of the new Hamiltonian, it has no energy despite corresponding to an odd number of total bound operators.

While such a system has never been experimentally observed, there is literature suggesting that a semiconductor-superconductor heterostructure could be used to construct a system which yields this kind of novel delocalized zero-energy state. [47] [48] Though the above model assumes a superconducting 1D nearest-neighbor chain of spinless p-wave orbitals, from a material standpoint, there is reason to believe that for a certain kind of 1D nanowire heterostructure, the confined 2DEG accumulation layer near the surface, which exhibits both the Rashba and Dresselhaus effects, can satisfy the requirement that the electrons be spinless, given proximity to a conventional superconductor in order to create a superconducting proximity effect, and through a carefully applied magnetic field.

In this situation, the parabolic dispersion band in the bulk material is split in momentum according to the spin-orbit interaction previously described, and the proximity to the superconductor effectively forces a superconducting gap between the valence band minimum and the conduction band maximum. When applying the magnetic field along the axis of the wire, however, the polarization of spin inhibits the ability of electrons to form Cooper pairs, and therefore the superconducting gap is gradually closed as the external magnetic field increases. At this point, the poorly-defined spin resulting from the high degree of spin-orbit coupling causes the system to undergo a topological phase transition in which the superconducting gap reopens, creating a "negative gap." Said phase transition can result in the superconducting layer effectively acting as a spin-less p-wave superconductor, given that the magnitudes of the spin orbit and magnetic interactions are precisely tuned.

In this case, the resulting Hamiltonian, in its simplest form becomes

$$\mathcal{H} = [p^2/2m - \mu(y)]\tau_z + u(y)p\sigma_z\tau_z B(y)\sigma_x + \Delta(y)\tau_x \quad (65)$$

where the first term is momentum and chemical energy, the second is spin orbit interaction, the third is magnetic field, and the fourth is the superconductivity, all acting on a single particle. [49]

BEEM measurement can be used in the optimization of such devices, as the material characteristics of the buried interface between the superconductor layer and the underlying nanowire are of utmost importance to create such a precisely constructed system. Any deterioration, defects, or charge traps present at the interface could easily destroy such a system, even if the predictions for a perfectly constructed system hold for a system which is chemically possible to fabricate. As a result, using experimental procedures with the standardized BEEM setup as a fundamental current transport system can provide the key insights necessary for optimizing the UHV-MBE system to create atomically nearly-perfect metal-semiconductor junctions. The experimental transport data recorded through the BEEM setup can be compared against detailed material simulations, which can in turn be used to inform the construction of new nanostructures which may display the properties necessary for the creation of an MZM system. Ballistic transport measurements can then in turn be performed on these new nanostructures, cyclically, until a viable material system is found.

7.4 Conclusion

As a result of standardizing the three-probe BEEM experimental setup through the means described in this thesis, the high-precision *in-situ* MBE fabrication system used to fabricate the above test samples can be implemented to optimize the development of advanced nanostructures, in particular, superconductor-semiconductor hybrid nanowires. By applying BEEM measurement techniques to such nanostructures, the electronic characteristics of the relevant epitaxially-grown interfaces can be analyzed in detail and compared to theoretical predictions.

To accomplish this, a sample consisting of an Au thin film grown epitaxially on a GaAs substrate was first tested using two scanning probes and the sample backside ground as transport contacts. Despite the lack of expected response for this system, it was instrumental in diagnosing the issue of the sample backside ground transport as a point of noise in the system. The initial attempt, which failed to produce the expected result, led to the creation of a three-probe measurement system, consisting of an additional probe, constructed from an Au wire, being used as a contact for recording collector current, through a separately deposited contact from the Au thin film under study. By depositing Ti between the Au and the GaAs substrate for one of many circular deposition regions on a sample, an ohmic contact could be precisely fabricated, allowing controlled measurement of ballistic transport current. Once the data acquisition process was standardized, various Schottky barrier-height measurement techniques were tried, and the results com-

pared and referenced to literature. Using a high-precision model which includes a piecewise fit of the sub-threshold current combined with a quadratic response in the near-threshold range, Schottky barrier heights were extracted for a spatially-resolved 2D map, which could then be compared against the surface topography of the sample. In a final attempt at applying the setup to a more elaborate system, BEEM response was measured for a confined 2DEG system with an active region composed of patterned Au grown through Si shadow mask deposition on a layer of a wide-gap InAlAs alloy grown on an InAs layer, resulting in a confined 2DEG electron accumulation layer in the InAs region. Though it was not possible to find a conclusive barrier-height for the wide-gap semiconducting alloy, the measured response was found to be in accordance with results from self-consistent Schrödinger-Poisson simulation and $\mathbf{k}\cdot\mathbf{p}$ perturbation theory simulations of similar systems.

8 Acknowledgments

This thesis was made possible by the generous support of the Microsoft corporation and the University of Copenhagen. Special thanks goes to the expert assistance provided to me at every level by supervisors Peter Krogstrup and Rajib Batabyal. Steffen Zeltzer provided me with a huge amount of help, particularly when it came to experimental processes and sample fabrication. Xiaojing Zhao also provided help in this regard. When it comes to fabrication, I also want to thank Keita Otani, Henrik Ingerslev, and Mohana Rajpalke, of the Microsoft Quantum Materials Lab. For theoretical simulation and discussions, I would like to thank Kasper Grove-Rasmussen, Fabiano Corsetti, and Georg W. Winkler. Khoa Nguyen Do was a major help when it came to lab coordination, especially during coronavirus. Signe Forsberg, Jeanette Pyrdol, and Morten Hannibal Madsen were a significant help in managing the administrative tasks which allowed this thesis to be completed. Thanks also to my family, and especially to my parents for all their support along the way.

References

- [1] V. Mourik, K. Zuo, S. M. Frolov, S. R. Plissard, E. P. A. M. Bakkers, and L. P. Kouwenhoven. Signatures of majorana fermions in hybrid superconductor-semiconductor nanowire devices. *Science*, 336(6084):1003–1007, 2012.
- [2] Anindya Das, Yuval Ronen, Yonatan Most, Yuval Oreg, Moty Heiblum, and Hadas Shtrikman. Zero-bias peaks and splitting in an al–inas nanowire topological superconductor as a signature of majorana fermions. *Nature Physics*, 8(12):887–895, Dec 2012.
- [3] M. T. Deng, C. L. Yu, G. Y. Huang, M. Larsson, P. Caroff, and H. Q. Xu. Anomalous zero-bias conductance peak in a nb–insb nanowire–nb hybrid device. *Nano Letters*, 12(12):6414–6419, 2012. PMID: 23181691.
- [4] G. Binnig, H. Rohrer, Ch. Gerber, and E. Weibel. Tunneling through a controllable vacuum gap. *Applied Physics Letters*, 40(2):178–180, 1982.
- [5] J.E.A de Jong. *Ballistic electron emission microscopy on al2o3 tunnel junctions*. PhD thesis, 2001.
- [6] Matthew C. Beard, Gordon M. Turner, and Charles A. Schmuttenmaer. Transient photoconductivity in gaas as measured by time-resolved terahertz spectroscopy. *Phys. Rev. B*, 62:15764–15777, Dec 2000.
- [7] H. L. Qin, K. E. J. Goh, M. Bosman, K. L. Pey, and C. Troadec. Subthreshold characteristics of ballistic electron emission spectra. *Journal of Applied Physics*, 111(1):013701, 2012.
- [8] T. G. Gopakumar. Scanning tunneling microscope.
- [9] B. Jayant Baliga. Schottky rectifiers. *Fundamentals of Power Semiconductor Devices*, page 171–206, 2018.
- [10] M. K. Weilmeier, W. H. Rippard, and R. A. Buhrman. Ballistic-electron-emission microscopy of conduction-electron surface states. *Phys. Rev. B*, 61:7161–7164, Mar 2000.
- [11] K. Reuter, F. J. Garcia-Vidal, P. L. de Andres, F. Flores, and K. Heinz. Ballistic electron emission microscopy on $\text{cosi}_2/\text{Si}(111)$ interfaces: Band structure induced atomic-scale resolution and role of localized surface states. *Phys. Rev. Lett.*, 81:4963–4966, Nov 1998.
- [12] K. Takayanagi, Y. Kondo, and H. Ohnishi. Cutting edge 1 suspended gold nanowires : Ballistic transport of electrons. 2001.

- [13] D.D.L. Chung and Edward Beam. Gold on gaas: Its crystallographic orientation and control on the orientation of the au-ga reaction product. *Thin Solid Films*, 128(3):299–319, 1985.
- [14] Daniel Gall. Electron mean free path in elemental metals. *Journal of Applied Physics*, 119(8):085101, 2016.
- [15] L.D. Bell, W.J. Kaiser, M.H. Hecht, and L.C. Davis. 7. ballistic electron emission microscopy. In Joseph A. Stroscio and William J. Kaiser, editors, *Scanning Tunneling Microscopy*, volume 27 of *Methods in Experimental Physics*, pages 307–348. Academic Press, 1993.
- [16] L. D. Bell and W. J. Kaiser. Observation of interface band structure by ballistic-electron-emission microscopy. *Phys. Rev. Lett.*, 61:2368–2371, Nov 1988.
- [17] Sabar D. Hutagalung, Khatijah Yaacob, Samsudi Sakrani, and Ahmad Isa. The development of beam modeling for the characterization of si/ge self-assembled quantum dot heterostructures. volume 2006, pages 306 – 310, 02 2006.
- [18] Z. Liliental-Weber, J. Washburn, N. Newman, W. E. Spicer, and E. R. Weber. Morphology of au/gaas interfaces. *Applied Physics Letters*, 49(22):1514–1516, 1986.
- [19] Thomas Ihn. *5.4 Metal electrodes on semiconductor surfaces*. Oxford University Press, 2015.
- [20] S. Forment, R. L. Van Meirhaeghe, A. DeVrieze, K. Strubbe, and W. P. Gomes. A comparative study of electrochemically formed and vacuum-deposited n-GaAs/Au Schottky barriers using ballistic electron emission microscopy (BEEM). *Semiconductor Science Technology*, 16(12):975–981, December 2001.
- [21] Robert Balsano, Akitomo Matsubayashi, and Vincent P. LaBella. Schottky barrier height measurements of cu/si(001), ag/si(001), and au/si(001) interfaces utilizing ballistic electron emission microscopy and ballistic hole emission microscopy. *AIP Advances*, 3(11):112110, 2013.
- [22] Wouter Leroy, Stefaan Forment, and R. Van Meirhaeghe. The barrier height inhomogeneity in identically prepared au/n-gaas schottky barrier diodes. *Solid-State Electronics*, 49:878–883, 06 2005.

- [23] D. L. Smith, E. Y. Lee, and V. Narayanamurti. Ballistic electron emission microscopy for nonepitaxial metal/semiconductor interfaces. *Physical Review Letters*, 80(11):2433–2436, 1998.
- [24] L Douglas Bell and Venkatesh Narayanamurti. Ballistic-electron-emission microscopy of semiconductor heterostructures. *Current Opinion in Solid State and Materials Science*, 3(1):38–44, 1998.
- [25] L D Bell and W J Kaiser. Ballistic-electron-emission microscopy: A nanometer-scale probe of interfaces and carrier transport. *Annual Review of Materials Science*, 26(1):189–222, 1996.
- [26] Zuzanna Liliental-Weber. Schottky and ohmic au contacts on gaas: Microscopic and electrical investigation. *Journal of Vacuum Science amp; Technology B: Microelectronics and Nanometer Structures*, 4(4):912, 1986.
- [27] Lisa K. Seidel and Thomas W. Crowe. Fabrication and analysis of gaas schottky barrier diodes fabricated on thin membranes for terahertz applications. *International Journal of Infrared and Millimeter Waves*, 10(7):779–787, 1989.
- [28] Adam J. Barcz. Au-gaas reaction kinetics: Its role in fabrication of ohmic contacts. *MRS Proceedings*, 260, 1992.
- [29] F. Ren, C. R. Abernathy, S. J. Pearton, and J. R. Lothian. Use of ti in ohmic metal contacts to p-gaas. *Journal of Vacuum Science & Technology B: Microelectronics and Nanometer Structures Processing, Measurement, and Phenomena*, 13(2):293–296, 1995.
- [30] W. J. Kaiser and L. D. Bell. Direct investigation of subsurface interface electronic structure by ballistic-electron-emission microscopy. *Phys. Rev. Lett.*, 60:1406–1409, Apr 1988.
- [31] M. Prietsch and R. Ludeke. Ballistic-electron-emission microscopy and spectroscopy of gap(110)-metal interfaces. *Phys. Rev. Lett.*, 66:2511–2514, May 1991.
- [32] P.L. de Andres, F.J. Garcia-Vidal, K. Reuter, and F. Flores. Theory of ballistic electron emission microscopy. *Progress in Surface Science*, 66(1):3–51, 2001.
- [33] Seongjin Ahn, Haining Pan, Benjamin Woods, Tudor D. Stanescu, and Sankar Das Sarma. Estimating disorder and its adverse effects in semiconductor majorana nanowires, 2021.

- [34] H. Hebal, Z. Koziol, S.B. Lisesivdin, and R. Steed. General-purpose open-source 1d self-consistent schrödinger-poisson solver: Aestimo 1d. *Computational Materials Science*, 186:110015, 2021.
- [35] Chien Liu. Self-consistent schrödinger-poisson results for a nanowire benchmark, Oct 2018.
- [36] Charles Kittel and Ching-Yao Fong. *Quantum theory of solids*. Wiley, 2010.
- [37] Peter Y. Yu and Manuel Cardona. *Fundamentals of semiconductors. physics and materials properties*. Springer, 2005.
- [38] Abel Molina and John Watrous. Revisiting the simulation of quantum turing machines by quantum circuits. *Proceedings of the Royal Society A: Mathematical, Physical and Engineering Sciences*, 475(2226):20180767, Jun 2019.
- [39] Shenkai Wang, Junmian Zhu, Raymond Blackwell, and Felix R. Fischer. Automated tip conditioning for scanning tunneling spectroscopy. *The Journal of Physical Chemistry A*, 125(6):1384–1390, 2021. PMID: 33560124.
- [40] Subir Parui, P. Klandermans, Sriram Venkatesan, C Scheu, and T. Banerjee. Hot electron attenuation of direct and scattered carriers across an epitaxial schottky interface. *Journal of physics. Condensed matter : an Institute of Physics journal*, 25:445005, 09 2013.
- [41] A. Davies and H. G. Craighead. Ballistic-electron-emission microscopy characteristics of reverse-biased schottky diodes. *Applied Physics Letters*, 64(21):2833–2835, 1994.
- [42] L. Douglas Bell. Ballistic electron emission microscopy and spectroscopy: Recent results and related techniques. *Journal of Vacuum Science & Technology B*, 34(4):040801, 2016.
- [43] Wei Cai, Yulu Che, Jonathan P. Pelz, Eric R. Hemesath, and Lincoln J. Lauhon. Direct measurements of lateral variations of schottky barrier height across “end-on” metal contacts to vertical si nanowires by ballistic electron emission microscopy. *Nano Letters*, 12(2):694–698, 2012. PMID: 22214531.
- [44] A Yu Kitaev. Unpaired majorana fermions in quantum wires. *Physics-Uspekhi*, 44(10S):131–136, Oct 2001.
- [45] P. Haupt, Hirsh Kamakari, E. Thoeng, and Aswin Vishnuradhan. Majorana fermions in condensed matter physics: The 1d nanowire case. 2018.

- [46] Carlo Beenakker. Search for non-abelian majorana braiding statistics in superconductors. *SciPost Physics Lecture Notes*, 2020.
- [47] R. M. Lutchyn, E. P. A. M. Bakkers, L. P. Kouwenhoven, P. Krogstrup, C. M. Marcus, and Y. Oreg. Majorana zero modes in superconductor–semiconductor heterostructures. *Nature Reviews Materials*, 3(5):52–68, May 2018.
- [48] Yuval Oreg, Gil Refael, and Felix von Oppen. Helical liquids and majorana bound states in quantum wires. *Phys. Rev. Lett.*, 105:177002, Oct 2010.
- [49] Liang Fu and C. L. Kane. Superconducting proximity effect and majorana fermions at the surface of a topological insulator. *Phys. Rev. Lett.*, 100:096407, Mar 2008.

Appendices

A Analysis Code

A.1 Height Profiles

```
1
2 close all
3 clear all
4 clc
5
6 data=importdata ('heightchap6.txt');
7 X=data(:,1)*1.0e9;
8 height=data(:,2)*1.0e9;
9
10
11 figure('Name', 'Height Profile Au_GaAs')
12     plot(X,height,'-*');
13     title ('Height Profile Au_GaAs')
14     set(gca,'YDir','Normal')
15     axis tight
16     xlabel('X (nm)','FontSize',14, 'FontWeight','bold');
17     ylabel('Height (nm)','FontSize',14,'FontWeight','bold');
```

A.2 Sub-threshold Fitting

```
1 close all
2 clear
3 clc
4
5
6 load ('BEEM2021-03-23_LineSpectra1_Ic.mat')
7 Ic=mean_array*1e3;
8 Ic=Ic-max(Ic);
9 Ic=-1*Ic;
10 Ic_mean=mean(Ic,2);
11
12 load ('BEEM2021-03-23_LineSpectra1_It.mat')
13 It=mean_array*1e3;
14 It=It-max(It);
15 It=-1*It;
16 It_mean=mean(It,2);
17
18 load ('BEEM2021-03-23_LineSpectra1_dIdV.mat')
19 dIc=mean_array*1e3;
20 dIc=dIc-max(dIc);
21 dIc=-1*dIc;
22 dIc_mean=mean(dIc,2);
23
24 %V - Energy Scale in eV
25 V_tot=1.4;
26 V_min=0.2;
27 V_max=1.6;
28 dV=V_tot/198;
29 V=V_min:dV:V_max;
30 V=sort(V, 'descend');
31
32 %X scale is in nm
33 L=36.07;
34 dX=L/119;
35 X=0:dX:L;
36
37
```

```

38
39     %%%Smoothing along energy axis
40     for i=1:size(Ic,2)
41         Ic_smt(:,i)=smooth(Ic(:,i));
42     end
43
44
45
46
47     %%%Smoothing along energy axis
48     for i=1:size(dIc,2)
49         dIc_smt(:,i)=smooth(dIc(:,i));
50     end
51
52     for i=1:size(Ic_mean,2)
53         Icmean_smt(:,i)=smooth(Ic_mean(:,i));
54     end
55
56
57
58
59
60     lbound=0.1;
61     Vsb=zeros(199-round(lbound/dV), size(Icmean_smt,2));
62     rmax=zeros(199-round(lbound/dV), size(Icmean_smt,2));
63     r = cell(199-round(lbound/dV), size(Icmean_smt,2));
64     fits = cell(199-round(lbound/dV),size(Icmean_smt,2));
65     fitmax = cell(199-round(lbound/dV),size(Icmean_smt,2));
66     for i=1:199-round(lbound/dV)
67         ubound = i + round(lbound/dV);
68         for j=1:size(Icmean_smt,2)
69             r{i,j} = zeros(199-ubound,1);
70             fits{i,j} = cell(199-ubound,2);
71             for k=1:200-ubound
72
73                 fo = fitoptions('Method','NonlinearLeastSquares',...
74                     'Lower',[0 0],...
75                     'Upper',[Inf Inf],...
76                     'StartPoint',[1 0]);

```

```

77     ft = fittype('subthreshold(x,a,b,s)', 'problem', ...
    ↪ 's', 'options', fo);
78     [fits{i,j}{k,1}, fits{i,j}{k,2}, fits{i,j}{k,3}] = ...
    ↪ fit(V((201-k-ubound):(199)).', ...
    ↪ Icmean_smt(201-k-ubound:(199),j),ft, ...
    ↪ 'problem', V_min+dV*(k-1));
79     r{i,j}(k) = fits{i,j}{k,2}.adjrsquare;
80
81
82     end
83     rmax(i,j) = max(r{i,j});
84     fitmax{i,j} = fits{i,j}{r{i,j}==rmax(i,j)};
85     Vsb(i,j)=probvalues(fitmax{i,j});
86 end
87 end
88
89 Vsb2=zeros(size(Icmean_smt,2),1);
90 rmax2=zeros(size(Icmean_smt,2),1);
91 fitmax2=cell(size(Icmean_smt,2),1);
92 for j=1:size(Icmean_smt,2)
93     rmax2(j) = max(rmax(:,j));
94     fitmax2{j} = fitmax{rmax(:,j)==rmax2(j),j};
95     Vsb2(j)=probvalues(fitmax2{j});
96 end
97
98 bounds=(lbound+dV):dV:200*dV;

```

Sub-threshold Function

```

1 function y = subthreshold(x,a,b,s)
2
3 e = 1.60217646 * 10^(-19);
4
5
6 y = zeros(size(x));
7
8 % This example includes a for-loop and if statement
9 % purely for example purposes.
10 for i = 1:length(x)

```

```
11     if x(i) < s
12         y(i) = a * exp(b * (x(i) - s));
13     else
14         y(i) = a * (1 + b * (x(i) - s) + 0.5 * b^2 * (x(i) - ...
           ↪ s)^2);
15     end
16 end
17 end
```

A.3 2D Map Fitting

```
1 close all
2 clear
3 clc
4
5 load ('Map_2D_BEEM.mat')
6 load ('V.mat')
7 load ('X_cord.mat')
8 load ('Y_cord.mat')
9
10 V_min=min(V);
11 V_max=max(V);
12 dV=(V_max-V_min)/length(V);
13
14 X=X(57:61);
15 Y=Y(1:5);
16
17 I = zeros(length(X),length(Y),length(V));
18 I_smt = zeros(length(X),length(Y),length(V));
19 for i=1:length(X)
20     for j=1:length(Y)
21         I(i,j,:)=IC_shape(i,j,:)-max(IC_shape(i,j,:));
22         I(i,j,:)=-1*I(i,j,:);
23         I_smt(i,j,:)=smooth(I(i,j,:));
24     end
25 end
26
27 fo = fitoptions('Method','NonlinearLeastSquares',...
28     'Lower',[0 0],...
29     'Upper',[Inf Inf],...
30     'StartPoint',[1 0]);
31 ft = fittype('subthreshold(x,a,b,s)','problem', ...
32     ↪ 's','options',fo);
33
34 r = zeros(length(X),length(Y),length(V));
35 Vsb = zeros(length(X),length(Y));
36 rmax = zeros(length(X),length(Y));
```

```

37 fits = cell(length(X),length(Y),3);
38 fitmax = cell(length(X),length(Y),3);
39 ubound = round(0.2/dV);
40 for i=1:length(X)
41     for j=1:length(Y)
42
43         for k=1:(length(V)-1-ubound)
44
45             [fits{i,j,k,1}, fits{i,j,k,2}, fits{i,j,k,3}] = ...
46                 ↪ fit(V(length(V)-k-ubound:length(V)-k).', ...
47                 ↪ permute(I_smt(i, j, ...
48                 ↪ length(V)-k-ubound:length(V)-k), [3 1 ...
49                 ↪ 2]),ft, 'problem', V_min+dV*(k-1));
50             r(i,j,k) = fits{i,j,k,2}.adjrsquare;
51
52         end
53         rmax(i,j)=max(r(i,j,1:length(V)-ubound-1));
54         fitmax{i,j} = fits{i,j,r(i,j,:)==rmax(i,j)};
55         Vsb(i,j)=probvalues(fits{i,j,r(i,j,:)==rmax(i,j)});
56     end
57 end
58
59 figure('Name', 'Vsb (Au/GaAs)')
60 imagesc(X,Y,Vsb);
61 title ('Au/GaAs- Vsb as a function X and Y')
62 axis tight
63 xlabel('X (nm)','FontSize',14, 'Fontweight', 'bold');
64 ylabel('Y (nm)','FontSize',14, 'Fontweight', 'bold');
65 set(gca,'YDir','reverse')
66 colorbar
67
68 figure('Name', 'Adjusted R^2 (Au/GaAs)')
69 imagesc(X,Y,rmax);
70 title ('Au/GaAs- Adjusted R^2 as a function X and Y')
71 axis tight
72 xlabel('X (nm)','FontSize',14, 'Fontweight', 'bold');

```

```
73 ylabel('Y (nm)', 'FontSize', 14, 'Fontweight', 'bold');  
74 set(gca, 'YDir', 'reverse')  
75 colorbar  
76 caxis([-1 1])
```

A.4 Logarithm Fitting

```
1 close all
2 clear
3 clc
4
5
6 load ('BEEM2021-03-23_LineSpectra1_Ic.mat')
7 Ic=mean_array*1e3;
8 Ic=Ic-max(Ic);
9 Ic=-1*Ic;
10 Ic_mean=mean(Ic,2);
11
12 load ('BEEM2021-03-23_LineSpectra1_It.mat')
13 It=mean_array*1e3;
14 It=It-max(It);
15 It=-1*It;
16 It_mean=mean(It,2);
17
18 load ('BEEM2021-03-23_LineSpectra1_dIdV.mat')
19 dIc=mean_array*1e3;
20 dIc=dIc-max(dIc);
21 dIc=-1*dIc;
22 dIc_mean=mean(dIc,2);
23
24 %V - Energy Scale in eV
25 V_tot=1.4;
26 V_min=0.2;
27 V_max=1.6;
28 dV=V_tot/198;
29 V=V_min:dV:V_max;
30 V=sort(V, 'descend');
31
32 %X scale is in nm
33 L=36.07;
34 dX=L/119;
35 X=0:dX:L;
36
37
```

```

38     %%%Smoothing along energy axis
39     for i=1:size(Ic,2)
40         Ic_smt(:,i)=smooth(Ic(:,i));
41     end
42
43
44
45     %%%Smoothing along energy axis
46     for i=1:size(dIc,2)
47         dIc_smt(:,i)=smooth(dIc(:,i));
48     end
49
50     for i=1:size(Ic_mean,2)
51         Icmean_smt(:,i)=smooth(Ic_mean(:,i));
52     end
53
54     Icmean_smt=log(abs(Icmean_smt));
55
56     lbound=0.05;
57     lround=round(lbound/dV);
58     Vsb=zeros(199-lround, size(Icmean_smt,2));
59     rmax=zeros(199-lround, size(Icmean_smt,2));
60     r = cell(199-lround, size(Icmean_smt,2));
61     fits = cell(199-round(lbound/dV),size(Icmean_smt,2));
62     fitmax = cell(199-round(lbound/dV),size(Icmean_smt,2));
63     for i=1:199-round(lbound/dV)
64         ubound = i+round(lbound/dV);
65         for j=1:size(Icmean_smt,2)
66             r{i,j} = zeros(199-ubound,1);
67             fits{i,j} = cell(199-ubound,2);
68             for k=1:200-ubound
69                 fo = fitoptions('Method','NonlinearLeastSquares',...
70                     'Lower',0,...
71                     'Upper',Inf,...
72                     'StartPoint',0.1);
73                 ft = fittype('a*log(x-b+1)', 'problem', 'b', ...
74                     ↪ 'options', fo);
75                 [fits{i,j}{k,1}, fits{i,j}{k,2}, fits{i,j}{k,3}] = ...
76                     ↪ fit(V((201-k-ubound):(200-k)).', ...
77                     ↪ Icmean_smt(201-k-ubound:(200-k),j), ft, ...

```

```

↪ 'problem', V_min+dV*(k-1));
75     r{i,j}(k) = fits{i,j}{k,2}.adjrsquare;
76
77     end
78     rmax(i,j)=max(r{i,j});
79     fitmax{i,j} = fits{i,j}{r{i,j}==rmax(i,j)};
80     Vsb(i,j)=probvalues(fits{i,j}{r{i,j}==rmax(i,j)});
81 end
82 end
83
84 Vsb2=zeros(size(Icmean_smt,2),1);
85 rmax2=zeros(size(Icmean_smt,2),1);
86 fitmax2=cell(size(Icmean_smt,2),1);
87 for j=1:size(Icmean_smt,2)
88     rmax2(j) = max(rmax(:,j));
89     fitmax2{j} = fitmax{rmax(:,j)==rmax2(j),j};
90     Vsb2(j)=probvalues(fitmax2{j});
91 end
92
93
94 bounds=lbound:dV:199*dV;
95
96
97     nrows1 = size(V(99:198).',1);
98     nrows2 = size(V(1:86).',1);
99     v1 = [ones(nrows1,1) V(99:198).'];
100    v2 = [ones(nrows2,1) V(1:86).'];
101    l1 = v1\(\sqrt{Icmean_smt(99:198)});
102    f1 = l1(1)+l1(2)*V;
103    Ic_log = ((Icmean_smt));
104    l1 = v1\Ic_log(99:198);
105    f1 = l1(1)+l1(2)*V;
106    l2 = v2\Ic_log(1:86);
107    f2 = l2(1)+l2(2)*V;
108    intercept=min(abs(f1-f2));
109
110    for k=1:size(V.')
111        if abs(f1(k)-f2(k)) == intercept
112            V_intercept = V(k);
113            I_intercept = f1(k);

```

```
114         abs(f1(k)-f2(k))
115     end
116 end
```

A.5 Line-spectra

```
1 close all
2 clear all
3 clc
4
5
6 load ('BEEM2021-03-23_LineSpectra1_Ic.mat')
7 Ic=mean_array*1e3;
8 Ic=Ic-max(Ic);
9 Ic=-1*Ic;
10 Ic_mean=mean(Ic,2);
11
12 load ('BEEM2021-03-23_LineSpectra1_It.mat')
13 It=mean_array*1e9;
14 It_mean=mean(It,2);
15
16 load ('BEEM2021-03-23_LineSpectra1_dIdV.mat')
17 dIc=mean_array;
18 dIc=-1*dIc;
19 dIc_mean=mean(dIc,2);
20
21 %V - Energy Scale in eV
22 V_tot=1.4;
23 V_min=0.2;
24 V_max=1.6;
25 dV=V_tot/198;
26 V=V_min:dV:V_max;
27 V=sort(V,'descend');
28
29 %X scale is in nm
30 L=36.07;
31 dX=L/119;
32 X=0:dX:L;
33
```

```
34     %%%Smoothing along energy axis
35     for i=1:size(It,2)
36         Ic_smt(:,i)=smooth(It(:,i));
37     end
38
39
40
41
42     %%%Smoothing along energy axis
43     for i=1:size(It_mean,2)
44         It_smt(:,i)=smooth(It_mean(:,i));
45     end
46
47
48
49     %%%Smoothing along energy axis
50     for i=1:size(dIc,2)
51         dIc_smt(:,i)=smooth(dIc(:,i));
52     end
53
54     %%%Smoothing along energy axis
55     for i=1:size(dIc_mean,2)
56         dIcmean_smt(:,i)=smooth(dIc_mean(:,i));
57     end
```